



저작자표시-비영리-변경금지 2.0 대한민국

이용자는 아래의 조건을 따르는 경우에 한하여 자유롭게

- 이 저작물을 복제, 배포, 전송, 전시, 공연 및 방송할 수 있습니다.

다음과 같은 조건을 따라야 합니다:



저작자표시. 귀하는 원저작자를 표시하여야 합니다.



비영리. 귀하는 이 저작물을 영리 목적으로 이용할 수 없습니다.



변경금지. 귀하는 이 저작물을 개작, 변형 또는 가공할 수 없습니다.

- 귀하는, 이 저작물의 재이용이나 배포의 경우, 이 저작물에 적용된 이용허락조건을 명확하게 나타내어야 합니다.
- 저작권자로부터 별도의 허가를 받으면 이러한 조건들은 적용되지 않습니다.

저작권법에 따른 이용자의 권리는 위의 내용에 의하여 영향을 받지 않습니다.

이것은 [이용허락규약\(Legal Code\)](#)을 이해하기 쉽게 요약한 것입니다.

[Disclaimer](#)

공학박사 학위논문

**Functional Inorganic Nanoparticles for
Stem Cell Tracking and
Ischemic Stroke Treatment**

줄기세포 추적 및 뇌경색 치료에 활용되는
기능성 무기 나노입자의 개발

2013년 2월

서울대학교 대학원

화학생물공학부

김 태 호

Functional Inorganic Nanoparticles for Stem Cell Tracking and Ischemic Stroke Treatment

지도 교수 현택환

이 논문을 공학박사 학위논문으로 제출함
2012 년 10 월

서울대학교 대학원
화학생물공학부
김태호

김태호의 공학박사 학위논문을 인준함
2012 년 12 월

위원장 _____ (인)

부위원장 _____ (인)

위원 _____ (인)

위원 _____ (인)

위원 _____ (인)

Abstract

Functional Inorganic Nanoparticles for Stem Cell Tracking and Ischemic Stroke Treatment

Taeho Kim

School of Chemical and Biological Engineering

The Graduate School

Seoul National University

During the last decade, various functional nanostructured materials with interesting optical, magnetic, mechanical, and chemical properties have been extensively applied to biomedical areas including imaging, diagnosis, and therapy. In particular, interdisciplinary collaborative research between material science and biomedicine enabled nanomaterials to translate the medical issues and application to clinical trials. Cellular therapies by the administration of therapeutic cells such

as stem cells or immune cells benefit greatly from the inclusion of nanomaterials to achieve high-resolution tracking of the cells. Another application of nanomaterials is as intrinsic chemotherapeutic agents. Long-term cell tracking can be realized by producing highly sensitive nanoparticles or by the control of particle-cell interactions. Engineering physical and chemical properties of nanoparticles - such as size, surface, and composition, enables to obtain optimized therapeutic potentials at target tissues with minimal toxicity.

Firstly, “hollow” manganese oxide core and mesoporous silica coated (HMnO@mSiO₂) nanoparticles were fabricated for highly efficient T₁ magnetic resonance imaging (MRI) contrast agent for labeling and MRI tracking of stem cells. These nanoparticles have been designed to enable optimal access of water molecules to core Mn ions combined with the large surface area-to-volume ratio, exhibiting much higher r₁ relaxivity over other existing MnO nanoparticle-based MRI contrast agents. Adipose-derived mesenchymal stem cells (MSCs) were efficiently labeled using electroporation, and detected on T₁-weighted MR images *in vitro*. Intracranial grafting of HMnO@mSiO₂-labeled MSCs enabled serial MR monitoring of cell transplants over a prolonged period of time.

Secondly, computed tomography (CT) cell tracking methods with gold nanoparticles were developed. CT cell tracking has been known to be very difficult due to its low sensitivity. Herein, 40 nm citrate stabilized gold nanoparticles were readily complexed with poly-L-lysine (PLL), which were then successfully used to label human mesenchymal stem cells (hMSCs). More importantly, gold nanoparticles labeling did not impair cellular viability, proliferation, and differentiation. Labeled hMSCs were visualized *in vitro* and tracked *in vivo* using micro-CT and their detection limit revealed to be $\sim 1 \times 10^4$ cells/ μl *in vivo*. This study represents, to the best of our knowledge, one of the first attempts to develop CT cell tracking, and can be applied in CT image-guided interventions and fluoroscopic procedures commonly used for injection of molecular and cellular therapeutics.

Finally, the protective effects of ceria nanoparticles against ischemic stroke were studied. Reactive oxygen species (ROS) are a major cause of ischemic brain injury, and ceria nanoparticles are known to exhibit potent free radical scavenging activity. Discrete and uniform 3 nm-sized ceria nanoparticles which were colloiddally very stable and tissue permeable were synthesized. These nanoparticles were successfully demonstrated to protect against ischemic stroke in living animals which

has been done for the first time. Targeting infarct site after intravenous injection, optimal dose of ceria nanoparticles (0.5 and 0.7 mg/kg) significantly reduced infarct volume and ischemic cell death *in vivo*. These protective effects of ceria nanoparticles in *in vivo* model were mediated by scavenging of ROS and a decrease in apoptosis.

Keywords: Nanobiotechnology, Stem cell tracking, Chemotherapeutic agents, Magnetic resonance imaging, Manganese oxide nanoparticles, Micro-CT imaging, Gold nanoparticles, Ischemic stroke, Ceria nanoparticles.

Student Number: 2010-30804.

Contents

Chapter 1 Nanomaterials in Translational Medicine: Therapeutic Applications and Developments ..1

1.1	Introduction	1
1.2	Nanomaterials to track stem cell therapies	5
1.2.1	The importance of stem cell tracking	5
1.2.2	Stem cell imaging modalities	9
1.2.3	Various nanoparticles for stem cell tracking.....	13
1.2.4	Cell labeling techniques.....	22
1.2.5	Applications of stem cell tracking	27
1.3	Nanomaterials as chemotherapeutic agents	33
1.3.1	Nanoparticles as anticancer agents	34
1.3.2	Radical scavenging nanomaterials	38
1.3.2.1	Oxidative stress in biological systems.....	38
1.3.2.2	Fullerenes and fullerene derivative	42
1.3.2.3	Ceria nanoparticles as potential antioxidants ..	45
1.3.2.4	Biological effects of ceria nanoparticles <i>in vitro</i> and <i>in vivo</i>	48

1.4	References.....	54
-----	-----------------	----

**Chapter 2 Mesoporous Silica-Coated Hollow Manganese
Oxide Nanoparticles as Positive T1 Contrast
Agents for Labeling and MRI Tracking of
Adipose-Derived Mesenchymal Stem Cells68**

2.1	Introduction.....	68
2.2	Experimental Section.....	72
2.3	Results and Discussion	85
2.4	Conclusion	110
2.5	References.....	111

**Chapter 3 Micro-CT Imaging of Human Mesenchymal
Stem Cells Labeled with Gold Nanoparticles119**

3.1	Introduction.....	119
3.2	Experimental Section.....	122
3.3	Results and Discussion	134
3.4	Conclusion	155
3.5	References.....	156

Chapter 4 Ceria Nanoparticles that can Protect against Ischemic Stroke	161
4.1 Introduction	161
4.2 Experimental Section	163
4.3 Results and Discussion	180
4.4 Conclusion	211
4.5 References	212
 Bibliography	217
 국문 초록 (Abstract in Korean)	225

List of Tables

Table 1.1	Critical issues for the therapeutic application of stem cells. (from Ref. [8], Solanki, A.; Kim, J. D.; Lee, K.-B. Nanomedicine 2008 , <i>3</i> , 567.).....	7
Table 2.1	Relaxivity date of manganese oxide based nanoparticles (per Mn)	98
Table 3.1	Hydrodynamic diameters of Au nanoparticles and Au NPs-PLL complexes	137
Table 3.2	Surface charge of Au nanoparticles and Au NPs-PLL complexes. Electrophoretic (zeta) potential (ζ) was measured with a particle size and zeta potential analyzer.	138
Table 3.3	HU measurements performed at the following locations in Figure 3.8. 1) Cell transplant: 5×10^5 cells; 2) Cell transplant: 2×10^5 cells; 3) Cell transplant: 6×10^4 cells; 4) Cell transplant: 2×10^4 cells; 5) Brain parenchyma; 6) Skull	154

List of Figures

- Figure 1.1** Nanomaterials in translational medicine. a) Nanomaterials for therapy: tracking cells. b) Nanomaterials as drug delivery systems. c) Nanomaterials as chemotherapeutic agents. d) Nanoparticles that were designed to bind to the specific cells of interest show greater accumulation at the target site. e) Biodistribution of the nanoparticles over time. (modified from Ref. [4], Lavik, E.; von Recum, H. *ACS Nano* **2011**, 5, 3419.).....3
- Figure 1.2** Direct labeling methods for cell tracking. (from Ref. [11], Kircher, M. F.; Gambhir, S. S.; Grimm, J. *Nat. Rev. Clin. Oncol.* **2011**, 8, 677.).....8
- Figure 1.3** A summary of modalities used for molecular imaging. Each modality has particular advantages and disadvantages. (from Ref. [13b], Willmann, J. K.; van Bruggen, N.; Dinkelborg L. M.; Gambhir, S. S. *Nat. Rev. Drug Discover.* **2008**, 7, 591.).....12

Figure1.4 a) Schematic descriptions of the human serum albumin coated iron oxide nanoparticle formation and cell labeling. b) T₂-weighted longitudinal MRI studies on day 7 and c) Prussian blue staining on a rat focal cerebral ischemia model injected with iron oxide labeled macrophages. (from Ref. [25], Xie, J.; Wang, J.; Niu, G.; Huang, J.; Chen, K.; Li, X.; Chen, X. *Chem. Commun.* **2010**, 46, 433.).....18

Figure1.5 *In vivo* MRI of labeled rat glioma cells 24 h after transplantation in the striata of rat brain. a–c) Spin echo images. d–f) R₁ maps. g–i) R₂ maps. j–l) R₁/R₂ merged maps. Two rats are injected with MnO- and SPIO-labeled cells (a,b), and one rat with SPIO labeled cells and unlabeled cells (c; control). (from Ref. [31], Gilad, A. A.; Walczak, P.; McMahon, M. T.; Na, H. B.; Lee, J. H.; An, K.; Hyeon, T.; van Zijl, P. C. M.; Bulte, J. W. M. *Magn. Reson. Med.* **2008**, 60, 1.).....19

Figure 1.6 Human mesenchymal stem cells (hMSCs) were labeled with bioconjugated quantum dots (QDs) a) Brightfield

microscopy images. b) Fluorescence microscope images of QDs-labeled hMSCs. (from Ref. [35], Shah, B. S.; Moiola E. K.; Strosio M. A.; Mao J. J. *Nano Lett.* **2007**, 7, 3071.).
20

Figure 1.7 a) TEM image of SPIO@SiO₂(FITC) nanoparticles. b) Colocalization of green fluorescent SPIO@SiO₂(FITC) with late endosomes/lysosomes. c) T₂-weighted MRI of SPIO@-SiO₂(FITC)-labeled hMSCs. (from Ref. [41], Lu, C.-W.; Hung, Y.; Hsiao, J.-K.; Yao, M.; Chung, T.-H.; Lin, Y.-S.; Wu, S.-H.; Hsu, S.-C.; Liu, H.-M.; Mou, C.-Y.; Yang, C.-S.; Huang, D.-M.; Chen, Y.-C. *Nano Lett.* **2007**, 7, 149.)21

Figure 1.8 a) Prussian blue staining of mesenchymal stem cells (MSCs) labeled with Feridex at 25 µg Fe/mL in culture medium for 2 h a) Feridex only. b) Feridex-PLL (1200 ng/mL PLL). c) Feridex-Superfect (2400 ng/mL Superfect). d) Feridex-PLUS/lipofectamine (1:1250/1:2500). (from Ref. [45b], Frank, J. A.; Miller, B. R.; Arbab, A. S.; Zywicke, H. A.; Jordan, E. K.; Lewis, B.

K.; Bryant, Jr, L. H.; Bulte, J. W. *Radiology* **2003**, 228, 480.).....24

Figure 1.9 Labeling of cells with superparamagnetic iron oxide (SPIO) using magnetoelectroporation. C17.2 mouse neural stem cells a) – d) and rat mesenchymal stem cells (rMSC) e) – g) were incubated with Feridex (2 mg Fe/ml) with a), c), e), g) and without b), d), f) electroporation (EP). (from Ref. [46a], Walczak, P.; Kedziorek, D. A.; Gilad, A. A.; Lin, S.; Bulte, J. W. M. *Magn. Reson. Med.* **2005**, 54, 769.).....25

Figure 1.10 a) Schematic description of triple-label CLIO-Tat. b) Axial MR images of bone marrow samples obtained from mouse femurs. CLIO-Tat labeled CD34+ cells were injected intravenously into NOD/SCID mouse (4.0×10^6 cells/animal). c) Fluorescence microscopy (magnification $\times 160$; insert $\times 1,000$). (from Ref. [48b], Lewin, M.; Carlesso, N.; Tung, C.-H.; Tang, X.-W.; Cory, D.; Scadden, D. T.; Weissleder, R. *Nat. Biotechnol.* **2000**, 18, 410.).....26

Figure 1.11 Serial *in vivo* tracking of MSCs by MRI in animal model of myocardial infarction. a) Injection of 2×10^6 SPIO-labeled MSCs 7 days after left coronary artery ligation created a wide intramural area of hypointensity (arrows) at the anterior LV wall. b) Positive signals are still visible after 28 days. c) Injection of unlabeled MSCs did not alter the magnetic signal of the myocardium. (from Ref. [50a], Amsalem, Y; Mardor, Y; Feinberg, M. S.; Landa, N.; Miller, L.; Daniels, D.; Ocherashvilli, A.; Holbova, R.; Yosef, O.; Barbash, I. M. Leor, J. *Circulation* **2007**, *116*, 38.).29

Figure 1.12 Coronal section through a rat brain at various times after transplantation of embryonic stem cells (ES cells) into the hemisphere contralateral to the induced transient 60-min focal ischemia. (from Ref. [51b], Hoehn, M; Kustermann, E.; Blunk, J. Wiedermann, D.; Trapp, T.; Wecker, S.; Focking, M; Arnold, H.; Hescheler, J.; Fleischmann, B. K.; Schwindt, W.; Buhrle, C. *Proc. Natl. Acad. Sci. U.S.A.* **2002**, *99*, 16267.).30

- Figure 1.13** Clinical cell tracking with MRI. Monitoring of the delivery of dendritic cells labeled with SPIO and ^{111}In by MRI before and after injection into a patient's lymph node. (from Ref. [54], de Vries, I. J.; Lesterhuis, W. J.; Barentsz, J. O.; Verdijk, P.; Krieken, J. H.; Boerman, O. C.; Oyen, W. J. G.; Bonenkamp, J. J.; Boezeman, J. B.; Adema, G. J.; Bulte, J. W. M.; Scheenen, T. W. J.; Punt, C. J. A.; Heerschap, A.; Figdor, C. G. *Nat. Biotechnol.* **2005**, *23*, 1407.).31
- Figure 1.14** Effects of gold nanoparticles on angiogenesis *in vivo* in the ears of nude mice. (from Ref. [61], Mukherjee, P.; Bhattachary, R.; Wang, P.; Wang, L.; Basu, S.; Nagy, J. A.; Atala, A.; Mukhopadhyay, D.; Soker, S. *Clinic. Cancer Res.* 2005, *11*, 3530.).37
- Figure 1.15** Oxidative stress and human pathology. (from Ref. [67], Celardo, I.; Pedersen, J. Z.; Traversa, E.; Ghibelli, L. *Nanoscale*, **2011**, *3*, 1411.).40
- Figure 1.16** Pathways of ROS formation, the lipid peroxidation

process and the role of glutathione (GSH)/catalase and other antioxidants (Vitamin E, Vitamin C, lipoic acid) in the management of oxidative stress. (from Ref. [69b], Valko, M.; Leibfritz, D.; Moncol, J.; Cronin, M. T. D.; Mazur, M.; Telser J.; *Int. J. Biochem. Cell Biol.* **2007**, *39*, 44.).....41

Figure 1.17 Tumor growth inhibition by $[Gd@C_{82}(OH)_{22}]_n$ nanoparticles compared with saline group. (from Ref. [72], Yin, J.-J.; Lao, Meng, J.; Fu, P. P.; Zhao, Y.; Xing, G.; Gao, X.; Sun, B.; Wang, P.C.; Chen, C.; Liang, X.-J. *Mol. Pharmacol.* **2008**, *74*, 1132.).....44

Figure 1.18 A model reaction mechanism for the complete dismutation of hydrogen peroxide. (from Ref. [80b] Celardo, I.; Pedersen, J. Z.; Traversa E.; Ghibelli L. *Nanoscale* **2011**, *3*, 1411.).....47

Figure 1.19 Live–dead assay and Neuron–glial cell assay studies of ceria nanoparticles-treated cultures of adult rat spinal cord. (from Ref. [83], Das, M.; Patil, S.; Bhargava, N.; Kang,

	J.-F.; Riedel, L. M.; Seal, S.; Hickm, J. J. <i>Biomaterials</i> 2007 , 28, 1918.).....	50
Figure 1.20	Effects of ceria nanoparticles on myocardial inflammation. (from Ref. [84], Niu, J.; Azfer, A.; Rogers, L. M.; Wang, X.; Kolattukudy, P. E. <i>Cardiovas. Res.</i> 2007 , 73, 549.)...51	
Figure 1.21	Intravitreal injection of ceria nanoparticles protects rat retina photoreceptor cells from light-induced degeneration. (from Ref. [87], Chen, J.; Patil, S.; Seal S.; Mcginnis, J. F.; <i>Nat. Nanotechnol.</i> 2006 , 1, 142.).....	53
Scheme 2.1	Schematic illustration of the synthesis of HMnO@mSiO ₂ nanoparticles and labeling of MSCs	91
Figure 2.1	Characterization of HMnO@mSiO ₂ nanoparticles. (a) TEM image. (b) HRTEM image of a single nanoparticle. (c) T ₁ map of HMnO@mSiO ₂ nanoparticles suspended in water at 11.7 T. (d) Plot of 1/T ₁ versus Mn concentration.	92
Figure 2.2	N ₂ adsorption/desorption isotherms of HMnO@mSiO ₂ (inset: pore size distribution; V: pore volume, D: pore	

	size).....	93
Figure 2.3	TEM images of (a) PEG-phospholipid-capped MnO nanoparticles (MnO@PEG-phospholipid) and (b) dense silica-coated MnO nanoparticles (MnO@dSiO ₂).	94
Figure 2.4	XRD pattern for HMnO@mSiO ₂ nanoparticles before (a) and after (b) acid etching..	95
Figure 2.5	Hydrodynamic size distribution of HMnO@mSiO ₂ nanoparticles in PBS, as measured by dynamic light scattering (DLS).....	96
Figure 2.6	Electrophoretic (zeta) potential (ζ) was measured with particle size and a zeta potential analyzer.	97
Figure 2.7	(a) T ₁ -weighted MR image of adipose derived MSC suspended in 5% gelatin. (b) Normalized MRI signal intensity of cells electroporated with nanoparticles, incubated with nanoparticles, or electroporated without nanoparticles. (c) The R ₁ relaxation rate plotted as a	

	function of the nanoparticle concentration used for labeling the cells	103
Figure 2.8	Microscopy images of RITC-HMnO@mSiO ₂ -labeled MSCs, counterstained with Hoechst 33342. Using (a) electroporation or (b) simple incubation with 0, 11.4, and 34.3 µg Mn/ml (left to right).....	104
Figure 2.9	Assessment of MSC viability at 24 h after electroporation or simple incubation with HMnO@mSiO ₂ nanoparticles.	106
Figure 2.10	Differentiation of HMnO@mSiO ₂ -labeled MSCs into adipogenic (a-d) or osteogenic (e-h) phenotype.	107
Figure 2.11	<i>In vivo</i> MRI of transplanted MSCs (a) No hyperintense signal was detected in mice transplanted with unlabeled MSCs. (b) Hyperintense signals (green arrows) were detected in mice transplanted with HMnO@mSiO ₂ -labeled MSCs and was visible 14 days after injection...	109
Figure 3.1	a) Schematic illustration of Au NPs-PLL(RITC) complexes. b) TEM images of 40 nm Au NPs-PLL(RITC)	

	complexes.....	136
Figure 3.2	Cellular uptake of Au NPs-PLL(RITC) complexes to human mesenchymal stem cells. a) Brightfield microscopy images. b) Fluorescence microscopy images. c) Transmission electron microscopy images.	140
Figure 3.3	Assessment of cell viability and proliferation using a) MTS assay, and b) Calcein-AM assay..	143
Figure 3.4	Differentiation of labeled (a-c) and unlabeled hMSCs (d-f) and in 3 weeks b, e) Adipogenic differentiation c, f) Osteogenic differentiation.....	144
Figure 3.5	<i>In vitro</i> micro-CT imaging of hMSCs labeled with different concentrations of Au NPs-PLL(RITC) complexes. a) Micro-CT images and HU values of hMSCs suspended in 1% agarose (1×10^6 cells/tube). b) HU vs. versus Au concentration used for labeling. c) HU values vs. intracellular Au concentration as measured by ICP-MS	148

Figure 3.6	HU of labeled cell phantoms (○) versus HU of free gold nanoparticles phantoms (●).....	149
Figure 3.7	<i>In vitro</i> micro-CT imaging of different number of labeled hMSCs. a) Micro-CT images and HU of labeled hMSCs suspended in 1% agarose. b) A Plot of HU values vs. Number of cells labeled with Au NPs-PLL(RITC) complexes (0.1 mg Au/ml).....	150
Figure 3.8	<i>In vivo</i> micro-CT images of transplanted hMSCs by stereotaxic injection. a) Different number of cells labeled with Au NPs-PLL(RITC) complexes (0.1 mg Au/mL) were transplanted into parenchyma of rat brain. 1) 5×10^5 cells; 2) 2×10^5 cells; 3) 6×10^4 cells; 4) 2×10^4 cells. b) Immunofluorescence images of the corresponding brain tissue section in a). Left) Transplanted hMSCs are stained with anti-human cytoplasmic (STEM121) antibody (green). Middle) Au NPs-PLL(RITC) complexes (red). Right) Overlapped image of the left and the middle image. Scale bar = 200 μm	153

Figure 4.1	a) TEM images of 3-nm-sized ceria nanoparticles. b) High-resolution TEM images. c) The selected area electron diffraction pattern.....	183
Figure 4.2	X-ray diffraction pattern revealed a cubic fluorite structure.....	184
Figure 4.3	X-ray photoelectron spectroscopy analysis was used to identify the valence state of cerium ions.....	185
Figure 4.4	a) Hydrodynamic diameters of phospholipid-PEG-capped ceria nanoparticles in PBS and blood. b) A sketch of the ceria nanoparticles geometry (core diameter $d_c = 3 - 4$ nm and hydrodynamic diameter $d_h = 17 - 18$ nm)	186
Figure 4.5	ROS-scavenging activities of ceria nanoparticles by superoxide dismutase-mimetic assay and catalase-mimetic assay.	187
Figure 4.6	Autocatalytic activity of ceria nanoparticles as examined by color change and UV/Vis spectroscopy. (a) Reversible	

	color change. (b) UV/Vis absorption spectra show the red-shift of the band between 300 and 400 nm	188
Figure 4.7	Protective effects of ceria nanoparticles against ROS-induced cell death <i>in vitro</i>	191
Figure 4.8	Fluorescence microscopy images of CHO-K1 cells incubated with ceria nanoparticles conjugated with a fluorescent rhodamine dye	192
Figure 4.9	Cellular uptake of ceria nanoparticles according to concentration and time analysed by fluorescence-activated cell sorting (FACS)	193
Figure 4.10	Infarct volume and ischemic cell death decrease <i>in vivo</i>	197
Figure 4.11	Ischemic cell death decrease <i>in vivo</i> . a) Microscopic analysis of cell death in brain slices using TUNEL b) Quantitative analysis of the number of TUNEL-positive cells.	199
Figure 4.12	The concentration of ceria nanoparticles in the	

	nonischemic brain at 24 h after ischemia was very low, but significantly increased at 24 h after ischemia.....	202
Figure 4.13	Identification of rhodamine B isothiocyanate-conjugated ceria nanoparticles in the ischemic hemisphere.....	203
Figure 4.14	Computerized visual augmentation with 3-dimensional reconstruction of fluorescence signals	204
Figure 4.15	Reactive oxygen species (ROS)-scavenging effects <i>in vivo</i> . a, b)Oxidized hydroethidine signals (as a detector of ROS) were decreased in the ceria nanoparticle-injected group	207
Figure 4.16	Decrease of Lipid peroxides in stroke area of ceria- injected group.....	208
Figure 4.17	Apoptosis-reducing effects. a) Morphological criteria of apoptotic TUNEL-positive cells. b) Quantitative analysis of apoptotic cells in the ceria-nanoparticle-injected group	209

Figure 4.18 Western blotting analyses – decrease of pro-apoptotic proteins, such as phospho-p53, cleaved caspase-3, and gelsolin, in the ceria nanoparticle-injected group210

Chapter 1. Nanomaterials in Translational Medicine: Therapeutic Applications and Developments

1.1 Introduction

Biomedical engineering is an evolving field of research having enormous potential with positive impact on human health care system. The recent nanotechnology is expected to solve lots of key questions of biological systems. Functional elements of biological systems are mostly in the nanometer scale range and so nanomaterials can interact with them at the molecular levels.^[1] Furthermore, nanomaterials ranging from 2 to 100 nm exhibit unique electronic, optical, physical, and magnetic properties which are different from their bulk counterparts.^[2] Therefore biological phenomena can be explored by precisely controlling and harnessing these unique properties of nanomaterials.^[3]

In particular, collaborative research between material science and biomedicine enabled the use of nanomaterials to translate medical

issues and applications to clinical trials. As shown in Figure 1.1, one of the areas in which nanomaterials can move to the clinic is in tracking treatments. For example, cellular therapies by the administration of therapeutic cells such as stem cells or immune cells benefit greatly from the inclusion of nanomaterials which permit high-resolution tracking of the cells. Nanomaterials can act as drug delivery vehicles for the targeted delivery of therapies to increase efficacy and to reduce side effects. Furthermore, recent investigations have proven that some of the nanomaterials can act as intrinsic chemotherapeutic agents at the target sites. ^[4]

Of course, we should first understand how nanomaterials interact with the cells at the molecular level, and their mechanism and toxicity during the processing. The biodistribution and pharmacokinetics influenced by nanomaterial surfaces and their administration routes should also be assessed. To properly evaluate their therapeutic efficacy, appropriate disease model should also be chosen. ^[5]

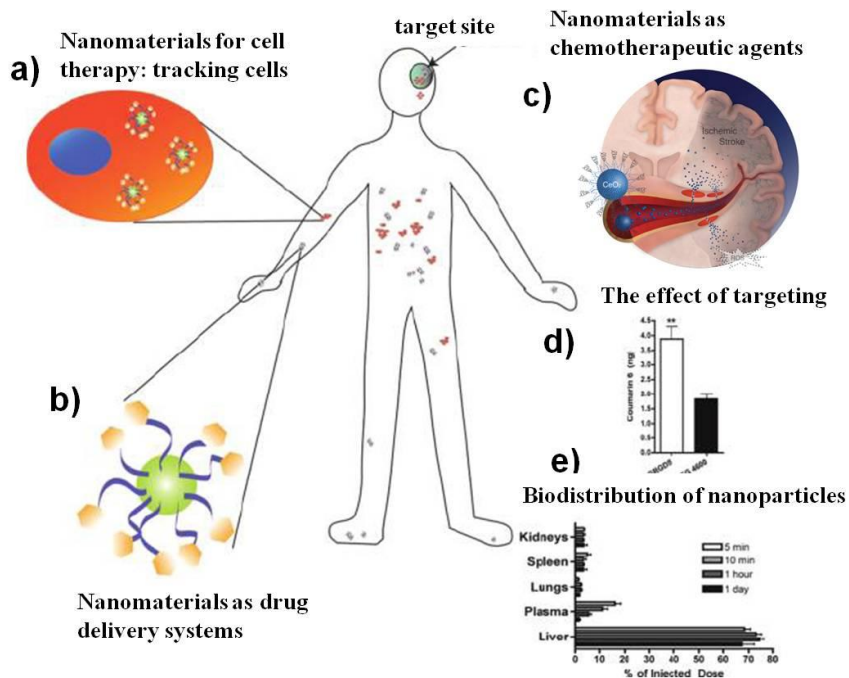


Figure 1.1. Nanomaterials in translational medicine. a) Nanomaterials for cell therapy: tracking cells. Nanomaterials can be designed to be endocytosed by cells. The particles generate a signal by various imaging modalities which permit non-invasive tracking of cell therapies. b) Nanomaterials as drug delivery systems. Nanoparticles can be administered systemically to deliver a drug to a target site such as a tumor through passive or active targeting. c) Nanomaterials as chemotherapeutic agents. Nanoparticles at a target site work as therapeutic agents with their intrinsic chemical properties – eg. treatments of neurodegenerative disease by scavenging reactive oxygen

species. d) Nanoparticles designed to bind to the specific cells of interest show greater accumulation at the target site. e) Biodistribution of the nanoparticles over time. (Modified from Ref. [4], Lavik, E.; von Recum, H. *ACS Nano* **2011**, 5, 3419.)

1.2 Nanomaterials to Track Stem Cell Therapies

Cell based therapeutics has emerged as effective treatment in regenerative medicine. To successfully realize and optimize their therapeutic potentials, cell tracking to understand the migration and proliferation mechanisms of transplanted cells is essential. For this, a number of cell labeling techniques to obtain traceable signals have been developed. In particular, nanoparticles have inherent optical, magnetic, or acoustic properties, and can be detected by corresponding imaging modalities with a high spatial and temporal resolution. These features allow transplanted cells to be differentiated from host cells; and have advantages over traditional post mortem histological methods, as they permit non-invasive, real-time tracking *in vivo*.

1.2.1 The importance of stem cell tracking

Stem cells have drawn a lot of attention for their self-renewal feature and their ability to be differentiated into various specialized cell types.^[6] Such proliferative capacities and pluripotencies enable the cells to replace defective cell populations, which can revolutionize

therapeutics.^[7] However, to fully achieve the therapeutic effects of stem cells, several critical issues should be addressed.^[8] (Table 1.1) The ability to monitor cell survival, migration, and differentiation is essential for the success of cell based therapies. Desired or actual delivery route, and distribution of transplanted cells could also be evaluated through cell imaging.^[9] With these data, it should be easier to optimize the cell delivery to the target pathological sites and maximize the therapeutic effects.^[10]

Direct cell labeling method is widely used because it is relatively simple and does not involve genetic modification of the cell (Figure 1.2).^[11] In direct cell labeling, nanomaterials which are incorporated into cells enables their tracking and it may accelerate the translation of therapies. The control of size and composition of nanoparticles together with their surface engineering could allow efficient particle-cell interaction. In particular, enhancing physical properties and the prolonged cellular retention time of nanomaterials provides a large observation window and therefore makes it possible for longitudinal cell tracking *in vivo*.^[12]

Critical issues for the therapeutic application of stem cells

- The long-term behavior of transplanted stem cells in the target tissues
- The pluripotency/multipotency of stem cells to differentiate towards homogeneous populations of specific cell types
- The control of transplanted stem cells to migrate to the correct microenvironmental places
- The optimal time period for stem cell-replacement therapy for degenerative diseases

Table 1.1. Critical issues for the therapeutic application of stem cells.

(from Ref. [8], Solanki, A.; Kim, J. D.; Lee, K.-B. *Nanomedicine* **2008**, *3*, 567.)

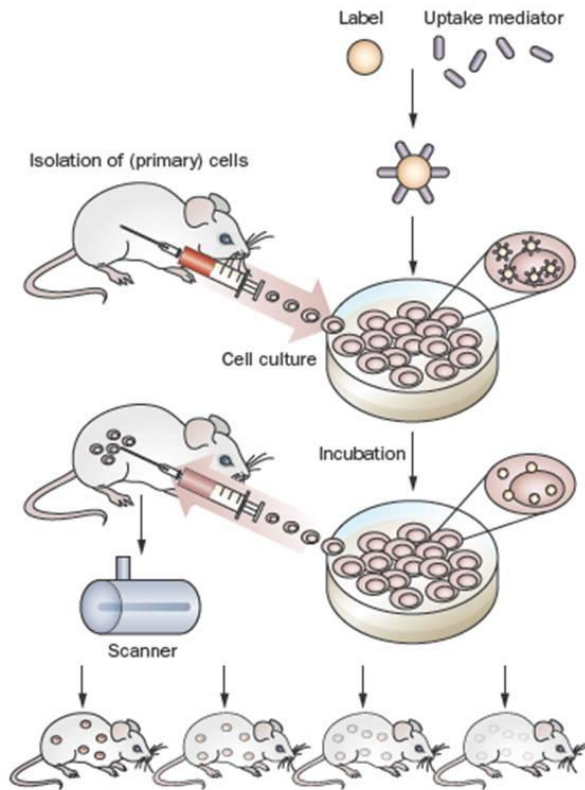


Figure 1.2. Direct labeling methods for cell tracking. For direct labeling of cells, exogenous contrast agents which are coupled with transfection agents or positively charged peptides are incubated with cells. Cells are harvested from a donor first. Once labeled, cells are transplanted into the recipient for repeated scanning. Since the labels are diluted during cell division, imaging is only feasible during a limited period of time. (from Ref. [11], Kircher, M. F.; Gambhir, S. S.; Grimm, J. *Nat. Rev. Clinic. Oncol.* **2011**, 8, 677.)

1.2.2 Stem cell imaging modalities

Imaging plays a critical role in clinical medicine and biomedical research, and various imaging modalities are currently used. However, to determine the suitable imaging modality many factors such as specificity, sensitivity, resolution, availability, and cost-effectiveness should be considered. Consequently, the proper imaging modalities should also be selected for cell imaging by considering these factors to clearly see transplanted cells and evaluate the underlying pathological processes.^[13] There are several molecular imaging modalities as shown in Figure 1.3.

First, magnetic resonance imaging has been widely used as noninvasive imaging modality to produce images of human body with great detail. MRI is particularly attractive for clinical trials because it provides high-resolution, detailed structural images, three-dimensional spatial reconstruction, and no ionizing radiation.^[14] Furthermore, when imaging stem cells by MRI, additional anatomical and pathological information could also be acquired. In this sense, cell tracking by MRI has come forward as an excellent method to provide detailed information of cell location after transplantation and has become the

most commonly used technique.^[15]

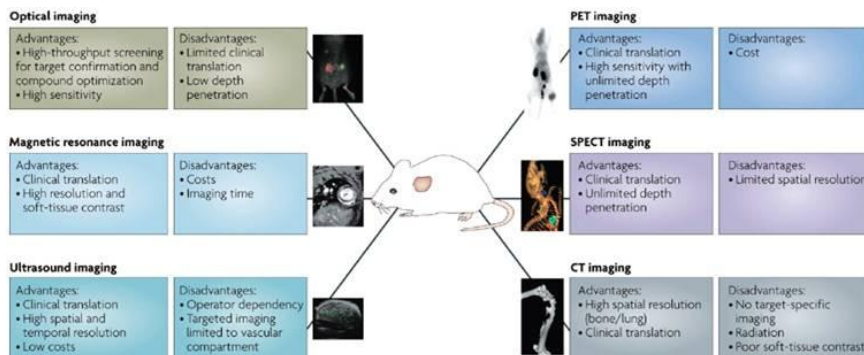
Secondly, X-ray CT has excellent temporal resolution, very high spatial resolution, and satisfactory anatomical depictions. Above all, CT imaging is cost-effective and handy technique with fast imaging processes.^[16] Compared to MRI, cell tracking with CT is much less developed. However, gold nanoparticles have recently successfully proved as blood pool CT contrast agents and demonstrated as molecular imaging probes combined with target molecules.^[17] Gold nanoparticles are recently found to be safely labeled to mesenchymal stem cells and have no detrimental effects on cell viabilities and functions.^[18] Therefore, X-ray CT is now considered as a potential candidate imaging modalities for stem cell imaging, particularly in imaging in brain and lungs.^[19]

Nuclear medicine has an excellent *in vivo* sensitivity and is capable of whole body imaging. However, in order to provide additional anatomical information integrated MRI/PET instrument is now developed. However, radionucleotide-base cell tracking is still unclear due to radiation safety and cellular toxicity issues.^[20]

Optical imaging modalities are very sensitive and particularly managed by low cost and portable optical scanners. In particular, optical imaging,

is not only as sensitive as radiolabel based imaging techniques, but also doesn't need any exposure to irradiation.^[21] Therefore, optical imaging could be an effective means of non-invasive cell tracking repeatedly. However, the wide application of optical imaging is restricted because light scattering and absorption by the tissues occurs and thus optical signals of 4–10 cm from the surface of the skin may not be detected.^[22]

Recently, many optical probes with relatively good tissue penetration in the near-infrared (NIR) range were developed. Now, we can anticipate more wide and realistic applications of optical imaging in molecular targeted imaging and cell tracking *in vivo*.^[23]



Nature Reviews | Drug Discovery

Figure 1.3. A summary of modalities used for molecular imaging. Each modality has particular advantages and disadvantages. (from Ref. [13b], Willmann, J. K.; van Bruggen, N.; Dinkelborg L. M.; Gambhir, S. S. *Nat. Rev. Drug Discover.* **2008**, *7*, 591.)

1.2.3 Various nanoparticles for stem cell tracking

After the introduction of MRI to medical imaging, iron oxide nanoparticles were used as MR imaging contrast agents of the liver to diagnose malignancy.^[24] Iron oxide nanoparticles induce strong field inhomogeneities under magnetic field, and locally reduce the T_2 and T_2^* relaxation. When they are imaged with T_2 and T_2^* -weighted pulse sequences, iron oxide nanoparticles produce hypointense signals on the MRI and these strong signals enable the microscopic visualization of labeled cells (Figure 1.4).^[25] Iron oxide nanoparticles are usually synthesized by thermal decomposition of organometallic precursor or coprecipitation of ferric iron with stabilizing coating materials. In particular, coating materials such as dextran,^[26] polyethylene glycol (PEG),^[27] or polystyrene,^[28] contribute to the stability and solubility of nanoparticles in biological media. They also prevent aggregation of nanoparticles inside cells, which lowers cytotoxicity of the cells as well. Recently, the optimal design of iron oxide nanoparticles to increase the magnetic and MRI contrast-enhancing properties were conducted by controlling the core size or changing the composition of core particles.^[29]

Although iron oxide nanoparticles are widely used MRI contrast agents, iron oxide labeled cells cannot be distinguished from other hypointense regions, such as hemorrhage and blood clots found commonly in many lesions. Therefore, paramagnetic gadolinium (Gd)- or manganese (Mn)-based complexes could be good MRI contrast agents because they produce “positive contrast” to differentiate from the surroundings. They have many unpaired electrons – 7 unpaired electrons for Gd and 5 for Mn, and can generate hyperintense signals in tissues by their predominant effects on the longitudinal (T_1) relaxation time of water protons. Tseng et al. developed a novel MRI contrast agent made of gadolinium hexandion nanoparticles (GDH-NPs) and incorporated into stem cells and monitored the transplanted stem cells.^[30] However, Gd^{3+} ions are known to be very toxic. Moreover, gadolinium-based contrast agents are associated with nephrogenic systemic fibrosis (NSF), particularly when being retained in cells without the fast clearance from the body. Therefore, the broader applications of Gd based cell tracking are now limited. It has been reported that the toxicity of manganese ions to cells is much lower than that of gadolinium based contrast agents which can be comparable to that of iron. Therefore, manganese oxide nanoparticles using positive

contrast draws great attention as an alternative tracking material (Figure 1.5).^[31]

Gold nanoparticles, which are already established as biocompatible dentistry materials, are reported to exhibit low cytotoxicity when labeled to cells.^[32] A few years ago, gold nanoparticles were characterized to have much higher X-ray absorption compared to that of commercialized iodinated compounds, which made gold nanoparticles as good candidate materials for CT contrast agents.^[33] Very recently bismuth, tantalum oxide and ytterbium-based nanoparticles are also developed as promising CT contrast agents.^[34]

Quantum dots have broad absorption and sharp emission bands. They are very photostable and have unique fluorescent properties to be able to tune the emission wavelength by manipulating the size or composition. These characteristics can facilitate the multicolor imaging of cellular events (Figure 1.6).^[35] The production of quantum dots with emission spectrum in near infrared range enabled to demonstrate the stem cell tracking transplanted in the brain.^[36]

Upconverting nanoparticles emitting photons with short wavelength but higher energy which is described as the anti-stokes emission process, were recently produced. They seem to be suitable for *in vivo*

imaging applications because they decrease the problematic photobleaching and autofluorescence problems.^[37] Biological molecules are optically transparent in the near-infrared region. Although upconverting nanoparticles seem to be an ideal candidate for cell labeling and imaging applications, very few studies have been reported with endogeneous cell labeling with them.^[38]

There are some hybrid nanoparticles composed of two or more substances. Ideally, cell labeling and imaging can gather information at both anatomic and functional levels with high spatial and temporal resolution. However, a single modality is not sufficient to provide all these details due to its own limitation of each modality. For instance, MRI has high resolution but low sensitivity. Radionuclide-based imaging techniques have very high sensitivity but have relatively poor spatial resolution. In optical imaging, it is difficult to acquire quantitative fluorescence analysis with living subjects, especially in deep tissues. Combination of several imaging modalities can offer synergistic advantages over any one modality alone.^[39] Additional integration of optical dyes or radionucleotides to MRI probes have synergistic effects to compensate the relatively low sensitivity of MR imaging. Patel et al. developed an ion-sensing nanoparticle formula

composed of a superparamagnetic iron oxide (SPIO) core encapsulated with a porous silica shell. It could be readily anchored with ligands which coordinate with positron-emitting metals. This hybrid nanoparticle has a great potential in cell tracking with both MRI and PET functions.^[40] Bifunctional superparamagnetic SPIO@SiO₂(FITC) core-shell nanoparticles were synthesized for dual modal detection of bone marrow hMSCs (Figure 1.7).^[41] In a recent study, Shi et al. developed Eu³⁺ doped Gd₂O₃ hybrid nanoparticles as a luminescent and T₁-weighted MRI contrast agent for stem cell labeling.^[42] Iron oxide coated with gold shell or iron oxide coated with tantalium oxide was designed for dual MR and CT imaging as well.^[43] In particular, the combination of magnetic nanoparticles and near infrared quantum dots seem to be attractive in *in vivo* stem cell tracking for clinical translation, thus Cy5.5 attached iron oxide were developed and demonstrated for both MR and NIR imaging.^[44]

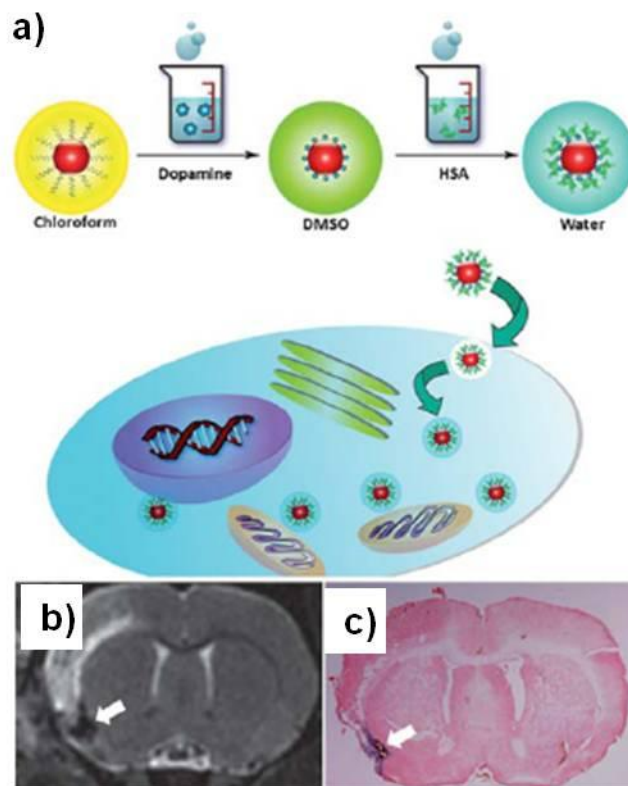


Figure 1.4. a) Schematic descriptions of the human serum albumin coated iron oxide nanoparticle formation and cell labeling. b) T₂-weighted longitudinal MRI studies on day 7 and c) Prussian blue staining on a rat focal cerebral ischemia model injected with iron oxide labeled macrophages. (from Ref. [25], Xie, J.; Wang, J.; Niu, G.; Huang, J.; Chen, K.; Li, X.; Chen, X. *Chem. Commun.* **2010**, 46, 433.)

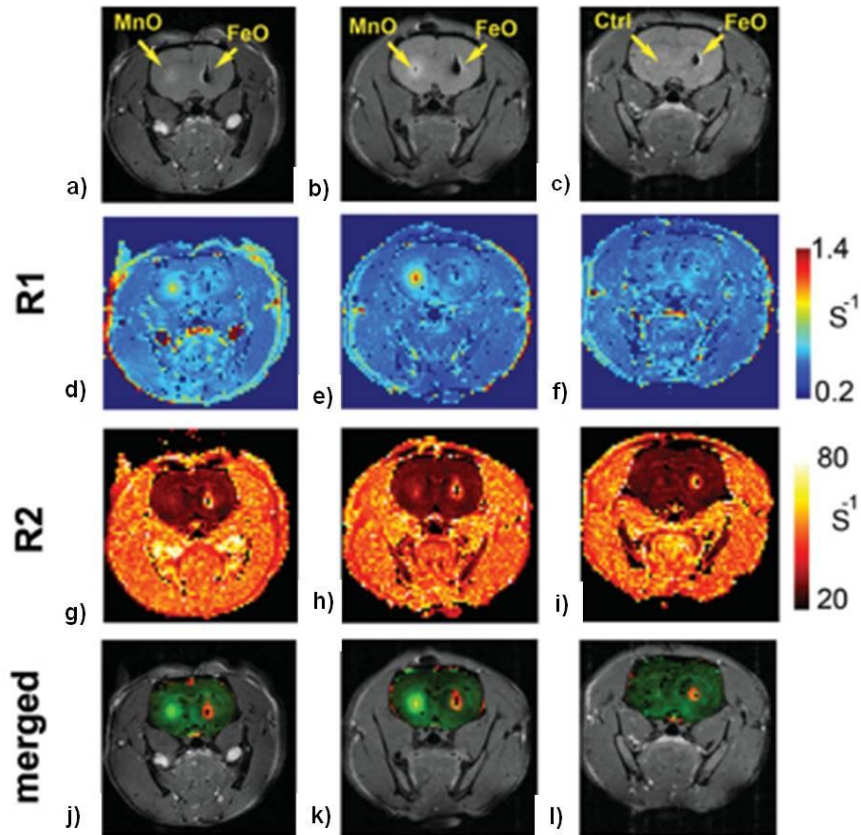


Figure 1.5. *In vivo* MRI of labeled rat glioma cells 24 h after transplantation in the striata of rat brain. a–c) Spin echo images. d–f) R_1 maps. g–i) R_2 maps. j–l) R_1/R_2 merged maps. Two rats are injected with MnO- and SPIO-labeled cells (a,b), and one rat with SPIO labeled cells and unlabeled cells (c; control). (from Ref. [31], Gilad, A. A.; Walczak, P.; McMahon, M. T.; Na, H. B.; Lee, J. H.; An, K.; Hyeon, T.; van Zijl, P. C. M.; Bulte, J. W. M. *Magn. Reson. Med.* **2008**, *60*, 1.)

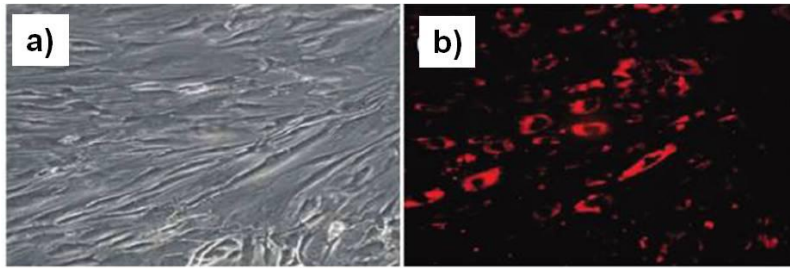


Figure 1.6. Human mesenchymal stem cells (hMSCs) were labeled with bioconjugated quantum dots (QDs). a) Brightfield microscopy images of QDs-labeled hMSCs. b) Fluorescence microscope images of QDs-labeled hMSCs. The QDs are distributed in the perinuclear region within the stem cells. As the MSCs proliferate, the QDs remain bright and are easy to detect. (from Ref. [35], Shah, B. S.; Moioli E. K.; Strosio M. A.; Mao J. J. *Nano Lett.* **2007**, 7, 3071.)

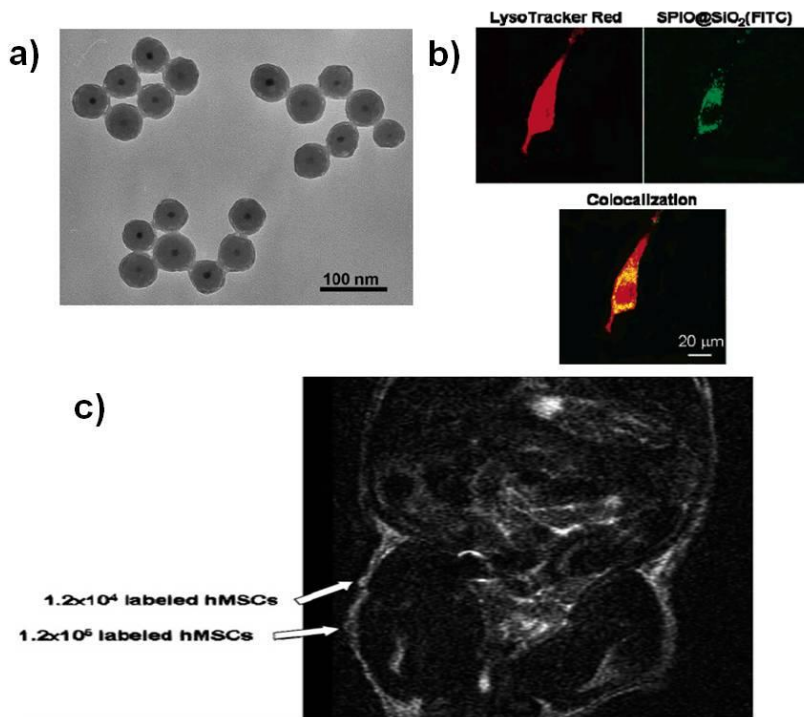


Figure 1.7. a) TEM image of SPIO@SiO₂(FITC) nanoparticles. b) Colocalization of green fluorescent SPIO@SiO₂(FITC) with late endosomes/lysosomes. c) T₂-weighted MRI of SPIO@SiO₂(FITC)-labeled hMSCs was performed. (from Ref. [41], Lu, C.-W.; Hung, Y.; Hsiao, J.-K.; Yao, M.; Chung, T.-H.; Lin, Y.-S.; Wu, S.-H.; Hsu, S.-C.; Liu, H.-M.; Mou, C.-Y.; Yang, C.-S.; Huang, D.-M.; Chen, Y.-C. *Nano Lett.* **2007**, 7, 149.)

1.2.4 Cell labeling techniques

Cell labeling techniques to locate nanoparticles from the extracellular environment to intracellular compartments are necessary. Labeling efficiency is dependent on the properties of cell membranes, size of nanoparticles, and the cell types. Some phagocytotic cells can be successfully labeled by simple incubation. Other cells require additional methods to be effectively labeled with nanoparticles. Polycationic polymers such as poly-L-lysine (MW = 350-400 KDa), protamine sulfate, and lipofectamine were utilized as transfection agents to label cells with nanoparticles.^[45] Nanoparticle-transfection complexes are formed through electrostatic interactions between nanoparticles and transfection agents. When nanoparticle-transfection complexes are mixed with cell culture media, they electrostatically interact with cell membrane which is negatively charged. Afterward, they are uptaken into endosome within cells during the 24 h of labeling periods (Figure 1.8). Alternative labeling methods can be achieved by temporary disruption of cell membrane stability – 1) Electroporation by exerting instant electric pulse,^[46] or 2) Sonoporation by ultrasound pulse (Figure 1.9).^[47] Prolonged incubations are not necessary for these

methods because these methods are instant and accomplished within seconds. However, cell viability can be decreased and parameters should be precisely controlled for successful labeling.

Stem cells can be labeled with nanoparticles by modifying their surfaces with internalizing ligand, such as HIV-Tat peptide which increase the transportation across the cell membrane. Weissleder and coworkers modified aminated dextran coated iron oxide nanoparticles with fluorescein isothiocyanate (FITC) derivatized HIV-Tat peptides, and internalized them into hemotopoietic stem and progenitor cells (Figure 1.10).^[48] Also, internalizing monoclonal antibodies such as OX-26 and anti-CD11 has been conjugated to dextran coated iron oxide nanoparticles and oligodendrocyte progenitor cells were labeled by targeting the transferrin receptors on the cells.^[49] However, these methods require bioconjugation techniques and are economically undesirable. Especially in the case of receptor mediated internalization, only cells expressing the particular receptor targets can be effectively labeled, which limits general use of the nanoparticle conjugates.

Therefore, optimization of transfection and nanoparticles combination should be made for each cell line to achieve highest uptake while not affecting the cell growth and cell function.

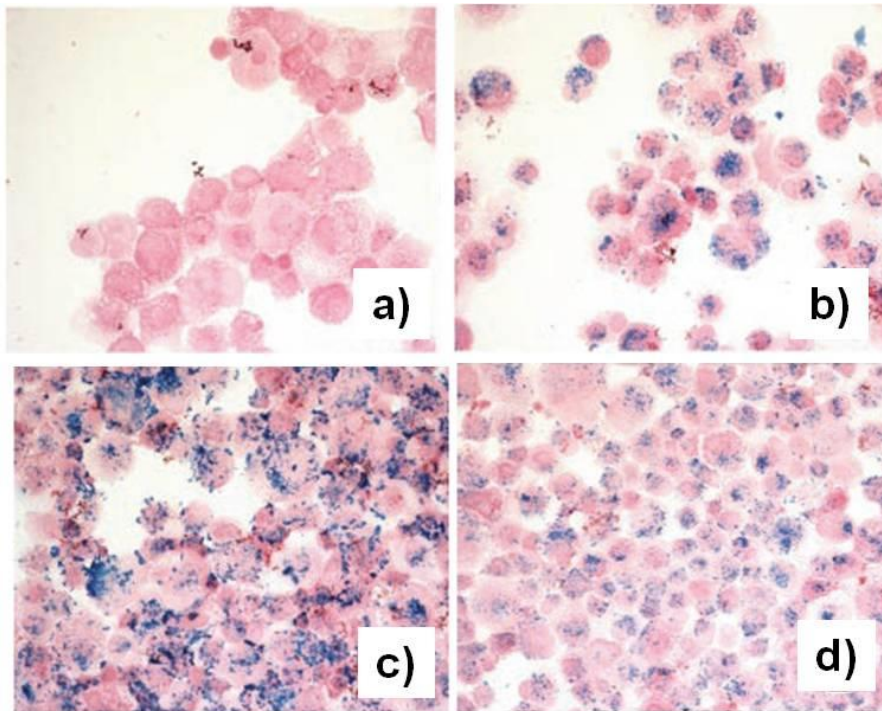


Figure 1.8. a) Prussian blue staining of mesenchymal stem cells (MSCs) labeled with Feridex at 25 μg Fe/mL in culture medium for 2 h a) Feridex only. b) Feridex-PLL (1200 ng/mL PLL). c) Feridex-Superfect (2400 ng/mL Superfect). d) Feridex-PLUS/lipofectamine (1:1250/1:2500 dilution, Invitrogen). (from Ref. [45b], Frank, J. A.; Miller, B. R.; Arbab, A. S.; Zywicke, H. A.; Jordan, E. K.; Lewis, B. K.; Bryant, Jr, L. H.; Bulte, J. W. *Radiology* **2003**, 228, 480.)

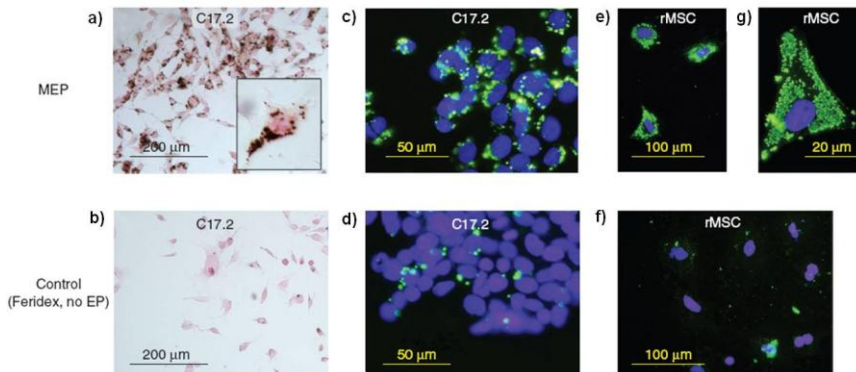


Figure 1.9. Labeling of stem cells with superparamagnetic iron oxide (SPIO) using magnetoelectroporation. C17.2 mouse neural stem cells a) – d) and rat mesenchymal stem cells (rMSC) e) – g) were incubated with Feridex (2 mg Fe/ml) with a), c), e), g) and without b), d), f) electroporation (EP). Only MEP-treated cells show significant Feridex uptake as assessed by DAB-enhanced Prussian blue staining a), and anti-dextran immunofluorescence c), e). (from Ref. [46a], Walczak, P.; Kedziorek, D. A.; Gilad, A. A.; Lin, S.; Bulte, J. W. M. *Magn. Reson. Med.* **2005**, *54*, 769.)

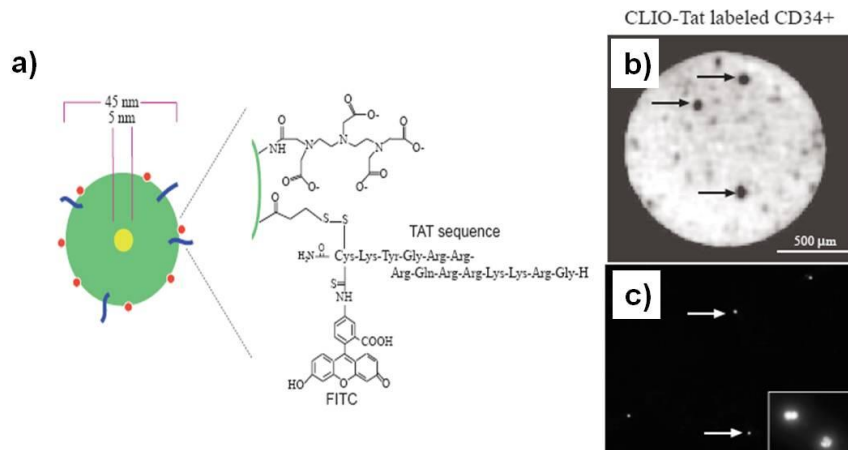


Figure 1.10. a) Schematic description of triple-label CLIO-Tat. Superparamagnetic iron oxide (SPIO) core (yellow) is sterically shielded by cross linked dextran (green), and the FITC-derivatized Tat peptide (blue) was attached to the aminated dextran. The dextran surface was also modified with the chelator DTPA (red) for isotope labeling. b) Axial MR images of bone marrow samples obtained from mouse femurs. CLIO-Tat labeled CD34⁺ cells were injected intravenously into NOD/SCID mouse (4.0×10^6 cells/animal). Single cells are detectable by MR imaging as dark signal voids (arrows). c) Fluorescence microscopy (magnification $\times 160$; insert $\times 1,000$). (from Ref. [48b], Lewin, M.; Carlesso, N.; Tung, C.-H.; Tang, X.-W.; Cory, D.; Scadden, D. T.; Weissleder, R. *Nat. Biotechnol.* **2000**, *18*, 410.)

1.2.5 Applications of stem cell tracking

Stem cell therapy is believed to be highly promising in cardiovascular diseases, such as heart infarct, arterial occlusive disease, and heart valve dysfunction. Stem cell therapies particularly can offer hope for regrowth of the heart tissues and recovery of their functions because heart muscle has the restricted regenerative capacity. Several studies have been performed to track and demonstrate stem cell therapies by MRI in cardiac disease models. For example, distribution of SPIO-labeled MSCs in cardiac tissue was imaged in rodent model and swine model of myocardial infarction (Figure 1.11).^[50]

The central nervous system (CNS) is also very complex and limited in regenerative capacities. Therefore, transplantation of exogenous stem cells can offer great potential to restore the function of brain. In particular, the complexity in central nervous system makes the tracking of transplanted cells more difficult and critical. Imaging of SPIO-labeled hMSCs and tracking their distributions were performed in rodent stroke model (Figure 1.12).^[51] Multiple sclerosis (MS) is another type of disease in which many stem cell based therapies are carried out in animal models.^[52]

Till now, only a few clinical studies have been performed.^[53] As shown in Figure 1.13, autologous dendritic cells were cultured and labeled with SPIO particles and ¹¹¹In-oxine *ex vivo*. Their migration after intranodal injection was imaged in melanoma patients with 3T MRI and with scintigraphy.^[54]

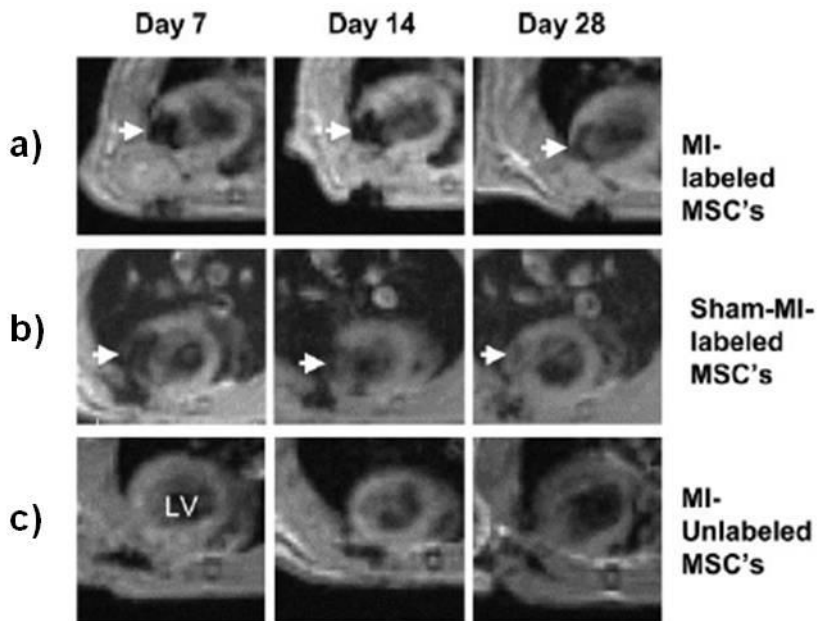


Figure 1.11. Serial *in vivo* tracking of MSCs by MRI in animal model of myocardial infarction. a) Injection of iron oxide labeled MSCs (2×10^6 cells) 7 days after left coronary artery ligation created a wide intramural area of hypointensity (arrows) at the anterior LV wall. b) Positive signals are still visible after 28 days. Similar magnetic signals (arrows) were produced by labeled cells injected to normal hearts. c) Injection of unlabeled MSCs did not alter the magnetic signal of the myocardium. (from Ref. [50a], Amsalem, Y; Mardor, Y; Feinberg, M. S.; Landa, N.; Miller, L.; Daniels, D.; Ocherashvili, A.; Holbova, R.; Yosef, O.; Barbash, I. M. Leor, J. *Circulation* **2007**, *116*, 38.)

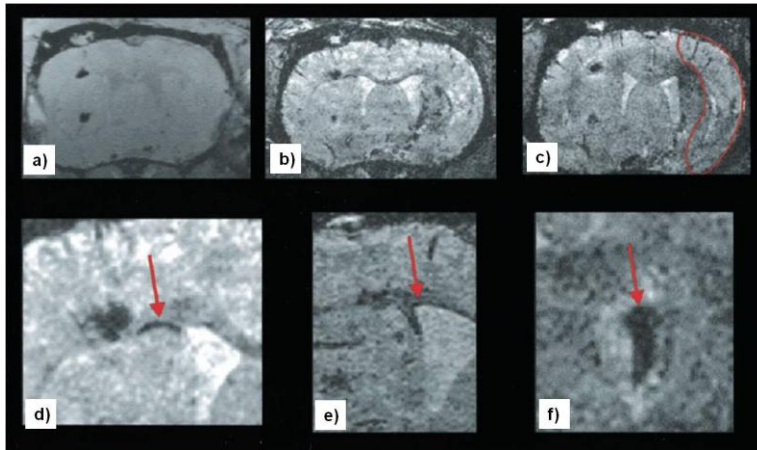


Figure 1.12. Transplantation of USPIO-labeled embryonic stem cells (ES cells) into the contralateral hemisphere of the focal ischemia. 3D data sets were recorded on a) 0th day, b) 6th day, and c) 8th day of transplantation. The necrotic tissue area is outlined in red on c). b) The discrete dark line along the corpus callosum between the cortical implantation site and the ventricular wall show cells migrating toward the lesioned hemisphere. c) the first arrival of labeled cells in the dorsal part of the lesioned territory. d) the migration along the corpus callosum, e) the lining along the ventricular wall, and f) the accumulation of labeled stem cells on the choroid plexus. (from Ref. [51b], Hoehn, M; Kustermann, E.; Blunk, J. Wiedermann, D.; Trapp, T.; Wecker, S.; Focking, M; Arnold, H.; Hescheler, J.; Fleischmann, B. K.; Schwindt, W.; Buhrle, C. *Proc. Natl. Acad. Sci. U.S.A.* **2002**, 99, 16267.)

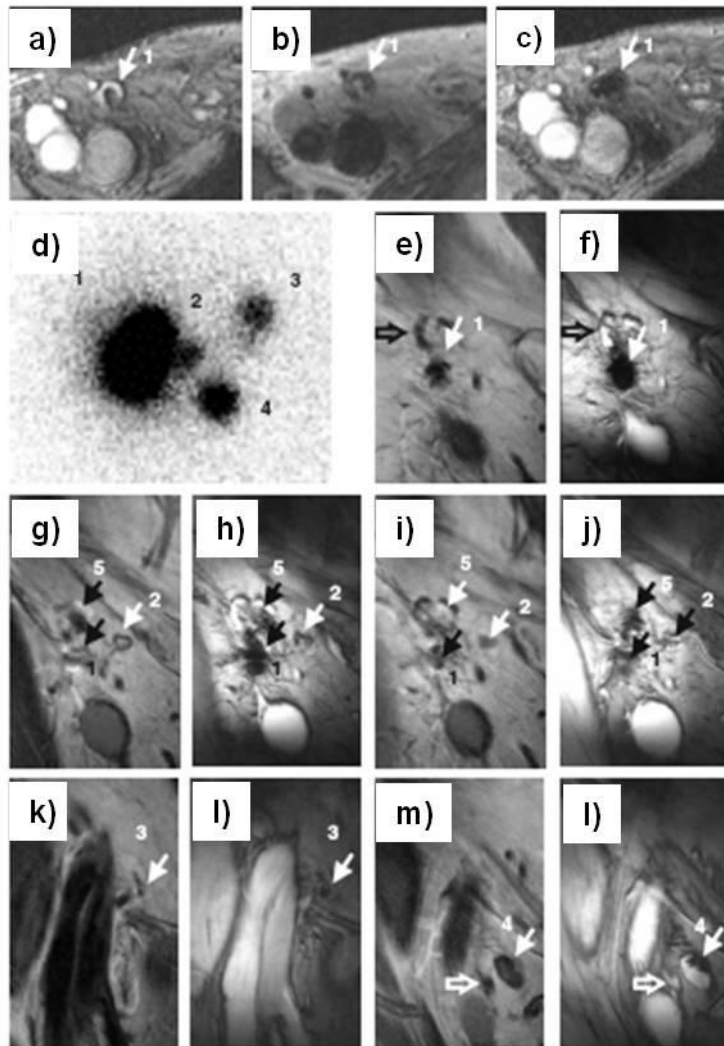


Figure 1.13. Clinical cell tracking with MRI. Monitoring of the delivery of dendritic cells labeled with SPIO and ^{111}In by MRI before and after injection into a patient's lymph node. a) Gradient echo transversal MRI image before vaccination showing a right inguinal

lymph node with a hyperintense signal area (1). b) Spin echo transverse MRI image obtained from the same lymph node after vaccination. c) Gradient echo transverse MRI image after vaccination in same position as part b showing a decreased signal intensity of lymph node (1). *In vivo* migration of labeled dendritic cells 2 days after injection into another patient. d) *In vivo* scintigraphy showing migration of the dendritic cells from the injection lymph node (1) to the following three lymph nodes (2–4). Five coronal gradient echo and spin echo images showing migration of the dendritic cells from e, f) the injection lymph node (1) to g - n) four following lymph nodes (2–5). Open arrows indicate lymph nodes that do not contain SPIO (dark grey on spin echo images; white on gradient echo images). Closed arrows indicate lymph nodes that are positive for SPIO in the gradient echo MRI image. (from Ref. [54], de Vries, I. J.; Lesterhuis, W. J.; Barentsz, J. O.; Verdijk, P.; Krieken, J. H.; Boerman, O. C.; Oyen, W. J. G.; Bonenkamp, J. J.; Boezeman, J. B.; Adema, G. J.; Bulte, J. W. M.; Scheenen, T. W. J.; Punt, C. J. A.; Heerschap, A.; Figdor, C. G. *Nat. Biotechnol.* **2005**, *23*, 1407.)

1.3 Nanomaterials as Chemotherapeutic Agents

Nanoparticles are widely used as potential drug and gene delivery systems in clinical applications because they may overcome intrinsic problems of drug efficacy, allowing targeted delivery and passage through biological barriers.^[55] In particular, when nanoparticles are used as drug delivery vehicle, the accumulation of anticancer drugs to tumor tissue could be increased considerably through EPR effects because the blood vessels are frequently permeable and leaky, facilitating the accumulation of nanosized materials around tumor tissues.^[56] Active targeting by conjugating with antibody such as folic acid (FA) or methotrexate (MTX) for recognition by folate receptor which are overexpressed on the surface of many cancer cells, or peptides such as RGD to the tumor vasculature can be accomplished as well.^[57] Furthermore, various tailored nanomaterials including core-shell structure nanoparticles can perform additional functions of imaging capability or controlled drug release.^[58]

However, another promising application of nanomaterials as self-therapeutics has been recently demonstrated. Likewise, colloidal metal has seen medicinal use since ancient time, people have recently paid

attention to colloiddally stable nanoparticle therapeutics as an alternative platform in clinical settings. In particular, with development of versatile methods of tailoring size and physical properties of nanomaterials as well as innovative molecular design control, we can now take the utmost advantages of both dimensions and unexpected functions of the nanosized materials. However, it is necessary to design and engineer nanoparticles that can be targeted to tissues of interest, as well as to produce specific, desired effects with minimal toxicity to realize optimal therapeutic potentials. In this sense, the physiochemical parameters such as charge, size, and shape of nanoparticles as well as the nature of the binding ligand should be considered in order to minimize toxicity and increase the therapeutic index.

1.3.1 Nanoparticles as anticancer agents

One of the key factors in the growth and spread of tumor cells is angiogenesis, which is the process of new blood vessel and capillary formation. Blood vessels supply oxygen and other nutrients to tumor cells, allowing them to grow, migrate, and metastasize to different organs.^[59] Tumor angiogenesis is triggered by endothelial-specific

mitogens, such as vascular endothelial growth factor (VEGF), basic fibroblast growth factor (bFGF), and transforming growth factor-beta (TGF- β). Judah Folkman et al. proposed that angiogenesis contribute to the tumor growth and he pioneered the idea of treating cancer with anti-angiogenesis.^[60]

Mukherjee et al. tested the effect of gold nanoparticles (Au NPs) on VEGF mediated angiogenesis and demonstrated their anticancerous properties in a mouse ear model. In this study, naked gold nanoparticles inhibited the activity of heparin binding proteins, such as VEGF 165 and bFGF *in vitro* and VEGF induced angiogenesis *in vivo*. Herein, the angiogenic response found in tumors could be mimicked by injecting adenoviral vector of VEGF (ad-VEGF) (Figure 1.14).^[61]

Silver has also shown to exhibit anti-angiogenic effects. 40 nm silver nanoparticles (Ag NPs) were used and indicated their anti-angiogenic properties in bovine retinal epithelial cells (BREC) *in vitro* and in a matrigel plug assay *in vivo*.^[62]

Porcel et al. demonstrates that platinum nanoparticles may also have potential as therapeutics for cancer.^[63] The combination of fast ion radiation (hadron therapy) with Pt nanoparticles resulted in enhanced DNA strand breakage. The fast carbon ion irradiation of platinum led to

the production of HO^\bullet radicals and then amplifying the lethal damages to DNA. Human colon carcinoma cells (HT29) showed a dose and time dependent response when exposed to platinum nanoparticles.^[64] Pt^{2+} ions from the platinum nanoparticles are released in cellular endosomes and cause significant DNA damages and cellular apoptosis. Since platinum nanoparticles do not directly interact with DNA, the soluble species of Pt forms a complex with DNA, which is similar to that of cisplatin.^[65]

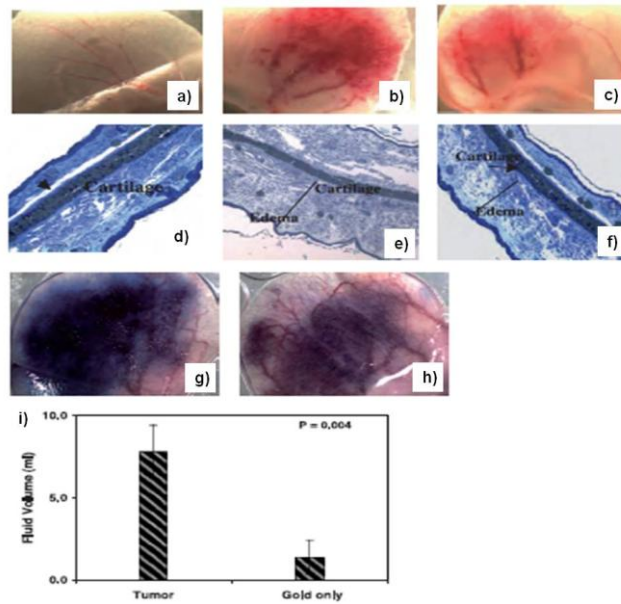


Figure 1.14. Effect of gold nanoparticles on angiogenesis *in vivo* in the ears of nude mice. Gross appearance of angiogenesis 7 days after injection of gold nanoparticles only a), Ad-VEGF only b), gold nanoparticles and ad-VEGF c). Giemsa stained 1 Amol/L epon sections of the ears were photographed at 10 magnifications, gold nanoparticles only d) Ad-VEGF only e), gold nanoparticles and ad-VEGF f). Effect of gold nanoparticles on permeability, Ad-VEGF only g), gold nanoparticles and ad-VEGF h), ascites fluid accumulation in the peritoneal cavity i). (from Ref. [61], Mukherjee, P.; Bhattachary, R.; Wang, P.; Wang, L.; Basu, S.; Nagy, J. A.; Atala, A.; Mukhopadhyay, D.; Soker, S. *Clinic. Cancer Res.* **2005**, *11*, 3530.)

1.3.2 Radical scavenging nanomaterials

Reactive oxygen and nitrogen species play a critical role in homeostasis. When these ROS/RNS production is excessive and radical scavenging is not sufficient, oxidative stress occurs and this might be involved in many human diseases.

Unexpectedly, nanoparticles acting as radical scavengers were found. Those are modified fullerenes and cerium oxide nanoparticles. Over the past ten year, various forms of these nanoparticles have been engineered and studied to decrease damages induced by reactive oxygen and nitrogen species in biological systems.

1.3.2.1 Oxidative stress in biological systems

In all human cells, free radicals are produced as byproducts of essential metabolic reactions such as energy generation reactions from mitochondria or the detoxification reactions, and occasionally cause the formation of reactive oxygen species (ROS).^[66] In particular, when imbalance in normal redox state of cells occurred by excessive ROS production and insufficient antioxidants, oxidative stress is induced in

biological systems. This oxidative stress leads to degenerative damage of DNA, proteins, and lipids, and is thought to be involved in the development of many diseases including cardiovascular diseases, neurodegenerative diseases, and cancers (Figure 1.15).^[67] However, since ROS is also considered as the essential endogenous participants in cell signal transduction pathways, basal ROS levels is necessary for cellular homeostasis and ROS levels should be properly controlled by exogenous or endogenous antioxidants.^[68]

In general, prevalent reactive oxygen species are superoxide ($O_2^{\bullet-}$), hydrogen peroxide (H_2O_2), and hydroxyl radical (HO^{\bullet}). There are antioxidant enzymes, such as superoxide dismutase (SOD), catalase and glutathione peroxidase, and low molecular weight antioxidants, such as ascorbate (vitamin C), α -tocopherol (vitamin E), and glutathione (GSH).^[69] SOD transforms superoxide into H_2O_2 in a dismutation reaction, and H_2O_2 is eliminated by catalase in a second dismutation reaction. As shown in Figure 1.16, catalase/glutathione peroxidase and SOD are particularly known as the most efficient two enzymes due to their relatively high reactivity and rapid diffusion.

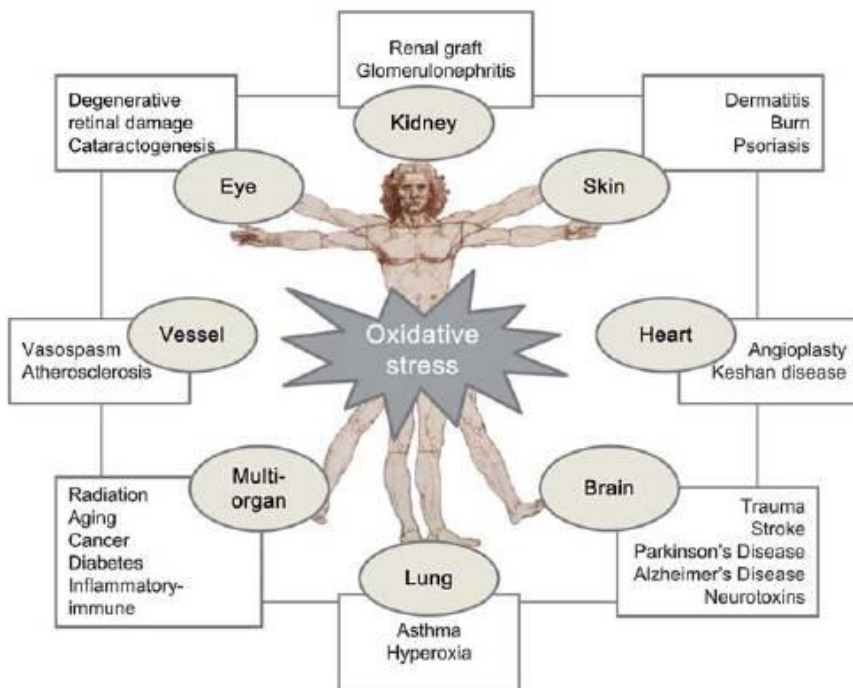


Figure 1.15. Oxidative stress and human pathology. Oxidative stress is involved in many human diseases, which are caused by deregulated and aberrant free radical production or insufficient radical scavenging. For this reason, the development of antioxidant therapies is emphasized. (from Ref. [67], Celardo, I.; Pedersen, J. Z.; Traversa, E.; Ghibelli, L. *Nanoscale*, **2011**, 3, 1411.)

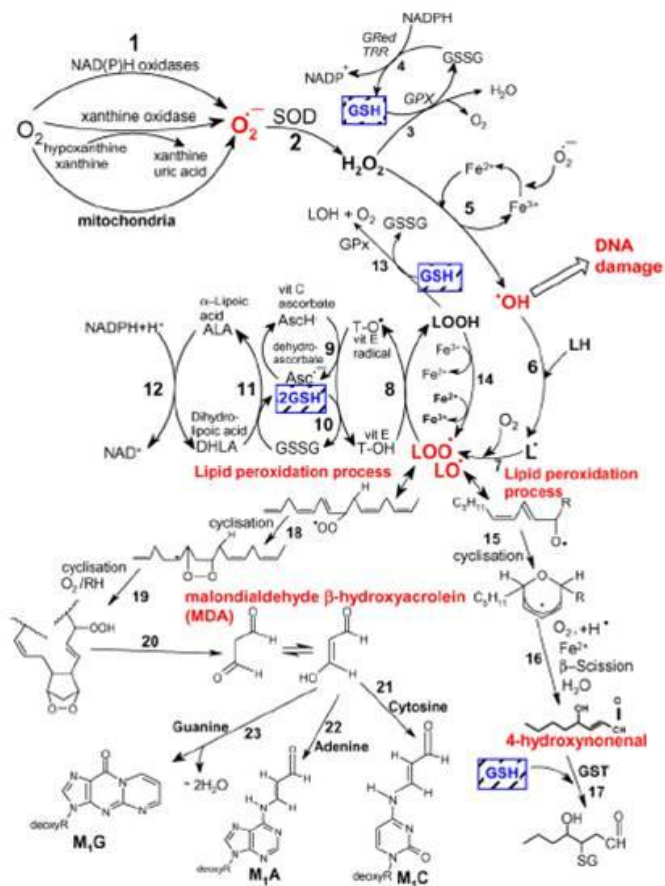


Figure 1.16. Pathways of ROS formation, the lipid peroxidation process, and the role of SOD, glutathione (GSH)/catalase, and other antioxidants (Vitamin E, Vitamin C, lipoic acid) in the management of oxidative stress. (from Ref. [69b], Valko, M.; Leibfritz, D.; Moncol, J.; Cronin, M. T. D.; Mazur, M.; Telser J.; *Int. J. Biochem. Cell Biol.* **2007**, 39, 44.)

1.3.2.2 Fullerenes and fullerene derivatives

Several studies have been conducted by using water soluble derivatives of fullerenes as radical scavenging nanomaterials and have shown that administration of fullerenes can effectively prevent biological injury caused by reactive oxygen species.

For the first time, carboxyfullerenes were administered to wild type and mutant SOD (G93A) animals, a model for amyotrophic lateral sclerosis (ALS). It was suggested that carboxyfullerenes had inhibited an imbalance between ROS production and defense by scavenging superoxide, and delayed death.^[70]

Lipid peroxidation which is a symptom of oxidative stress to cell was studied *in vitro*, and polar and non-polar fullerene derivatives were shown to prevent lipid peroxidation induced by HO^\bullet and $\text{O}_2^{\bullet-}$.^[71] Fullerenes also decreased the enzyme activities associated with the metabolism of reactive oxygen species (ROS) in tumor bearing mice (Figure 1.17).^[72] Particularly, comprehensive mechanism is also proposed. Using electron spin resonance (ESR), it was confirmed that ROS scavenging by fullerene is a catalytic reaction because no structural changes of fullerene is observed.

Lai et al. demonstrated that water-soluble fullerenes act as effective antioxidants and significantly reduced ischemia-reperfusion-induced lung injury. Excessive reactive oxygen species are produced which damage cellular components during ischemia–reperfusion period.^[73] Carboxyfullerenes were also shown to prevent neuronal injuries against a neurotoxin, 1-methyl-4-phenyl-pyridinium (MPP+).^[74]

Very recently, amine modified carbon nanotubes (CNT) injected intravenously in ischemia–reperfusion stroke injury model, demonstrated to reduce oxidative stress and exerts the cellular protective effects.^[75]

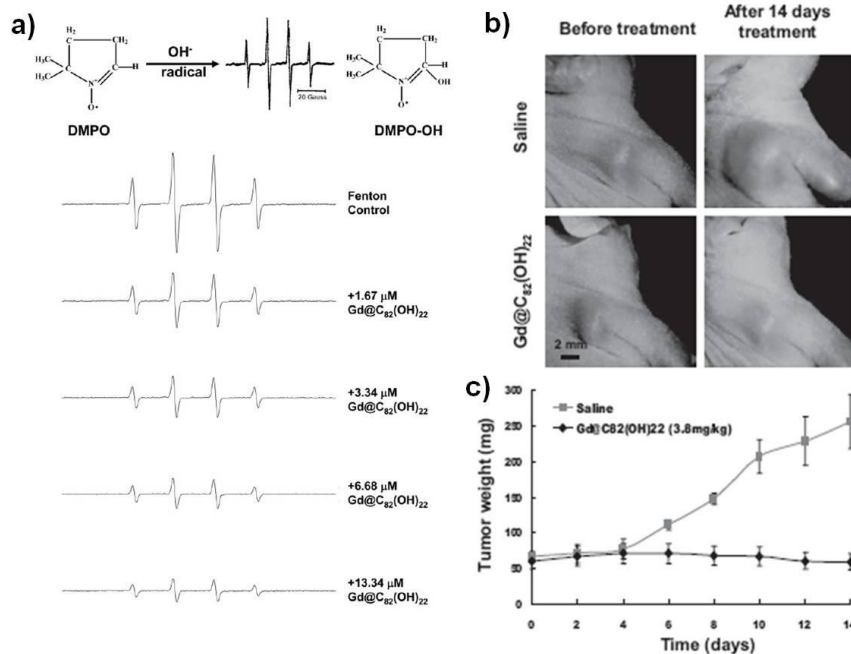


Figure 1.17. a) ESR signals of hydroxyl radicals generated by Fenton reaction and scavenged by $[Gd@C_{82}(OH)_{22}]_n$ nanoparticles measured 6 min after initiating generation of HO^\cdot . b) Treatment of tumor. c) Tumor growth inhibition by $[Gd@C_{82}(OH)_{22}]_n$ nanoparticles compared with saline group. (from Ref. [72], Yin, J.-J.; Lao, Meng, J.; Fu, P. P.; Zhao, Y.; Xing, G.; Gao, X.; Sun, B.; Wang, P.C.; Chen, C.; Liang, X.-J. *Mol. Pharmacol.* **2008**, 74, 1132.)

1.3.2.3 Ceria nanoparticles as potential antioxidants

Cerium oxide (Ceria) nanoparticles (5-30 nm), tend to have oxygen vacancies at the nanoparticle surfaces, which results in mixed valence of cerium(IV) and cerium(III) oxidation states.^[76] Interestingly, valence switching between these two oxidation states happens reversibly and this resembles the mechanism of redox enzymes to catalyze reversible redox reactions in cells and tissues by using metals as co-factors.^[77] In particular, ceria nanoparticles have received much attention as potential antioxidant agents *in vitro* and *in vivo*, because they are highly biocompatible and can regenerate the initial oxidation state through redox cycling reactions.^[78]

Ceria nanoparticles basically act as SOD mimetic enzymes which oxidize superoxide and produce peroxide. Because Ce^{3+} mostly contributes the reduction of superoxide, it requires a high $\text{Ce}^{3+}/\text{Ce}^{4+}$ ratio to have better SOD mimetics.^[79] However, it was recently found that ceria nanoparticles can react with H_2O_2 in an additional way,^[80] which is very important implication in terms of radical scavenging *in vivo*. This mechanism involves H_2O_2 reaction with Ce^{4+} , which is reduced to Ce^{3+} with the concomitant oxidation of H_2O_2 to molecular

O₂ by a reaction similar to that of catalase.

To sum up, when ceria nanoparticle reduces superoxide, H₂O₂ is formed and Ce³⁺ is oxidized to Ce⁴⁺; then Ce⁴⁺ and H₂O₂ can react together to regenerate Ce³⁺ and oxidize H₂O₂ to O₂ (Figure 1.18). This would be a very elegant way of regenerating reduced ceria nanoparticles and sequentially eliminating both superoxide and hydrogen peroxide.

The combination of these two SOD and catalase mimetic functions of ceria nanoparticles makes them to be very attractive biological ROS scavengers because they can scavenge two abundant types of ROS ceaselessly.

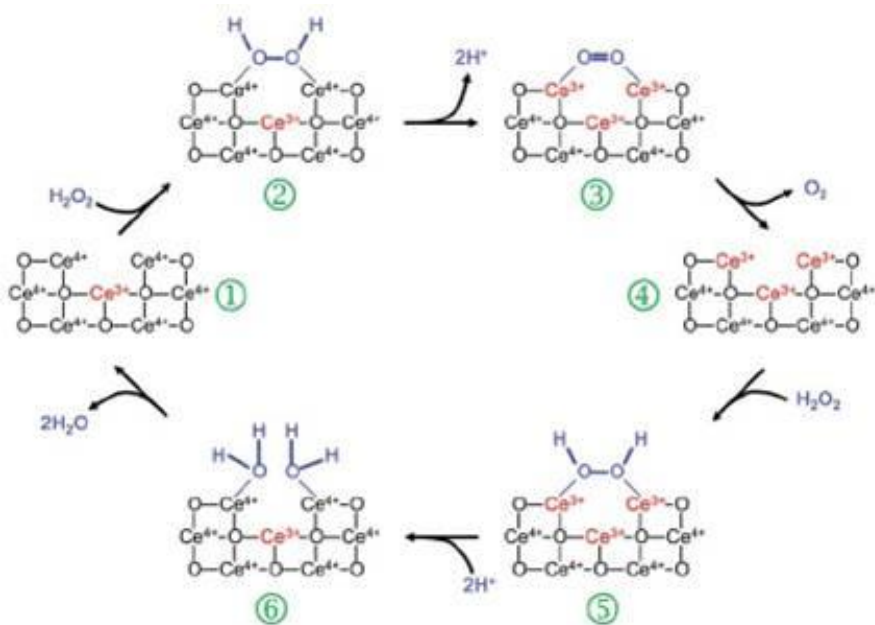


Figure 1.18. A model reaction mechanism for the complete dismutation of hydrogen peroxide. The oxidative half-reaction is identical to the sequence shown in 1) – 4). The reductive half involves binding of H₂O₂ to the 2 Ce³⁺ site 5), uptake of two protons and homolysis of the O–O bond with transfer of electrons to the two Ce³⁺ 6), and release of the water molecules to regenerate the initial Ce⁴⁺ site 1). This reaction sequence would be analogous to the one found in catalases. (from Ref. [80b], Celardo, I.; Pedersen, J. Z.; Traversa E.; Ghibelli L. *Nanoscale* **2011**, 3, 1411.)

1.3.2.4 Biological effects of ceria nanoparticles *in vitro* and *in vivo*

The protective effects of ceria nanoparticles *in vitro*, including established cell lines and primary cultures from tumors or normal tissues have been studied. In this set of studies, ceria nanoparticles decreased both endogenous and induced ROS, and preserved the viability of damaged cells. Several studies to prove ceria nanoparticle as antioxidants in animal models have also been conducted.

Ceria nanoparticles were found to scavenge free radicals in murine insulinoma cells treated with hydroquinone.^[81] In murine macrophages stimulated with lipopolysaccharide (LPS), ceria nanoparticles reduced the LPS-dependent ROS production and associated cell activation, without alleviating LPS-induced macrophage death.^[82] Neuroprotective effect of ceria nanoparticles demonstrated to have prevention from hydrogen peroxide mediated injury to spinal cord neurons (Figure 1.19).^[83] In a pioneering study, ceria nanoparticles were injected into transgenic mice expressing monocyte chemo-attractant protein-1 (MCP-1) in the cardiac tissue. These mice develop myocardial inflammation leading to fatal ischemic cardiomyopathy. Ceria nanoparticle injection alleviated many clinical symptoms of these mice,

due to its radical scavenging properties to reduce inflammation (Figure 1.20).^[84]

Ceria nanoparticle administration to animals can protect organ functions after specific stimulus. This includes protection from radiation induced pneumonitis,^[85] or gastro-intestinal epithelial damage,^[86] and from peroxide-induced retinal degeneration.^[87] X-ray irradiations evoke secondary oxidative stress and induce tissue damages, and ROS scavenging ability of ceria nanoparticles can relieve these damages. Intravitreal injection of ceria nanoparticles prevented light-induced degradation of rat retina photoreceptor cells (Figure 1.21).

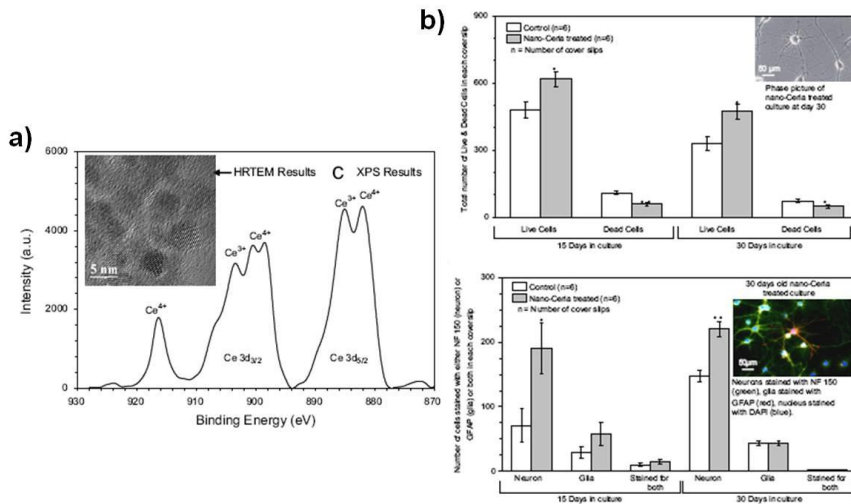


Figure 1.19. a) XPS analysis and HRTEM images of the synthesized ceria nanoparticles. b, c) Live–dead assay and neuron–glial cell assay studies of control ceria nanoparticles-treated cultures of adult rat spinal cord. b) Live–dead cell assays indicated that ceria nanoparticles-treated cultures had significantly higher cell survival and less cell death on day 15 and day 30 in culture as compared to the control cultures. c) Neuron–glial cell assays indicated that a significantly high neuronal survival in treated cultures on day 15 and day 30 as compared to the control cultures. (from Ref. [83], Das, M.; Patil, S.; Bhargava, N.; Kang, J.-F.; Riedel, L. M.; Seal, S.; Hickm, J. J. *Biomaterials* **2007**, *28*, 1918.)

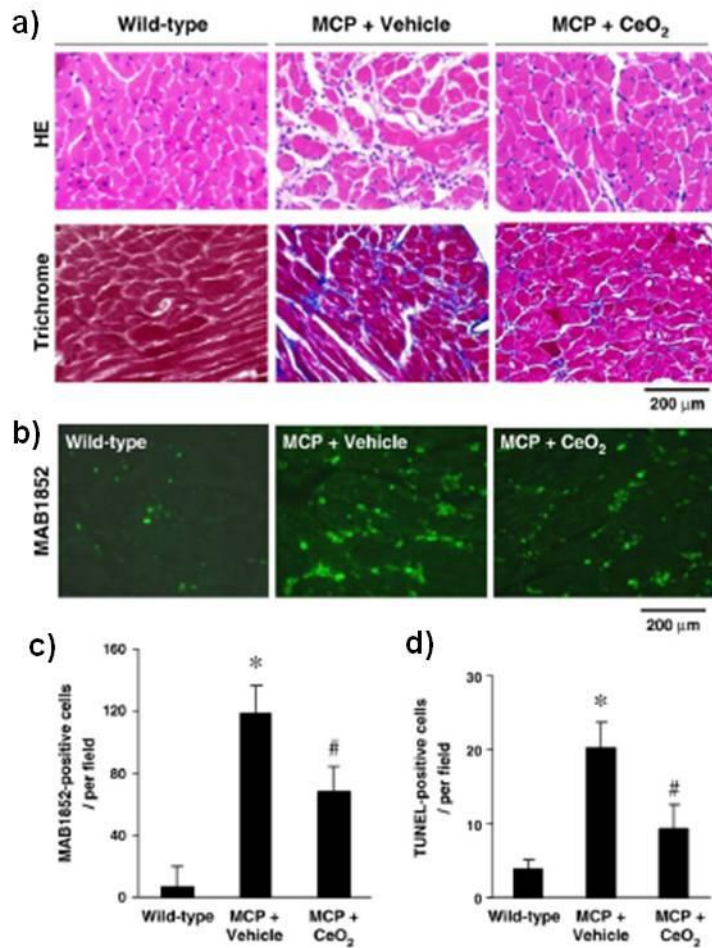


Figure 1.20. Effects of ceria nanoparticles on myocardial inflammation.

a) Histopathological photomicrographs of Left Ventricular (LV) obtained from wild-type control, vehicle- and ceria nanoparticles-treated MCP mice. Upper panel: H&E staining; lower panel: Masson's trichrome staining, blue represents collagen deposition. b) Representative immunohistochemical photographs of monocyte/macrophage

infiltration in the myocardium. Green denotes infiltrated monocytes/macrophages. c, d) Histograms showing the number of MAB1852-positive cells and TUNEL-positive cells in the myocardium of different group of mice, respectively. (from Ref. [84], Niu, J.; Azfer, A.; Rogers, L. M.; Wang, X.; Kolattukudy, P. E. *Cardiovas. Res.* **2007**, *73*, 549.)

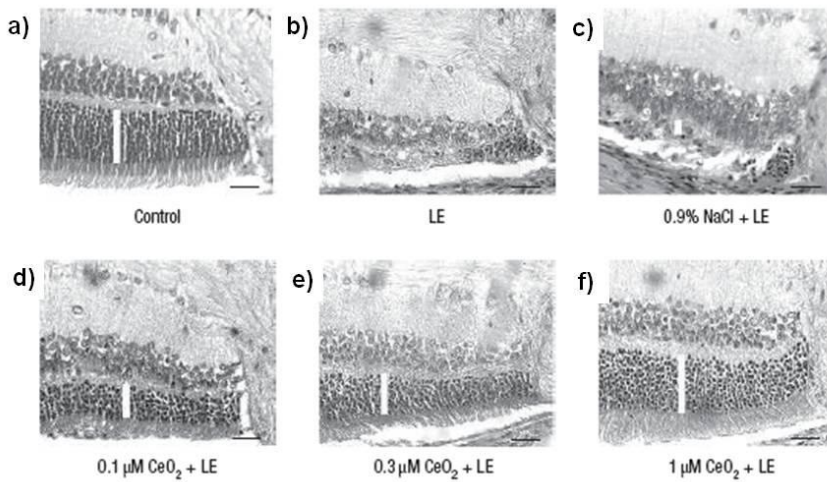


Figure 1.21. Intravitreal injection of ceria nanoparticles protects rat retina photoreceptor cells from light-induced degeneration. Representative images show H&E stained sections adjacent to the optic nerve. The white bars indicate the thickness of the layer of nuclei of rods and cones. Injection of ceria nanoparticles were performed on day 0, rats were exposed to light on day 3, and the experiment ended on day 10. a) No light exposure (LE), no injection. b–f) Rats were exposed to 6 h of 2,700 lux white light. No injection b), injections of saline c), 0.1 mM ceria d), 0.3 mM ceria e), and 1.0 mM ceria f), 3 days before LE. The scale bars = 25 mm. (from Ref. [87], Chen, J.; Patil, S.; Seal S.; McGinnis, J. F.; *Nat. Nanotechnol.* **2006**, *1*, 142.)

1.4 References

- [1] a) Ma, X.; Zhao, Y.; Liang, X-J. *Acc. Chem. Res.* **2011**, *44*, 1144. b) Petrod, R. A.; DeSimone, J. M. *Nat. Rev. Drug Discover.* **2010**, *9*, 615.
- [2] a) A. P. Alivisatos, *Nat. Biotechnol.* **2004**, *22*, 47. b) N. L. Rosi, C. A. Mirkin, *Chem. Rev.* **2005**, *105*, 1547. c) K. J. Klabunde, *Nanoscale Materials in Chemistry*, Wiley-Interscience, New York, **2001**. d) C. M. Niemeyer, *Angew. Chem. Int. Ed.* **2001**, *40*, 4128. e) X. Michalet, F. F. Pinaud, L. A. Bentolila, J. M. Tsay, S. Doose, J. J. Li, G. Sundaresan, A. M. Wu, S. S. Gambhir, S. Weiss, *Science* **2005**, *307*, 538.
- [3] Farokhzad, O. C.; Langer, R. *Adv. Drug Deliv. Rev.* **2006**, *58*, 1456.
- [4] Lavik, E.; von Recum, H. *ACS Nano* **2011**, *5*, 3419.
- [5] a) Sun, C.; Lee J. S.; Zhang, M. *Adv. Drug Delivery Rev.* **2008**, *60*, 1252.
b) Veiseh, O.; Gunn, J. W.; Zhang, M. *Adv. Drug Delivery Rev.* **2010**, *62*, 284.
- [6] a) Liechty, K. W.; MacKenzie, T. C. Shaaban, A. F.; Radu, A.; Moseley, A. B.; Deans, R.; Marshark, D. R.; Flake, A. W. *Nat. Med.* **2000**, *6*, 1282.
b) Pittenger, M. F.; Mackay, A. M.; Beck, S. C.; Jaiswal, R. K.; Douglas, R.; Mosca, D.; Moorman, M. A.; Simonetti, D. W.; Craig, S.; Marshak D. R. *Science* **1999**, *284*, 143.

- [7] a) Boheler, K. R.; Czyz, J.; Tweedie, D.; Yang, H.-T.; Anisimov, S. V.; Wobus, A. M. *Circ. Res.* **2002**, *91*, 189. b) Carpenter, M. K.; Frey-Vasconcells, J.; Rao, M. S. *Nat. Biotechnol.* **2009**, *27*, 606. c) Marin-Garcia, J.; Goldenthal, M. J. *Curr. Stem Cell Res. Ther.* **2006**, *1*, 1. d) J. F.; Anderson, S. A.; Adler, E.; Frank, J. A. *Nat. Rev. Cardiol.* **2010**, *7*, 97.
- [8] Solanki, A.; Kim, J. D.; Lee, K.-B. *Nanomedicine* **2008**, *3*, 567.
- [9] a) Hart, L. S.; El-Deiry, W. S. *J. Clin. Oncol.* **2008**, *26*, 2901. b) Corot, C.; Robert, P.; Idee, J. M.; Port, M. *Adv. Drug Delivery Rev.* **2006**, *58*, 1471.
- [10] Berman, S. M. C.; Walczak, P.; Bulte, J. W. *Wiley Interdiscip. Rev. Nanomed. Nanobiotechnol.* **2011**, *3*, 343.
- [11] Kircher, M. F.; Gambhir, S. S.; Grimm, J. *Nat. Rev. Clin. Oncol.* **2011**, *8*, 677.
- [12] Janowski, M.; Bulte, J. W.; Walczak P. *Adv. Drug Deliv. Rev.* **2011**, *64*, 1488.
- [13] a) Weissleder, R.; Pittet, M. J. *Nature* **2008**, *452*, 580. b) Willmann, J. K.; van Bruggen, N.; Dinkelborg L. M.; Gambhir, S. S. *Nat. Rev. Drug Discover.* **2008**, *7*, 591.
- [14] a) Na, H. B.; Hyeon T. *J. Mater. Chem.* **2009**, *19*, 6267. b) Na, H. B.; Song, U. C.; Hyeon, T. *Adv. Mater.* **2009**, *21*, 2133.
- [15] a) Long, C.M.; Bulte, J. W. *Expert Opin. Biol. Ther.* **2009**, *9*, 293. b)

- Bulte, J. W.; Kraitchman, D. L. *NMR Biomed.* **2004**, *17*, 484.
- [16] a) Schwenzer, N. F.; Springer, F.; Schraml, C.; Stefan, N.; Machann, J.; Schick, F. *J. Hepatol.* **2009**, *51*, 433. b) Yu S.-B.; Watson A. D. *Chem. Rev.* **1999**, *99*, 2353. c) Shilo, M.; Reuveni, T.; Motiei, M.; Popovtzer, R. *Nanomedicine* **2012**, *7*, 257.
- [17] a) Eck, W.; Nicholson, A. I.; Zentgraf, H.; Semmler, W.; Bartling, S. *Nano Lett.* **2010**, *10*, 2318. b) Reuveni, T.; Motiei, M.; Romman, Z.; Popovtzer, A.; Popovtzer, R. *Int. J. Nanomed.* **2011**, *6*, 2859.
- [18] Ricles, L. M.; Nam, S. Y.; Sokolov, K.; Emelianov, S. Y.; Suggs, L. J. *Int. J. Nanomedicine* **2011**, *6*, 407.
- [19] a) Hainfeld, J. F.; Slatkin, D. N.; Focella, T. M.; Smilowitz, H. M. *Br. J. Radiol.* **2006**, *79*, 248. b) Boote, E.; Fent, G.; Kattumuri, V.; Casteel, S.; Katti, K.; Chanda, N.; Kannan, R.; Churchill, R. *Acad. Radiol.* **2010**, *17*, 410. c) Cormode, D. P.; Roessl, E.; Thran, A.; Skajaa, T.; Gordon, R. E.; Schlomka, J. P.; Fuster, V.; Fisher, E. A.; Mulder, W. J.; Proksa, R.; Fayad, Z. A. *Radiology* **2010**, *256*, 774.
- [20] a) Lee, W. W.; Marinelli, B.; van der Laan, A. M.; Sena, B. F.; Gorbatov, R.; Leuschner, F.; Dutta, P.; Iwamoto, Y.; Ueno, T.; Begieneman, M. P.; Niessen, H. W.; Piek, J. J.; Vinegoni, C.; Pittet, M. J.; Swirski, F. K.; Tawakol, A.; Carli, M. D.; Weissleder, R.; Nahrendorf, M. *J. Am. Coll.*

- Cardiol.* **2012**, *59*, 153. b) Maramraju, S. H.; Smith, S. D.; Junnarkar, S. S.; Schulz, D.; Stoll, S.; Ravindranath, B.; Purschke, M. L.; Rescia, S.; Southekal, S.; Pratte, J. F.; Vaska, P.; Woody, C. L.; Schlyer, D. *J. Phys. Med. Biol.* **2011**, *56*, 2459.
- [21] Sutton, E. J.; Henning, T. D.; Pichler, B. J.; Bremer, C. Daldrup-Link, H. E. *Eur. Radiol.* **2008**, *18*, 2021.
- [22] Boddington, S.; Henning, T. D.; Sutton, E. J.; Daldrup-Link, H. E. *J. Vis. Exp.* **2008**, *14*, 686.
- [23] Zhou, J.; Liu, Z.; Li, F. *Chem. Soc. Rev.* **2012**, *41*, 1323.
- [24] Stark, D. D.; Weissleder, R.; Elizondo, G.; Hahn, P. F.; Saini, S.; Todd, L. E.; Wittenberg, J.; Ferrucci, J. T. *Radiology* **1988**, *168*, 297.
- [25] Xie, J.; Wang, J.; Niu, G.; Huang, J.; Chen, K.; Li, X.; Chen, X. *Chem. Commun.* **2010**, *46*, 433.
- [26] Matuszewski, L.; Persigehl, T.; Wall, A.; Schwindt, W.; Tombach, B.; Fobker, M.; Poremba, C.; Ebert, W.; Heindel, W.; Bremer, C. *Radiology* **2005**, *235*, 155.
- [27] Basly, B.; Felder-Flesch, D.; Perriat, P.; Billotey, C.; Taleb, J.; Pourroy, G.; Begin-Colin, S. *Chem. Commun.* **2010**, *46*, 985.
- [28] Seymour, L.; Schacht, E.; Duncan, R. *Cell Biol. Int. Rep.* **1991**, *15*, 277.
- [29] a) Lee, J.-H.; Huh, Y.-M.; Jun, Y.-W.; Seo, J. W.; Jang, J. T.; Song, H.-T.;

- Kim, S.; Cho, E.-J.; Yoon, H.-G.; Suh, J. S.; Cheon J. *Nat. Med.* **2006**, *13*, 95. b) Lee, N.; Kim, H.; Choi, S. H.; Park, M.; Kim, D.; Kim, H.-C.; Choi, Y.-S.; Lin, S.; Kim, B. H.; Jung, H. S.; Kim, H.; Park, K. S.; Moon W. K.; Hyeon, T. *Proc. Natl. Acad. Sci. U.S.A.* **2011**, *108*, 2662.
- [30] Tseng, C.-L.; Shih, I. L.; Stobinski, L.; Lin, F.-H. *Biomaterials* **2010**, *31*, 5427.
- [31] Gilad, A. A.; Walczak, P.; McMahon, M. T.; Na, H. B.; Lee, J. H.; An, K.; Hyeon, T.; van Zijl, P. C. M.; Bulte, J. W. M. *Magn. Reson. Med.* **2008**, *60*, 1.
- [32] Shukla, R.; Bansal, V.; Chaudhary, M.; Basu, A.; Bhonde, R. R.; Sastry, M. *Langmuir* **2005**, *21*, 10644.
- [33] a) Hainfeld, J. F.; O'Connor, M. J.; Dilmanian, F. A.; Slatkin, D. N.; Adams, D. J.; Smilowitz, H. M. *Br. J. Radiol.* **2011**, *84*, 526. b) Menk, R. H.; Schultke, E.; Hall, C.; Arfelli, F.; Astolfo, A.; Rigon, L.; Round, A.; Ataelmannan, K.; MacDonald, S. R.; Juurlink, B. H. *Nanomedicine* **2011**, *7*, 647.
- [34] a) Rabin, O.; Perez, J. M.; Grimm, J.; Wojtkiewicz, G.; Weissleder, R. *Nat. Mater.* **2006**, *5*, 118. b) Liu, Y.; Ai, K.; Liu, J.; Yuan, Q.; He, Y.; Lu, L. *Angew. Chem. Int. Ed.* **2012**, *51*, 1437. c) Oh, M. H.; Lee, N.; Kim, H.; Park, S. P.; Piao, Y.; Lee, J.; Jun, S. W.; Moon, W. K.; Choi, S. H.; Hyeon,

- T. *J. Am. Chem. Soc.* **2007**, *133*, 5508. d) Bonitatibus Jr., P. J.; Torres, A. S.; Goddard, G. D.; FitzGerald, P. F.; Kulkarni, A. M. *Chem. Commun.* **2010**, *46*, 8956.
- [35] Shah, B. S.; Moiola E. K.; Stroschio M. A.; Mao J. J. *Nano Lett.* **2007**, *7*, 3071.
- [36] Sugiyama, T.; Kuroda, S.; Osanai, T.; Shichinohe, H.; Kuge, Y.; Ito, M.; Kawabori, M.; Iwasaki, Y. *Neurosurgery* **2011**, *68*, 1036.
- [37] a) Hilderbrand, S. A.; Shao, F.; Salthouse, C.; Mahmood, U.; Weissleder, R. *Chem. Commun.* **2009**, 4188. b) Zhou, J.; Liu, Z.; Li, F. *Chem. Soc. Rev.* **2012**, *41*, 1323.
- [38] a) Wang, F.; Banerjee, D.; Liu, Y.; Chen, X.; Liu, X. *Analyst*, **2010**, *135*, 1839. b) Idris, N. M.; Li, Z.; Ye, L.; Sim, E. K. W.; Mahendran, R.; Ho P. C.-L.; Zhang, Y. *Biomaterials* **2009**, *30*, 5104.
- [39] a) Blasberg, R. G. *Nucl. Med. Biol.* **2003**, *30*, 879. b) Lee, H.-Y.; Li, Z.; Chen, K.; Hsu, A. R.; Xu, C.; Xie, J.; Sun, S.; Chen, X. *J. Nucl. Med.* **2008**, *49*, 1371. c) Choi, J.-S.; Park, J. C.; Nah, H.; Woo, S.; Oh, J.; Kim, K. M.; Cheon, G. J.; Chang, Y.; Yoo, J.; Cheon, J. *Angew. Chem. Int. Ed.*, **2008**, *47*, 6259. d) Jennings, L. E.; Long, N. J. *Chem. Commun.* **2009**, 3511.
- [40] Patel, D.; Kell, A.; Simard, B.; Xiang, B.; Lin, H. Y.; Tian, G.

Biomaterials **2011**, *32*, 1167.

- [41] Lu, C.-W.; Hung, Y.; Hsiao, J.-K.; Yao, M.; Chung, T.-H.; Lin, Y.-S.; Wu, S.-H.; Hsu, S.-C.; Liu, H.-M.; Mou, C.-Y.; Yang, C.-S.; Huang, D.-M.; Chen, Y.-C. *Nano Lett.* **2007**, *7*, 149
- [42] Shi, Z.; Neoh, K. G.; Kang, E. T.; Shuter, B.; Wang, S.-C. *Contrast Media Mol. Imaging* **2010**, *5*, 105.
- [43] a) Narayanan, S.; Sathy, B. N.; Mony, U.; Koyakutty, M.; Nair, S. V.; Menon, D. *ACS Appl. Mater. Interfaces* **2012**, *4*, 251. b) Lee, N. Cho, H. R.; Oh M. H.; Lee, S. H.; Kim, K.; Kim, B. H.; Shin, K.; Ahn, T.-Y.; Choi, J. W.; Kim, Y.-W.; Choi, S. H.; Hyeon, T. *J. Am. Chem. Soc.* **2012**, *134*, 10309.
- [44] a) Kim, H. M.; Lee, H.; Hong, K. S.; Cho, M. Y.; Sung, M. H.; Poo, H.; Lim, Y. T. *ACS Nano* **2011**, *5*, 8230. b) Cha, E. J.; Jang, E. S.; Sun, I. C.; Lee, I. J.; Ko, J. H.; Kim, Y. I.; Kwon, I. C.; Kim, K.; Ahn, C. H. *J. Control. Release* **2011**, *155*, 152.
- [45] a) Arbab, A. S.; Yocum, G. T.; Kalish, H.; Jordan, E. K.; Anderson, S. A.; Khakoo, A. Y.; Read, E. J.; Frank, J. A. *Blood* **2004**, *104*, 1217. b) Frank, J. A.; Miller, B. R.; Arbab, A. S.; Zywicke, H. A.; Jordan, E. K. Lewis, B. K.; Bryant, L. H. Bulte, J. W. *Radiology* **2003**, *228*, 480. c) Bulte, J. W.; Douglas, T.; Witwer, B.; Zhang, S. C.; Strable, E.; Lewis, B. K.; Zywicke,

- H.; Miller, B.; van Gelderen, P.; Moskowitz, B. M. et al. *Nat. Biotechnol.* **2001**, *19*, 1141.
- [46] a) Walczak, P.; Kedziorek, D. A.; Gilad, A. A.; Lin, S.; Bulte, J. W. *Magn. Reson. Med.* **2005**, *54*, 769. b) Walczak, P.; Ruiz-Cabello, J.; Kedziorek, D. A.; Gilad, A. A.; Lin, S.; Barnett, B.; Qin, L.; Levitsky, H.; Bulte, J. W. *Nanomedicine* **2006**, *2*, 89.
- [47] a) Qiu, B.; Xie, D.; Walczak, P.; Li, X.; Ruiz-Cabello, J.; Minoshima, S.; Bulte, J. W.; Yang, X. *Magn. Reson. Med.* **2010**, *63*, 1437. b) Xie, D.; Qiu, B.; Walczak, P.; Li, X.; Ruiz-Cabello, J.; Minoshima, S.; Bulte, J. W.; Yang, X. *NMR Biomed.* **2010**, *23*, 480.
- [48] a) Josephson, L.; Tung, C. H.; Moore, A.; Weissleder, R. *Bioconjugate Chem.* **1999**, *10*, 186. b) Lewin, M.; Carlesso, N.; Tung, C. H.; Tang, X. W.; Cory, D.; Scadden, D. T.; Weissleder, R. *Nat. Biotechnol.* **2000**, *18*, 410.
- [49] Ahrens, E. T.; Feili-Hariri, M.; Xu, H.; Genove G.; Morel, P. A. *Magn. Reson. Med.* **2003**, *49*, 1006.
- [50] a) Amsalem, Y.; Mardor, Y.; Feinberg, M. S.; Landa, N.; Miller, L.; Daniels, D.; Ocherashvili, A.; Holbova, R.; Yosef, O.; Barbash, I. M. Leor, J. *Circulation* **2007**, *116*, 38. b) Amado, L. C.; Saliaris, A. P.; Schuleri, K. H.; St. John, M.; Xie, J. S.; Cattaneo, S.; Durand, D. J.;

- Fitton, T.; Kuang, J. Q.; Stewart, G. et al. *Proc. Natl. Acad. Sci. USA* **2005**, *102*, 11474.
- [51] a) Kim, D.; Chun, B. G.; Kim, Y. K.; Lee, Y. H.; Park, C. S.; Jeon, I.; Cheong, C.; Hwang, T. S.; Chung, H.; Gwag, B. J. et al. *Cell Transplant* **2008**, *16*, 1007. b) Hoehn, M.; Kustermann, E.; Blunk, J. Wiedermann, D.; Trapp, T.; Wecker, S.; Focking, M.; Arnold, H.; Hescheler, J.; Fleischmann, B. K.; Schwindt, W.; Buhrle, C. *Proc. Natl. Acad. Sci. USA* **2002**, *99*, 16267.
- [52] a) Bulte, J. W.; Ben-Hur, T.; Miller, B. R.; Mizrachi-Kol, R.; Einstein, O.; Reinhartz, E.; Zywicke, H. A.; Douglas, T.; Frank, J. A. *Magn. Reson. Med.* **2003**, *50*, 201. b) Muja, N.; Bulte, J. W. *Prog. Nucl. Magn. Reson. Spectrosc.* **2009**, *55*, 61.
- [53] a) Zhu, J.; Zhou, L.; Wu, F. X. *N. Engl. J. Med.* **2006**, *355*, 2376. b) Bulte, J. W. *AJR Am. J. Roentgenol.* **2009**, *193*, 314. c) McColgan, P.; Sharma, P.; Bentley, P. *Stem Cell Rev.* **2011**, *7*, 1031.
- [54] de Vries, I. J.; Lesterhuis, W. J.; Barentsz, J. O.; Verdijk, P.; van Krieken, J. H.; Boerman, O. C.; Oyen, W. J.; Bonenkamp, J. J.; Boezeman, J. B.; Adema, G. J.; Bulte, J. W.; Scheenen, T. W.; Punt, C. J.; Heerschap, A.; Figdor, C. G. *Nat. Biotechnol.* **2005**, *23*, 1407.
- [55] a) Davis, M. E.; Chen, Z.; Shin, D. M. *Nat. Rev. Drug Discover.* **2008**, *7*,

771. b) Gu, X.; Huang, L. *Acc. Chem. Res.* **2012**, *45*, 971.
- [56] Cho, K.; Wang, X.; Nie, S.; Chen, Z.; Shin, D. M. *Clin. Cancer Res.* **2008**, *14*, 1310.
- [57] a) Liong, M.; Lu, J.; Kovochich, M.; Xia, T.; Ruehm, S. G.; Nel, A. E.; Tamanoi, F.; Zink, J. I. *ACS Nano* **2008**, *2*, 889. b) Taylor, K. M. L.; Rieter, W. J.; Lin W. *J. Am. Chem. Soc.* **2008**, *130*, 14358.
- [58] a) Kim, J.; Kim, H.; Lee, N.; Kim, T.; Kim, H., Yu, T.; Song, I.; Moon, W.; Hyeon, T. *Angew. Chem. Int. Ed.* **2008**, *47*, 8438. b) Kim, J.; Lee, J. E.; Lee, S. H.; Yu, J. H.; Lee, J. H.; Park, T. G.; Hyeon, T. *Adv. Mater.* **2008**, *20*, 478.
- [59] a) Ferrara, N.; Kerbel, R. S. *Nature* **2005**, *438*, 964. b) Ferrara, N.; Mass, R. D.; Campa C.; Kim, R. *Annu. Rev. Med.* **2007**, *58*, 491. c) Dvorak, H. *F. J. Clin. Oncol.* **2002**, *20*, 4368.
- [60] Tosetti, B. R.; Albini, A. *Suppl Tumori*, **2002**, *1*, 9.
- [61] Mukherjee, P.; Bhattacharya, R.; Wang, P.; Wang, L.; Basu, S.; Nagy, J. A.; Atala, A.; Mukhopadhyay D.; Soker, S. *Clin. Cancer Res.* **2005**, *11*, 3530.
- [62] Gurunathan, S.; Lee, K.-J.; Kalishwaralal, K.; Sheikpranbabu, S.; Vaidyanathan, R.; Eom, S. H. *Biomaterials* **2009**, *30*, 6341.
- [63] Porcel, E.; Liehn, S.; Remita, H.; Usami, N.; Kobayashi, K.; Furusawa,

- Y.; Le Sech, C.; Lacombe, S. *Nanotechnology* **2010**, *21*, 085103.
- [64] Pelka, J.; Gehrke, H.; Esselen, M.; Turk, M.; Crone, M.; Brase, S.; Muller, T.; Blank, H.; Send, W.; Zibat, V.; Brenner, P.; Schneider, R.; Gerthsen, D.; Marko, D. *Chem. Res. Toxicol.* **2009**, *22*, 649.
- [65] Ahmadi, T. S.; Wang, Z. L.; Green, T. C.; Henglein, A.; El-Sayed, M. A. *Science* **1996**, *272*, 1924.
- [66] Cadenas, E.; Davies, K. J. *Free Radical Biol. Med.* **2000**, *29*, 222.
- [67] Celardo, I.; Pedersen, J. Z.; Traversa, E.; Ghibelli, L. *Nanoscale* **2011**, *3*, 1411.
- [68] a) Droge, W. *Physiol. Rev.* **2002**, *82*, 47. b) Holbrook, N. J.; Ikeyama, S. *Biochem. Pharmacol.* **2002**, *64*, 999.
- [69] a) Halliwell, B.; Gutteridge, J. *Free Radicals in Biology and Medicine*, Oxford University Press, Oxford, 4th edn, **2007**. b) Valko, M.; Leibfritz, D.; Moncol, J.; Cronin, M. T. D.; Mazur, M.; Telser J.; *Int. J. Biochem. Cell Biol.* **2007**, *39*, 44.
- [70] Dugan, L. L.; Turetsky, D. M.; Du, C.; Lobner, D.; Wheeler, M.; Almlı, C. R.; Shen, C. K. F.; Luh, T. Y.; Choi, D. W.; Lin, T. S. *Proc. Natl. Acad. Sci. U. S. A.* **1997**, *94*, 9434.
- [71] a) Anya, M. Y. L.; Chyi, B. Y.; Wang, S. D.; Yu, H. H.; Kanakamma, P. P.; Luh, T. Y.; Chou, C. K.; Ho, L. T. *J. Neurochem.* **1999**, *72*, 1634.

- b) Wang, I. C.; Tai, L. A.; Lee, D. D.; Kanakamma, P. P.; Shen, C. K. F.; Luh, T.-Y.; Cheng, C. H.; Hwang, K. C. *J. Med. Chem.* **1999**, *42*, 4614.
- [72] Yin, J.-J.; Lao, Meng, J.; Fu, P. P.; Zhao, Y.; Xing, G.; Gao, X.; Sun, B.; Wang, P.C.; Chen, C.; Liang, X.-J. *Mol. Pharmacol.* **2008**, *74*, 1132.
- [73] Lai, Y. L.; Murugan, P.; Hwang, K. C. *Life Sci.* **2003**, *72*, 1271.
- [74] Lin, A. M. Y.; Yang, C. H.; Ueng, Y. F.; Luh, T. Y.; Liu, T. Y.; Lay, Y. P.; Ho, L. T. *Neurochem. Int.* **2004**, *44*, 99.
- [75] Lee, H. J.; Park, J.; Yoon, O. J.; Kim, H. W.; Lee, D.Y.; Kim, D. H.; Lee, W. B.; Lee, N.-E.; Bonventre, J. V.; Kim, S. S. *Nat. Nanotechnol.* **2011**, *6*, 121.
- [76] a) Esch, F.; Fabris, S.; Zhou, L.; Montini, T.; Africh, C.; Fornasiero, P.; Comelli, G.; Rosei, R. *Science* **2005**, *309*, 752. b) Fronzi, M.; Soon, A.; Delley, B.; Traversa, E.; Stampfl, C. *J. Chem. Phys.* **2009**, *131*, 104701.
- [77] a) Griendling, K. K.; Sorescu, D.; Ushio-Fukai, M. *Circ. Res.* **2000**, *86*, 494. b) Imlay, J. A. *Annu. Rev. Biochem.* **2008**, *77*, 755. c) Imlay, J. A. *Annu. Rev. Microbiol.* **2003**, *57*, 395. d) Stadtman, T. C. *Ann. N. Y. Acad. Sci.* **2000**, *899*, 399.
- [78] a) Karakoti, A.; Singh, S.; Dowding, J.; Seal, S.; Self, W. *Chem. Soc. Rev.* **2010**, *39*, 4422. b) Fronzi, M.; Piccinin, S.; Delley, B.; Traversa, E.; Stampfl, C. *Phys. Chem. Chem. Phys.* **2009**, *11*, 9188.

- [79] a) Korsvik, C.; Patil, S.; Seal, S.; Self, W. T. *Chem. Commun.* **2007**, 1056. b) Heckert, E. G.; Karakoti, A. S.; Seal, S.; Self, W. T. *Biomaterials* **2008**, *29*, 2705.
- [80] a) Pirmohamed, T.; Dowding, J. M.; Singh, S.; Wasserman, B.; Heckert, E. G.; Karakoti, A. S.; King, J. E. S.; Seal, S.; Self, W. T. *Chem. Commun.* **2010**, *46*, 2736. b) Celardo, I.; Pedersen, J. Z.; Traversa, E.; Ghibelli, L. *Nanoscale* **2011**, *3*, 1411.
- [81] Tsai, Y. Y.; Oca-Cossio, J.; Agering, K.; Simpson, N. E.; Atkinson, M. A.; Wasserfall, C. H.; Constantinidis, I.; Sigmund, W. *Nanomedicine* **2007**, *2*, 325.
- [82] Hirst, S. M.; Karakoti, A. S.; Tyler, R. D.; Sriranganathan, N.; Seal, S.; Reilly, C. M. *Small* **2009**, *5*, 2848.
- [83] Das, M.; Patil, S.; Bhargava, N.; Kang, J. F.; Riedel, L. M.; Seal, S.; Hickman, J. J. *Biomaterials* **2007**, *28*, 1918.
- [84] Niu, J.; Azfer, A.; Rogers, L. M.; Wang, X.; Kolattukudy, P. E. *Cardiovas. Res.* **2007**, *73*, 549.
- [85] Colon, J.; Herrera, L.; Smith, J.; Patil, S.; Komanski, C.; Kupelian, P.; Seal, S.; Jenkins, D. W.; Baker, C. H. *Nanomedicine* **2009**, *5*, 225.
- [86] Colon, J.; Hsieh, N.; Ferguson, A.; Kupelian, P.; Seal, S.; Jenkins, D. W.; Baker, C. H. *Nanomedicine* **2010**, *6*, 698.

[87] Chen, J.; Patil, S.; Seal, S.; McGinnis, J. F. *Nat. Nanotechnol.* **2006**, *1*, 142.

Chapter 2. Mesoporous Silica-coated Hollow Manganese Oxide Nanoparticles as Positive T1 Contrast Agents for Labeling and MRI Tracking of Adipose-Derived Mesenchymal Stem Cells

2.1 Introduction

In recent years, the use of nanoparticles for biomedical imaging has revolutionized the ability to monitor molecular and cellular events in living organisms. Semiconductor nanoparticles (quantum dots) have been applied as fluorescence probes for cell labeling in optical imaging.^[1-3] Gold nanoparticles have been investigated in optical imaging and as biomedical sensors because of their unique optical and electric properties.^[4-5] Magnetic nanoparticles have also been used as contrast enhancement agents for magnetic resonance imaging (MRI), and as biosensors.^[6-12] MRI is currently one of the most powerful and widely used imaging modalities that provides high spatial resolution combined with excellent anatomical details.^[13-15]

In the last decade, superparamagnetic iron oxide nanoparticles (SPIO) have become the preferred technique for MRI cell tracking,^[16-21] and have now entered the clinical arena.^[22,23] SPIO-labeled cells induce much shorter transverse (T_2) relaxation time and thus, produce hypointensities (dark regions) on T_2/T_2^* -weighted MR images, which presumably indicate the location of the transplanted cells. Unfortunately, SPIO-labeled cells cannot be distinguished from other hypointense regions, such as hemorrhage and blood clots, which are common in many lesions. Therefore, alternative tracking methods using “positive” contrast agents have been explored. i.e. gadolinium (Gd)-based complexes that can generate hyperintense regions as a result of their predominant effects on the longitudinal (T_1) relaxation time of water protons in tissue.^[24-30] Unfortunately, gadolinium-based contrast agents are now associated with nephrogenic systemic fibrosis (NSF), which makes them less favorable agents,^[31] in particular when being retained in cells without rapid clearance from the body. A different approach to enhance MRI contrast is to use manganese as a T_1 relaxation agent. Manganese has been mostly used in the form of $MnCl_2$ to study the structure and function of normal or diseased brain.^[32-34] $MnCl_2$ was used for direct labeling of cells *in vitro*.^[35] Mn

has also been chelated and conjugated to proteins to achieve a higher r_1 relaxivity.^[36] Relaxivity (r_1 , for longitudinal relaxation) describes the change in the relaxation rates of the water protons in the presence of a given contrast agent. Contrast agents with high r_1 values enable lower concentrations of the agent, and consequently, result in higher sensitivity.^[25,36] Alternatively, the longitudinal relaxation can be improved by increasing the number of Mn atoms per particle that can exchange with the water protons, as in the case of nanoparticles. Indeed, manganese oxide (MnO) nanoparticles have recently been explored as a new T_1 MR contrast agent that can delineate fine anatomical features in mouse brain,^[37] and to track cells with positive contrast.^[38] However, most of the reported manganese oxide nanoparticles provide weak contrast, and the duration of signal is too short for long-term *in vivo* MR contrast enhancement.^[37-39]

Coating of nanoparticles can significantly improve their stability, biocompatibility, and relaxivity.^[3,16,21,39] Silica has been recognized as a good candidate for a coating material because it is relatively biocompatible and resistant to biodegradation.^[40-44] In particular, mesoporous silica material is an excellent candidate due to its stability in aqueous solution and high labeling efficiency.^[45-53] Furthermore,

mesoporous silica allows easy access for water molecules to the magnetic center, which significantly improves the water proton relaxation.^[54,55] In this study, we report on a novel design of MnO nanoparticles that have a 'hollow' MnO core structure and a coating consisting of mesoporous silica (termed HMnO@mSiO₂). The high surface area-to-volume ratio and water accessibility through the pores allows for an efficient T₁ MR contrast agent. This was demonstrated *in vitro* and *in vivo* after labeling of multipotent adipose-derived mesenchymal stem cells (MSCs) with HMnO@mSiO₂ nanoparticles.

2.2 Experimental Section

2.2.1 Chemicals

Manganese chloride tetrahydrate (98%), 1-octadecene (90%), ammonium hydroxide (29.4%), cyclohexane (99.0%), oleic acid (90%), rhodamine B isothiocyanate (RITC), 3-aminopropyltriethoxysilane (APTES), and Igepal CO-520 were purchased from Aldrich Chemicals. Sodium oleate was purchased from TCI Chemicals. Cetyltrimethylammonium bromide (CTAB) and tetraethylorthosilicate (TEOS) were purchased from Acros Organics. Ammonium hydroxide (28.0~30.0%), ethylacetate (99%), hydrochloric acid (35~37%), n-hexane (99%), ethanol (99%), chloroform (99%), and acetone (99%) were purchased from Samchun Chemicals. 1,2-distearoyl-sn-glycero-3-phosphoethanolamine-N-[methoxy(polyethylene glycol)-2000] (mPEG-2000 PE) were purchased from Avanti Polar Lipids, Inc.

2.2.2 Synthesis of HMnO@mSiO₂ nanoparticles

Mesoporous silica-coated MnO nanoparticles were prepared using the

following procedure. First, uniformly sized 15 nm MnO nanoparticles were synthesized by the thermal decomposition of Mn-oleate complex.^[56] The resulting MnO nanoparticles were stabilized with oleic acid and dispersed in chloroform at a concentration of 10.8 mg Mn/mL, as measured by inductively coupled plasma atomic emission spectroscopy (ICP-AES). A typical mesoporous silica coating onto MnO nanoparticles (MnO@mSiO₂) was performed using a sol-gel reaction of tetraethyl orthosilicate (TEOS) in an aqueous solution containing cetyltrimethylammonium bromide (CTAB) and MnO nanoparticles stabilized with oleic acid. First, 600 μL of MnO nanoparticles in chloroform was poured into 5 mL of 0.05 M aqueous CTAB solution and the resulting solution was stirred for 1h. Forming an oil-in-water microemulsion, the mixture was heated up to 60 °C and maintained at that temperature for 20 min under stirring in order to evaporate the chloroform. The transparent resulting solution of MnO/CTAB was added to a mixture of 25 mL of water and 1.8 mL of 2 M NaOH solution, and the mixture was heated. At approximately 70 °C under stirring, 0.3 mL of TEOS and 1.8 mL of ethylacetate were added to the reaction solution in sequence. The reaction was continued for 12 h at approximately 70 °C. The washing steps for MnO@mSiO₂

nanoparticles with ethanol were performed to remove unreacted species and then the solution was redispersed in 5 mL of ethanol.

For the hollow core structure of mesoporous silica-coated MnO nanoparticles, an etching process was performed. 100 μ L of mild hydrochloric acid solution (4%) (pH \sim 2.4) was added to the dispersion followed by stirring for 1 h at 70 $^{\circ}$ C. Acid-etched MnO@mSiO₂ nanoparticles were then dispersed in 5 mL ethanol. After washing with ethanol two more times, nanoparticles were redispersed in distilled water. After filtration through a 450 nm (pore size) cellulose acetate filter, HMnO@mSiO₂ nanoparticles were finally redispersed in PBS (10 mM phosphate, 138 mM NaCl, pH = 7.4) solution.

2.2.3 Synthesis of PEG-phospholipid-capped MnO nanoparticles (MnO@PEG-phospholipid)

MnO nanoparticles, dispersed in chloroform, were encapsulated with a PEG-phospholipid shell.^[37] Typically, 2 ml of the organic, dispersible MnO nanoparticles in CHCl₃ (5 mg/ml) was mixed with 1 ml of CHCl₃ solution containing 10 mg of 1,2-distearoyl-sn-glycero-3-phosphoethanolamine-N-[methoxy(polyethylene glycol)-2000] at a

ratio of 5:1. After evaporating the solvent, it was incubated at 80 °C in vacuum for 1 h. The addition of 5 ml water resulted in a clear and dark-brown suspension. After filtration, excess mPEG-2000 PE was removed by ultracentrifugation, and the purified PEG-phospholipid capped MnO nanoparticles were dispersed in distilled water.

2.2.4 Synthesis of dense silica-coated MnO nanoparticles (MnO@dSiO₂)

Dense silica-coated MnO nanoparticles were prepared as described previously along with some modifications.^[40] Polyoxyethylene(5) nonylphenyl ether (0.23 g, 0.544 mmol, Igepal CO-520, containing 50 mol% hydrophilic group, Aldrich) was dispersed in a scintillation tube, containing 4.5 mL of cyclohexane, by sonication. Next, 300 µl of MnO nanoparticles, dispersed in cyclohexane (10.8 mg Mn/mL), was added to the scintillation tube. The resulting mixture was vortexed until the mixture became transparent. Next, 50 µl of ammonium hydroxide was added to form a transparent, brown reverse microemulsion. After 1h of stirring at room temperature, 50 µL of tetraethylorthosilicate (TEOS) was added. The reaction was continued for 24 h at room temperature.

The resulting MnO@dSiO₂ particles were precipitated by adding ethanol, and collected by centrifugation. The collected nanoparticles were redispersed in ethanol, and purified by sonication and centrifugation. Washing steps were repeated three more times, and finally, the particles were redispersed in distilled water.

2.2.5 Characterization of HMnO@mSiO₂ nanoparticles

Transmission electron microscopy (TEM) analysis was conducted with a JEOL JEM-2010 transmission electron microscope operating at 200 kV. Samples were prepared by putting a drop of particle dispersions onto a carbon-coated copper grid. X-ray diffraction (XRD) patterns were obtained using a Rigaku D/Max-3C diffractometer, equipped with a rotation anode and a Cu K α radiation source ($\lambda = 0.15418$ nm). The phase identification was performed using JCPDS-ICDD 2000 software (The International Centre for Diffraction Data; ICDD). N₂ absorption isotherms were measured at 77 K using a Micromeritics ASAP 2000 gas adsorption analyzer after the samples were degassed at 293 K at 10 μ torr for 5 hours. Surface area and total pore volume was evaluated using the Brunauer-Emmet-Teller (BET)

model, and the pore size was evaluated using the Barrett-Joyner-Halenda (BJH) model. DLS measurements and zeta potential measurements were obtained using a zeta-potential and particle size analyzer (ELS-Z2, Otsuka). An inductively coupled plasma atomic emission spectrometer (ICP-AES, Shimadzu ICPS-1000IV-JAPAN) and an inductively coupled plasma mass spectrometer (ICP-MS, ELAN 6100, Perkin-Elmer SCIEX) were used for the quantitative analysis.

2.2.6 Relaxivity measurements

MRI of phantoms was performed using an 11.7 T Bruker Avance system equipped with a 15 mm birdcage RF coil. T_1 and T_2 relaxation times were measured using a modified multi-echo spin echo (MSME) protocol.^[38] Typical settings for T_1 measurements were as follows: 64×64 matrix size; echo time (TE) = 6.4 ms; and a repetition time (TR) series of 0.2, 0.4, 0.8, 1, 1.5, 3, 4, 6 and 10 s; and 2 averages per measurement. For T_2 measurements, the parameters were 128×128 matrix; 3000 ms repetition time; echo time series of 6.4, 12.8, 19.2, 25.6, 32.0, 38.4, 44.8, 51.2, 57.6, 64.0, 70.4, and 76.8 ms; and 2

averages per measurement. Data processing was performed using Matlab (Mathworks, Natick, MA).

2.2.7 Cell culture

Inguinal fat pads were isolated from male C57Bl/6J mice, washed in PBS, and blood vessels were dissected out. The fat was then minced and digested with 0.1% collagenase A (Roche) in HBSS++ (Gibco) for 30 mins in a 35 mm dish at 37 °C and 5% CO₂ humidity. The cell suspension was then neutralized with MSC growth media, i.e., Dulbecco's Modified Eagle's Medium (DMEM, Invitrogen), supplemented with 20% fetal bovine serum (FBS, Gibco) and penicillin/streptomycin (100 U/mL and 100 µg/mL, respectively, Gibco), and centrifuged at 1200 rpm for 10 mins. The top layer of lysed, mature adipocytes, along with the supernatant, was decanted. The pellet, or the stromal vascular fraction, was resuspended in growth media and titrated before centrifuging at 1200 rpm for 5 mins. The pellet was then resuspended with fresh MSC growth media and plated in a 35 mm dish until 100% confluence. MSCs were then passaged and expanded.

2.2.8 Cell labeling and phantom preparation

Electroporation was used to label cells with HMnO@mSiO₂ nanoparticles. Mouse MSCs were cultured in 80 cm² flasks overnight to 80-90% confluence. On the next day, cells were suspended using trypsin-ethylene diamine tetraacetic acid (EDTA), washed with phosphate buffered saline (PBS), and counted. Cells were resuspended and transferred to sterile 0.4 cm gap electroporation cuvettes (Gene Pulser; Bio-Rad). Each cuvette contained 2×10^6 cells suspended in 580 μ l. Nanoparticles dispersed in PBS were added to the cuvette with a final volume of 700 μ l. Cuvettes were kept on ice for one min, and cells were electroporated using a BTX electroporation system (ECM830; Harvard Apparatus). The following electroporation conditions were used: pulse strength = 100 V; N pulses = 5; pulse duration = 5 ms; and pulse interval = 100 ms. After 30 s, cells were transferred to ice for two min, suspended in culture medium, transferred to six-well plates. At 24 h following electroporation, cells were washed twice with PBS, harvested using trypsin-ethylene diamine tetraacetic acid (EDTA), and counted. For gelatin phantoms, 2×10^6 cells suspended in 50 μ l of PBS were transferred to 0.5 mL

polypropylene tubes and mixed with 50 μl of 10% gelatin in PBS. The final cell concentration was 2×10^4 cells/ μl in 5% gelatin.

2.2.9 Cellular imaging *in vitro*

A solution of 2×10^6 MSCs suspended in 580 μl PBS was mixed with 120 μl HMnO@mSiO₂ (or PBS as a control) and electroporated or incubated. MRI scans of *in vitro* phantoms were obtained using a Bruker 9.4 T MRI scanner. T₁ relaxation was measured using an MSME pulse sequence (for T₁; TE = 9 ms, and TR = 0.2, 0.3, 0.5, 0.8, 1, 1.5, 2, 4, 6 and 10 s). Data processing was performed using Matlab (Mathworks, Natick, MA).

2.2.10 Measurement of intracellular manganese content

After *in vitro* gelatin phantom imaging, samples were assayed for manganese content using inductively coupled plasma mass spectroscopy (ICP-MS) analysis (ELAN 6100; Perkin-Elmer SCIEX). The cellular manganese concentration was calculated by dividing the total manganese content by the number of cells.

2.2.11 Cell viability assay.

To examine cell viability, an MTS (3-(4,5-dimethylthiazol-2-yl)-5-(3-carboxymethoxyphenyl)-2-(4-sulfophenyl)-2H-tetrazolium) assay (Cell Titer 96[®] Aqueous, G3582; Promega) was used. After labeling by electroporation or incubation, labeled MSCs were initially seeded in triplicate on 96-well plates at a density of 5×10^3 cells/well, and incubated in growth medium. After 24 h, cells were assayed for viability. To this end, Cell Titer 96[®] Aqueous One Solution reagent was added to each well. Cells were incubated for 2 h at 37 °C in a humidified 5% CO₂ atmosphere. The absorbance at 490 nm was measured using a 96-well plate reader (Beckman Coulter).

2.2.12 *In vitro* cell differentiation studies

Adipocyte differentiation was induced with an adipogenic differentiation kit (R&D System). HMnO@mSiO₂-labeled MSCs were washed with PBS, trypsinized, and plated at 2×10^4 cells/cm₂ in multiple wells of a 24-well plate in StemX Vivo adipogenic base medium (CCM007) or in regular growth medium as negative

differentiation control. When cells in regular growth medium reached 100% confluence, they were fixed with 4% paraformaldehyde, stained with 0.5% Oil Red O (Sigma) in isopropanol. When cells in adipogenic base medium reached 100% confluence, the medium was gently aspirated and fresh adipogenic base medium with 1:100 adipogenic supplement (CCM011) was added to the wells. This complete adipogenic differentiation medium was changed every 3–4 days for 2.5 weeks. Cells were then fixed with 4% paraformaldehyde and stained with 0.5% Oil Red O (Sigma) in isopropanol. MSCs not labeled with HMnO@mSiO₂ underwent the same differentiation protocol, were stained, and served as positive differentiation control. Images were taken at 20X on phase light settings with an inverted light source microscope.

To induce osteocytic differentiation, an osteocytic differentiation kit was used (R&D Systems). HMnO@mSiO₂-labeled MSCs were washed with PBS, trypsinized, and plated at 4×10^3 cells/300 μ l/well in multiple wells of a 24-well plate in StemX Vivo osteogenic base medium (CCM007) or regular growth medium (undifferentiated negative control). When cells in the regular growth medium reached 50-70% confluence, they were fixed in 4% paraformaldehyde, and

stained with Alizarin red in distilled water at pH = 4.1–4.3. When the cells in the osteogenic base medium reached 50–70% confluency, the culture media was replaced with fresh osteogenic base medium containing StemXVivo Osteogenic Supplement (CCM008). This was changed every 3–4 days for 2.5 weeks. Cells were then fixed with 4% paraformaldehyde and stained with Alizarin red in distilled water at pH = 4.1–4.3. MSCs not labeled with HMnO@mSiO₂ underwent the same differentiation protocol, were stained, and served as positive differentiation control. Images were taken at 20X on phase light settings with an inverted light source microscope.

2.2.13 Cellular imaging *in vivo*.

Animal experiments were performed in accordance with a protocol approved by Animal Care and Use Committee of the Johns Hopkins University School of Medicine. C15/BL6 male mice (weighing 20 g) were anesthetized with ketamine/xylazine (100/15 mg per kg), and positioned in a stereotaxic device (Stoelting, Wood Dale, IL, USA). A small skin incision was made in the midline to expose the skull. Using a motorized nanoinjector (Stoelting, Inc.) and 10 μ L Hamilton syringe

(Hamilton, Reno, NV) with an attached 33G needle, 1.0×10^5 labeled or unlabeled MSCs were injected into the putamen of mice ($n = 2$), according to the following coordinates from bregma: anteroposterior [AP] = 1.5 mm; mediolateral [ML] = 1.34 mm; and dorsoventral [DV] = -3.5 mm. Cells were injected slowly over 4 min, and the needle was left in place for 1 min before being withdrawn. The incision was closed with surgical glue, and postoperative analgesia was provided with Ketofen (2 mg/kg) for 72 h.

Serial *in vivo* MRI scans were performed on a Bruker 9.4 T horizontal bore magnet, equipped with a 30-mm Sawtooth resonator (Bruker), and using an MSME pulse sequence. For T_1 measurements, the following parameters were used: TE = 10.5 ms; TR = 1.5 s; FOV = 2.1×2.1 cm; and matrix size = 256×96 .

2.3 Results and Discussion

2.3.1 Synthesis and characterization of HMnO@mSiO₂ particles

Scheme 2.1 describes the synthesis of HMnO@mSiO₂ nanoparticles and labeling of MSCs using electroporation. Manganese oxide nanoparticles with a mean diameter of 15 nm, stabilized with oleic acid, were synthesized by the thermal decomposition of manganese oleate complex.^[56] Then, mesoporous silica shells were coated with a silica sol-gel reaction of tetraethyl orthosilicate (TEOS) in aqueous solution containing cetyltrimethylammonium bromide (CTAB) and MnO nanoparticles under basic conditions.^[49] Hydrophobic MnO nanoparticles capped with oleic acid were transferred to aqueous solution using CTAB, and the subsequent formation of a mesoporous silica shell was achieved. CTAB molecules were used not only as the stabilizing agent to transfer hydrophobic nanoparticles to the aqueous phase, but also as the organic structure-directing template to establish mesopores on the silica shell. The creation of the hollow interior of the MnO cores, along with template removal, was achieved by acid etching and refluxing in ethanol solutions (pH = 2.4). TEM revealed discrete

and uniformly sized HMnO@mSiO₂ nanoparticles. The average diameter of the particles was about 65 nm and the MnO core size was 15 nm. The nanoparticles were all well-dispersed and separated from one another. The mesoporous silica shell and hollow MnO core structures can be clearly seen on the TEM (Figure 2.1a) and HRTEM (Figure 2.1b) images. We also confirmed the mesoporous structures of HMnO@mSiO₂ nanoparticles using N₂ adsorption/desorption isotherms. The average pore diameter calculated using the Barrett-Joiner-Halenda (BJH) method was 3.3 nm. The Brunauer-Emmett-Teller (BET) surface area and pore volume of the HMnO@mSiO₂ nanoparticles were measured to be 181.3 m²g⁻¹ and 0.38 cm³g⁻¹ (Figure 2.2), respectively. These BET results indicate that HMnO@mSiO₂ nanoparticles are highly porous and have large surface areas, which enables rapid access for water molecules to the manganese core through the nanopores of the particles. In addition, the hollow interior of the MnO cores also enables more Mn ions to be exposed to water molecules at the inner surface.^[57] HMnO@mSiO₂ nanoparticles that have a large surface area at the manganese center resulting from these novel structures can be expected to have high T₁ relaxivities.

The MRI properties of the HMnO@mSiO₂ nanoparticles in water

were characterized using an 11.7 T MR scanner. The paramagnetic nanoparticles shortened the T_1 of water protons significantly (Figure 2.1c). The molar relaxivity (effectiveness as contrast agent) was obtained by measuring the relaxation rate with increasing concentrations of nanoparticles (Figure 2.1c), and was calculated to be $0.99 \text{ mM}^{-1}\text{s}^{-1}$ (Figure 2.1d). These relaxivities are significantly higher as compared to that measured for MnO nanoparticles encapsulated with PEG-phospholipids (MnO@PEG-phospholipid),^[37,38] dense silica-coated MnO nanoparticles (MnO@dSiO₂)^[39] (Fig 2.3), and non-etched mesoporous silica-coated MnO nanoparticles (MnO@mSiO₂). Summarized in Table 1, the r_1 values of HMnO@mSiO₂ nanoparticles were 12.4, 9.0, and 1.5 times higher than those of the MnO@dSiO₂, MnO@PEG-phospholipid, and MnO@mSiO₂ particles, respectively. These findings suggest that the majority of the improvement over other nanoparticles is derived from the coating, consistent with our hypothesis that the mesoporous shell allows better water exchange with the MnO core. Water diffusion across mesoporous silica has been studied previously using Pulsed Field Gradient (PFG) Diffusion NMR.^[58] It was shown that water diffuses anisotropically inside mesoporous silica in comparison to isotropic diffusion in the

surrounding environment, with the fastest diffusion component occurring along the channels in the mesoporous silica. The existence of nanopores allows water diffusion to the manganese core leading to efficient relaxation of water in the vicinity of the nanoparticles. In fact, using PFG NMR and magic angle spinning NMR, similar diffusion properties were shown for larger molecules such as pentane, cyclohexane, n-dodecane, and amino acids such as alanine.^[59] An additional improvement over MnO@mSiO₂ (1.5 fold, see above) may be a result of the acidic etching, which increases the surface area-to-volume ratio, and further increases the exchange of the water with Mn²⁺ ions. This improvement is in agreement with previously reported relaxivities for hollow manganese oxide nanoparticles.^[57] Recent reports on other manganese-based nanoparticles describe wide range of relaxivity (r_1) values.^[39,57,60,61] It is difficult to compare the relaxivities of those nanoparticles since the relaxivity was measured at different field strengths (Table 2.1). When measured at lower field (1.5 T), the HMnO@mSiO₂ particles gave higher r_1 but similar r_2 values ($r_1 = 1.72 \text{ mM}^{-1}\text{S}^{-1}$, $r_2 = 11.30 \text{ mM}^{-1}\text{S}^{-1}$) in comparison to those measured at 11.7 T. As expected, the r_2/r_1 ratio at lower field is lower. The closer this ratio is to 1, the better the nanoparticle will function as “positive”

contrast agent. For example, “Magnevist” (a commercial gadolinium complex) has an optimal r_2/r_1 ratio of 1 ($r_1 = 4.6 \text{ mM}^{-1}\text{S}^{-1}$, $r_2 = 4.5 \text{ mM}^{-1}\text{S}^{-1}$) at 1.5 T,^[62] in comparison to 6.56 for HMnO@mSiO₂ at the same field strength. When compared to manganese compounds^[33,36] such as MnCl₂ and chelated manganese, the HMnO@mSiO₂ particles have lower relaxivity. Nevertheless, the nanoparticles were designed specifically for cell labeling and tracking which is not possible with these compounds, even if the relaxivity had to be compromised.

The X-ray diffraction (XRD) pattern (Fig. 2.4) revealed polycrystalline properties of the HMnO@mSiO₂ nanoparticles, consisting mainly of tetragonal Mn₃O₄ phase and small fraction of a cubic MnO phase. The existence of an amorphous silica shell also contributes to the broad peaks of the patterns. In particular, it was found that the crystallinity of the nanoparticle was decreased after the acid etching. The dissolution of the cubic MnO phase from the core part was also examined. After acid etching, HMnO@mSiO₂ nanoparticles were mainly composed of the tetragonal Mn₃O₄ phase.

HMnO@mSiO₂ nanoparticles are stable in water and PBS solutions for over a month. The hydrodynamic diameter of HMnO@mSiO₂ nanoparticles in PBS solution was measured to be 86 nm using

Dynamic Light Scattering (Fig. 2.5). This demonstrates that nanoparticles are stable in PBS and do not form aggregates, which is desirable for its use as intracellular labeling agent. This good colloidal stability of the HMnO@mSiO₂ nanoparticles results from the negative charge of the silica surface. As shown by zeta potential (ζ) measurements (Fig. 2.6), the surface potential of the HMnO@mSiO₂ nanoparticles was -30.43 (mV) in PBS (10 mM phosphate, 138 mM NaCl, pH = 7.4) solution.



Scheme 2.1. Schematic illustration of the synthesis of HMnO@mSiO₂ nanoparticles and labeling of MSCs.

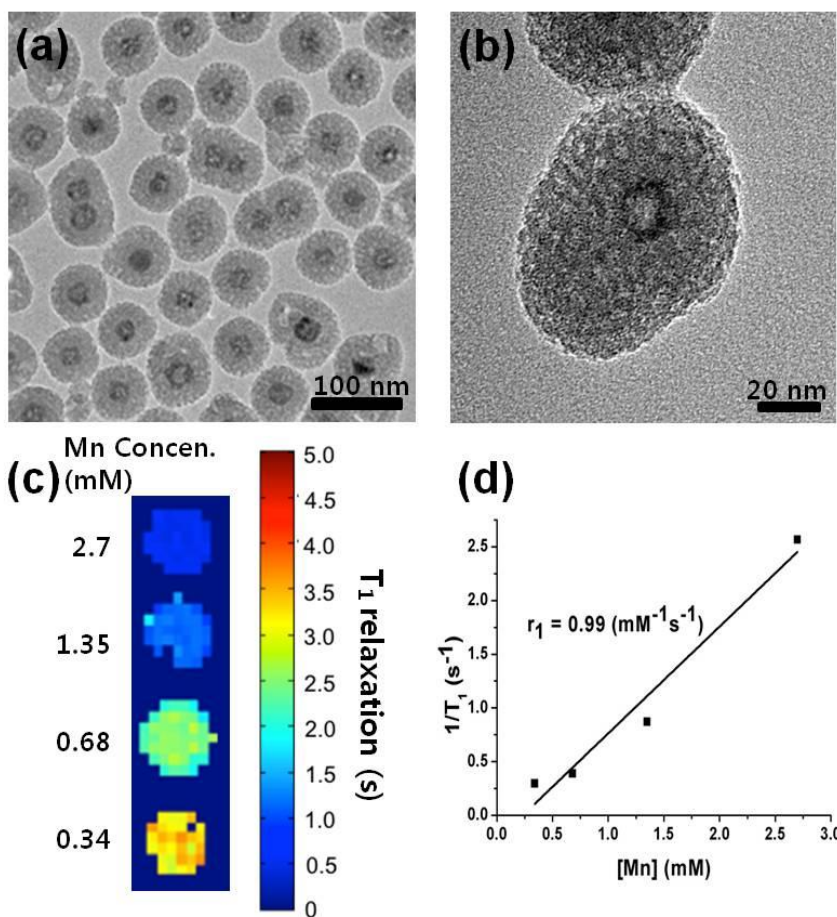


Figure 2.1. Characterization of HMnO@mSiO₂ nanoparticles. (a) TEM image. (b) HRTEM image of a single nanoparticle. (c) T₁ map of HMnO@mSiO₂ nanoparticles suspended in water at 11.7 T. (d) Plot of 1/T₁ versus Mn concentration. The slope indicates the specific relaxivity (r₁).

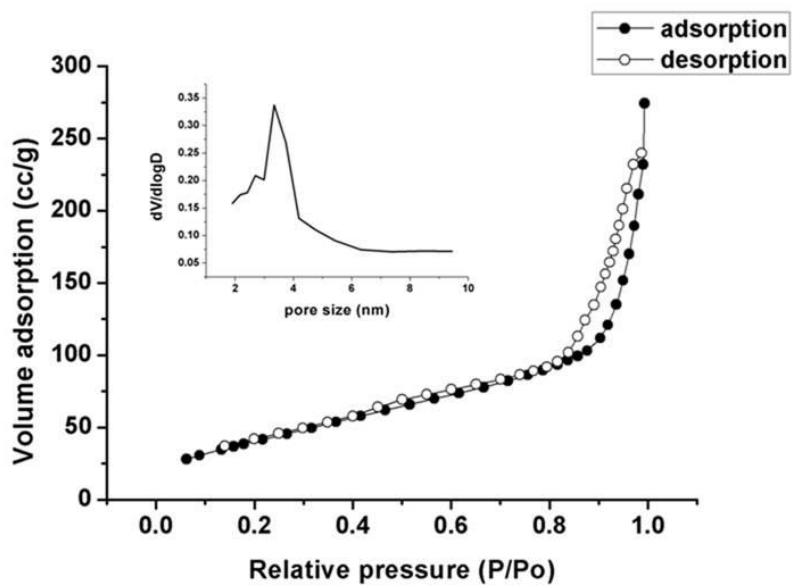


Figure 2.2. N₂ adsorption/desorption isotherms of HMnO@mSiO₂ (inset: pore size distribution; V: pore volume, D: pore size).

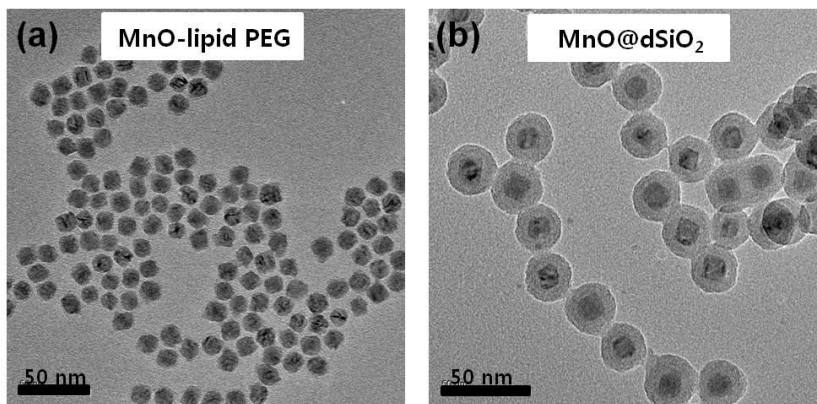


Figure 2.3. TEM images of (a) PEG-phospholipid-capped MnO nanoparticles (MnO@PEG-phospholipid, 15 nm MnO core, 35 nm total particle diameter). (b) dense silica-coated MnO nanoparticles (MnO@dSiO₂, 15 nm MnO core, 35 nm total particle diameter).

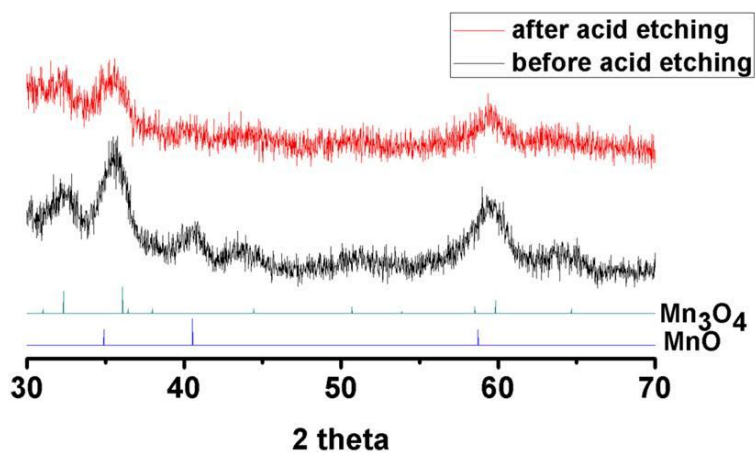


Figure 2.4. XRD pattern for HMnO@mSiO₂ nanoparticles before (a) and after (b) acid etching. XRD patterns for the tetragonal Mn₃O₄ phase (JCPDS Card No. 24-0734) and cubic MnO phase (JCPDS Card No. 07-0230) are shown for reference.

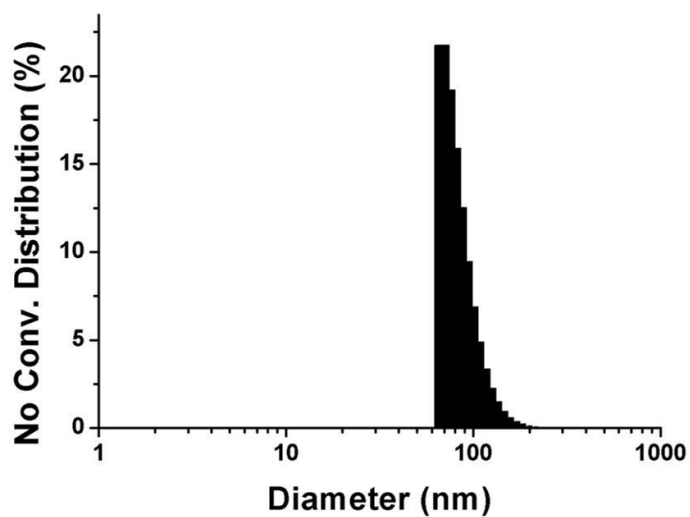


Figure 2.5. Hydrodynamic size distribution of HMnO@mSiO₂ nanoparticles in PBS, as measured by dynamic light scattering (DLS). The average hydrodynamic diameter size was 86 nm.

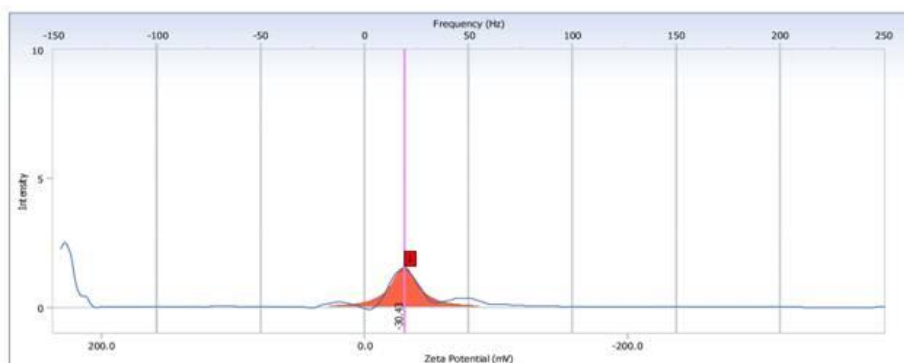


Figure 2.6. Electrophoretic (zeta) potential (ζ) was measured with particle size and a zeta potential analyzer. The zeta potential of HMnO@mSiO₂ nanoparticles in PBS solution was -30.43 (mV).

Table 2.1. Relaxivity date of manganese oxide based nanoparticles (per Mn)

Nanoparticle s¹	r₁ (mM⁻¹s⁻¹)	r₂ (mM⁻¹s⁻¹)	r₂/r₁	Field	Reference
HMnO@mSi	0.99	11.02	11.13	11.7 T	This paper
O₂					
MnO@PEG-phospholipid	0.11	6.16	56	11.7 T	This paper
MnO@mSiO ₂	0.65	9.50	14.61	11.7 T	This paper
MnO@dSiO ₂	0.08	2.27	28.37	11.7 T	This paper
HMnO@mSi	1.72	11.30	6.56	1.5 T	This paper
O₂					
WMON	0.21	1.49	7.09	3 T	57
HMON	1.42	7.74	5.45	3 T	57
Mn-NMOFs	4.0	112.8	28.2	9.4 T	60
Mn ₃ O ₄ @SiO ₂ (RBITC)	0.47	N/A		3.0 T	39
HAS-MNOP	1.97	N/A		7.0 T	61

¹ Nanoparticle annotations: HMnO@mSiO₂—mesoporous silica-coated, hollow MnO nanoparticles. MnO@PEG-phospholipid—MnO nanoparticles encapsulated with PEG-phospholipid. MnO@mSiO₂—non-etched mesoporous silica-coated MnO nanoparticles. MnO@dSiO₂—dense silica-coated MnO nanoparticles. WMON—water-dispersible manganese oxide nanoparticles. HMON—hollow

manganese oxide nanoparticles. Mn-NMOFs—manganese-containing nanoscale metal-organic frameworks (NMOFs). HAS-MNOP—human serum albumin coated manganese oxide nanoparticles.

2.3.2 Cellular uptake and *in vitro* MRI

In order to assess the feasibility of HMnO@mSiO₂ nanoparticles for cell labeling, we initially evaluated the cellular uptake *in vitro*. In this study, we have chosen to use multipotent mesenchymal stem cells (MSCs), which possess the ability to migrate to sites of tissue injury, have many possible therapeutic applications, including the replacement of damaged tissue and the treatment of cancer.^[63-65] Successful clinical translation for the application of MSCs requires an imaging modality that non-invasively permits their visualization and localization in a living organism. Mouse adipose-derived MSCs were labeled using either electroporation or a simple incubation approach. Electroporation uses an electrical pulse to induce a change in the electrochemical permeability of the cell membrane and enables efficient intracytoplasmic labeling of cells.^[66] This approach is commonly used for transferring DNA and chemotherapeutic drugs into cells, and was recently applied to cell labeling with superparamagnetic iron oxide nanoparticles (SPIO)^[67] and manganese oxide.^[38] We hypothesized that electroporation could also be efficiently used for cell labeling with HMnO@mSiO₂ nanoparticles. Since the cell membrane is negatively

charged,^[68] the negative charge of the nanoparticle would result in repulsion of the nanoparticles by the cell membrane, and thus, uptake would be hampered. However, with electroporation, negatively charged HMnO@mSiO₂ nanoparticles can be effectively introduced into cells without using other transfection agents, such as cationic, positively charged molecules.^[69]

Figure 2.7a shows a T₁-weighted MR image of tubes containing MSCs electroporated with different concentrations of HMnO@mSiO₂ nanoparticles suspended in 5% gelatin. The higher the nanoparticle concentration used for labeling, the brighter the tube appeared on the image. Figure 2.7b demonstrates that electroporation with nanoparticles shortens T₁ much more efficiently than direct incubation of the cells with nanoparticles. Figure 2.7c shows the linear correlation between the relaxation rate ($R_1 = 1/T_1$) and the concentration of nanoparticles that was used to label the cells, both by electroporation ($R^2 = 0.994$) and by incubation ($R^2 = 0.989$). At higher nanoparticle concentration, the electroporation is much more efficient than incubation. For these samples the manganese ion content was measured using ICP measurement. The Mn concentration was 9.0 μg Mn/mL (= 0.35 pg Mn/cell) and 1.8 μg Mn/mL (= 0.09 pg Mn/cell) for phantom of MSCs

labeled with electroporation and incubation, respectively. These findings indicate that 26.23% and 5.24% of the added nanoparticles were taken up by MSCs using electroporation and incubation, respectively. Next, both cellular labeling using electroporation and simple incubation were investigated using nanoparticles conjugated with RITC (Figure 2.8). This fluorescent organic dye could be easily conjugated to the silica surface using simple silane conjugation chemistry, as previously reported.^[42,49,70,71] For the same nanoparticle concentration, MSCs labeled with electroporation (Figure 2.8a) showed a higher uptake of nanoparticles than MSCs labeled with incubation (Figure 2.8b). There was also a clear concentration-dependent cellular uptake of the nanoparticles. As was previously shown, compounds that were introduced into the cells via incubation are more likely to accumulate in endosomes, while with electroporation the compounds are freely distributed within the cytoplasm. This may also explain in part the lower relaxivity observed for cells incubated with the particles in comparison to electroporation, since with incubation the particles are in confined region (endosome) and have restricted exchange with water in contrast to electroporated nanoparticles.^[72]

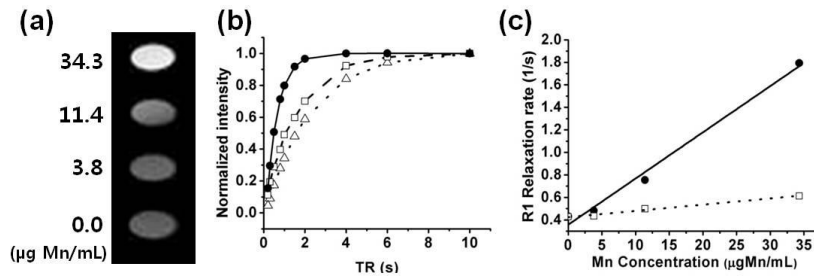


Figure 2.7. (a) T_1 -weighted MR image of adipose derived MSC suspended in 5% gelatin. The cells in each tube were electroporated with HMnO@mSiO₂ nanoparticles (0-34.3 µg Mn/ml). (b) Normalized MRI signal intensity of cells electroporated with 34.3 µg Mn/ml (●), incubated with 34.3 µg Mn/ml (□), or electroporated without nanoparticles (△). (c) The R_1 relaxation rate plotted as a function of the nanoparticle concentration used for labeling the cells (electroporation (●), incubation (□)).

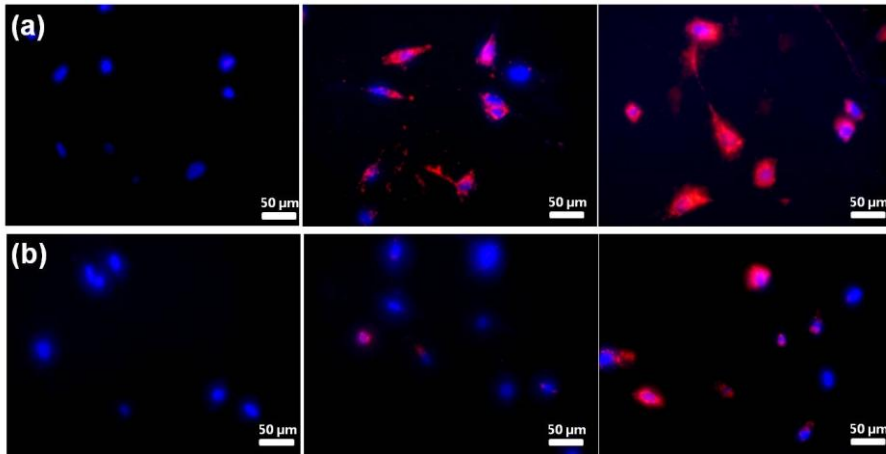


Figure 2.8. Fluorescence microscopy images of RITC-HMnO@mSiO₂-labeled MSCs, counterstained with Hoechst 33342. Using (a) electroporation or (b) simple incubation with 0, 11.4, and 34.3 μg Mn/ml (left to right). Cellular uptake of nanoparticles was dose-dependent. Higher nanoparticle uptake was observed in electroporated MSCs.

2.3.3 Cell viability and differentiation of labeled MSCs

To evaluate the possible cytotoxic effects of the HMnO@mSiO₂ nanoparticles on MSCs, cell viability was assessed with the MTS (3-(4,5-dimethylthiazol-2-yl)-5-(3-carboxymethoxyphenyl)-2-(4-sulfophenyl)-2H-tetrazolium) assay. As shown in Fig 2.9, high cell viability (more than 75%) was still attained at 24 h after electroporation with HMnO@mSiO₂ nanoparticles at a concentration of 68.6 µg Mn/mL. The effect of electroporation with HMnO@mSiO₂ nanoparticles on the differentiation of adipose-derived MSCs was also studied. It was found that MSCs retained the ability to differentiate into adipocytes; however, differentiation into an osteogenic phenotype could not be induced (Figure 2.10). These findings, taken together, indicate that HMnO@mSiO₂ nanoparticles by electroporation have a minimal impact on cell viability, but its effect on cell differentiation should be carefully evaluated for each specific application. In this respect, it is important to note that while SPIOs were reported to inhibit chondrogenesis^[73] SPIO-cell tracking clinical studies have nevertheless been initiated.^[22]

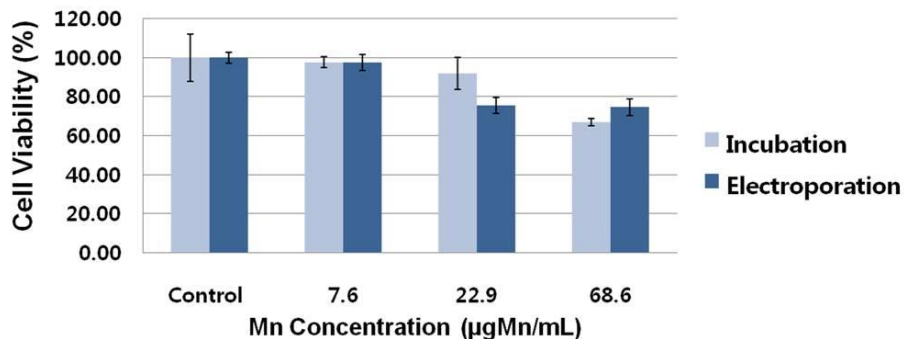


Figure 2.9. Assessment of MSC viability at 24 h after electroporation or simple incubation with HMnO@mSiO₂ nanoparticles. Cell viability was examined using an MTS (3-(4,5-dimethylthiazol-2-yl)-5-(3-carboxymethoxyphenyl)-2-(4-sulfophenyl)-2H-tetrazolium) assay.

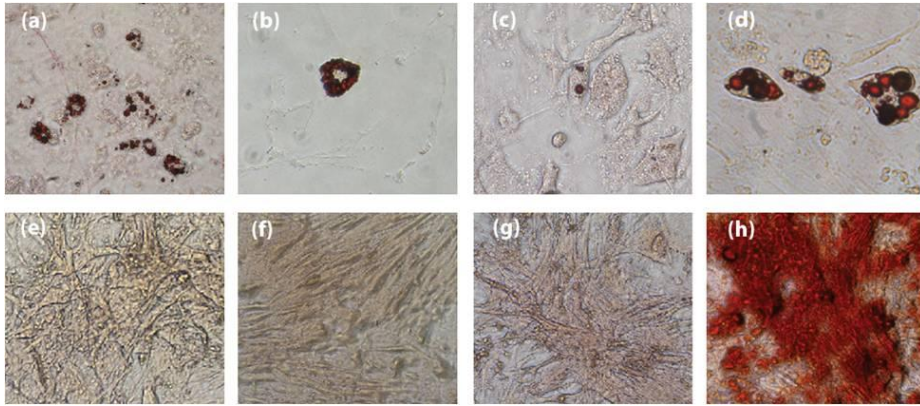


Figure 2.10. Differentiation of HMnO@mSiO₂-labeled MSCs into adipogenic (a-d) or osteogenic (e-h) phenotype. The following labeling conditions were used: (a and e) MSCs electroporated with HMnO@mSiO₂; (b and f) MSCs electroporated without HMnO@mSiO₂; (c and g) MSCs labeled with HMnO@mSiO₂ but not electroporated; and (d and h) MSCs without electroporation or HMnO@mSiO₂.

2.3.4 *In vivo* MR imaging

In order to study the feasibility of HMnO@mSiO₂ nanoparticles for long-term *in vivo* cell tracking, the fate of transplanted, labeled MSCs was serially monitored with MRI. In mice transplanted with unlabeled MSCs, no hyperintensity could be detected (red arrow, Figure 2.11a). However, in mice transplanted with HMnO@mSiO₂-labeled MSCs, a hyperintense region was observed at the transplantation site (green arrows, Figure 2.11b). Serial imaging over 14 days demonstrated that the nanoparticles were stable enough to produce sustained contrast *in vivo*, and therefore, are suitable for monitoring non-invasively the fate of transplanted cells.

The current HMnO@mSiO₂ nanoparticles can be further applied to MRI contrast agents for detecting tumors when conjugated with antibodies^[37] or RGD peptides^[60] that can be targeted directly to cancer cells or to the tumor vasculature, respectively. Furthermore, stem cells labeled with the HMnO@mSiO₂ nanoparticles can assist in detecting tumors because stem cells tend to migrate into tumor sites.^[74,75] And most importantly, such stem cells can be engineered to perform an anti-tumor activity.

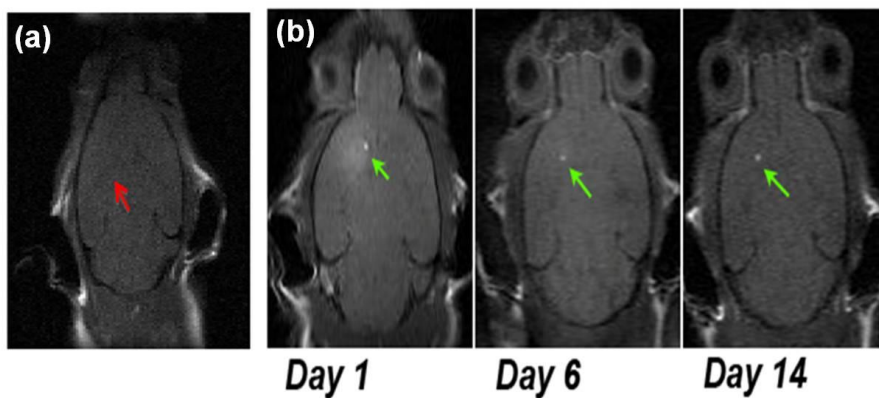


Figure 2.11. *In vivo* MRI of transplanted MSCs. (a) No hyperintense signal (red arrow) was detected in mice transplanted with unlabeled MSCs. (b) Hyperintense signals (green arrows) were detected in mice transplanted with HMnO@mSiO₂-labeled MSCs and was still visible 14 days after injection.

2.4 Conclusion

In summary, we have synthesized and characterized mesoporous silica-coated hollow manganese oxide nanoparticles. These HMnO@mSiO₂ nanoparticles showed a significantly higher r_1 relaxivity over other existing manganese oxide nanoparticle-based contrast agents. The porous coating, which enables water exchange across the shell, combined with the large surface area-to-volume ratio resulting from the novel structure, increases water accessibility to the manganese core, and consequently, provides enhanced T₁ contrast. These nanoparticles showed high cellular uptake by adipose derived MSCs, using electroporation, and were detected with MRI both *in vitro* and intracranially *in vivo* over a prolonged time period. In light of these findings, HMnO@mSiO₂ nanoparticles have a great potential for MRI cell tracking using positive contrast.

2.5 References

- [1] Dubertret, B.; Skourides, P.; Norris, D. J.; Noireaux, V.; Brivanlou, A. H.; Libchaber, A. *Science* **2002**, *298*, 1759.
- [2] Kim, S.; Lim, Y. T.; Soltesz, E. G.; De Grand, A. M.; Lee, J.; Nakayama, A.; Parker, J. A.; Mihaljevic, T.; Laurence, R. G.; Dor, D. M.; Cohn, L. H.; Bawendi, M. G.; Frangioni, J. V. *Nat. Biotechnol.* **2004**, *22*, 93.
- [3] Medintz, I. L.; Uyeda, H. T.; Goldman, E. R.; Mattoussi, H. *Nat. Mater.* **2005**, *4*, 435.
- [4] Nam, J.-M.; Thaxton, C. S.; Mirkin, C. A. *Science* **2003**, *301*, 1884.
- [5] Rosi, N. L.; Mirkin, C. A. *Chem. Rev.* **2005**, *105*, 1547.
- [6] Gao, J.; Gu, H.; Xu, B. *Acc. Chem. Res.* **2009**, *42*, 1097.
- [7] Jun, Y.-W.; Lee, J.-H.; Cheon, J. *Angew. Chem. Int. Ed.* **2008**, *47*, 5122.
- [8] Gao, J.; Xu, B. *Nano Today* **2009**, *4*, 37.
- [9] Gao, J.; Liang, C.; Cheung, J. S.; Pan, Y.; Kuang, Y.; Zhao, F.; Zhang, B.; Zhang, X.; Wu, E. X.; Xu, B. *J. Am. Chem. Soc.* **2008**, *130*, 11828.
- [10] Xie, J.; Chen, K.; Lee, H.-Y.; Xu, C.; Hsu, A. R.; Peng, S.; Chen, X.; Sun, S. *J. Am. Chem. Soc.* **2008**, *130*, 7542.
- [11] Xu, C.; Xie, J.; Ho, D.; Wang, C.; Kohler, N.; Walsh, E. G.; Morgan, J. R.; Chin, Y. E.; Sun, S. *Angew. Chem. Int. Ed.* **2008**, *47*, 173.

- [12] Na, H. B.; Song, I. C.; Hyeon, T. *Adv. Mater.* **2009**, *21*, 2133.
- [13] Massoud, T. F.; Gambhir, S. S. *Gene Dev.* **2003**, *17*, 545.
- [14] Weissleder, R.; Mahmood, U. *Radiology* **2001**, *219*, 316.
- [15] Weissleder, R.; Pittet, M. J. *Nature* **2008**, *452*, 580.
- [16] Bulte, J. W. M.; Douglas, T.; Witwer, B.; Zhang, S.-C.; Strable, E.; Lewis, B. K.; Zywicke, H.; Miller, B.; van Gelderen, P.; Moskowitz, B. M.; Duncan, I. D.; Frank, J. A. *Nat. Biotechnol.* **2001**, *19*, 1141.
- [17] Bulte, J. W. M.; Zhang, S.-C.; van Gelderen, P.; Heryneki, V.; Jordan, E. K.; Duncan, I. D.; Frank, J. A. *Proc. Natl. Acad. Sci. USA* **1999**, *96*, 15256.
- [18] Jun, Y.-W.; Huh, Y.-M.; Choi, J.-S.; Lee, J.-H.; Song, H.-T.; Kim, S.; Yoon, S.; Kim, K.-S.; Shin, J.-S.; Suh, J.-S.; Cheon, J. *J. Am. Chem. Soc.* **2005**, *127*, 5732.
- [19] Heyn, C.; Ronald, J. A.; Ramadan, S. S.; Snir, J. A.; Barry, A. M.; MacKenzie, L. T.; Mikulis, D. J.; Palmieri, D.; Bronder, J. L.; Steeg, P. S.; Yoneda, T.; MacDonald, I. C.; Chambers, A. F.; Rutt, B. K.; Foster, P. *J. Magn. Reson. Med.* **2006**, *56*, 1010.
- [20] Kraitchman, D. L.; Heldman, A. W.; Atalar, E.; Amado, L. C.; Martin, B. J.; Pittenger, M. F.; Hare, J. M.; Bulte, J. W. M. *Circulation* **2003**, *107*, 2290.

- [21] Lewin, M.; Carlesso, N.; Tung, C.-H.; Tang, X.-W.; Cory, D.; Scadden, D. T.; Weissleder, R. *Nat. Biotechnol.* **2000**, *18*, 410.
- [22] Bulte, J. W. M. *Am. J. Roentgenol.* **2009**, *193*, 314.
- [23] de Vries, I. J.; Lesterhuis, W. J.; Barentsz, J. O.; Verdijk, P.; Krieken, J. H.; Boerman, O. C.; Oyen, W. J. G.; Bonenkamp, J. J.; Boezeman, J. B.; Adema, G. J.; Bulte, J. W. M.; Scheenen, T. W. J.; Punt, C. J. A.; Heerschap, A.; Figdor, C. G. *Nat. Biotechnol.* **2005**, *23*, 1407.
- [24] Aime, S.; Castelli, D. D.; Lawson, D.; Terreno, E. *J. Am. Chem. Soc.* **2007**, *129*, 2430.
- [25] Caravan, P. *Chem. Soc. Rev.* **2006**, *35*, 512.
- [26] Caravan, P.; Das, B.; Dumas, S.; Epstein, F. H.; Helm, P. A.; Jacques, V.; Koerner, S.; Kolodziej, A.; Shen, L.; Sun, W.-C.; Zhang, Z. *Angew. Chem. Int. Ed.* **2007**, *46*, 8171.
- [27] Flacke, S.; Fischer, S.; Scott, M. J.; Fuhrhop, R. J.; Allen, J. S.; McLean, M.; Winter, P.; Sicard, G. A.; Gaffney, P. J.; Wickline, S. A.; Lanza, G. *M. Circulation* **2001**, *104*, 1280.
- [28] Modo, M.; Cash, D.; Mellodew, K.; Williams, S. C. R.; Fraser, S. E.; Meade, T. J.; Price, J.; Hodges, H. *NeuroImage* **2002**, *17*, 803.
- [29] Granot, D.; Addadi, Y.; Kalchenko, V.; Harmelin, A.; Kunz-Schughart L. A.; Neeman M. *Cancer Res.* **2007**, *67*, 9180.

- [30] Anderson, S. A.; Lee, K. K.; Frank, J. A. *Invest. Radiol.* **2006**, *41*, 332.
- [31] Perez-Rodriguez, J.; Lai, S.; Ehst, B. D.; Fine, D. M.; Bluemke, D. A. *Radiology* **2009**, *250*, 371.
- [32] Pelled, G.; Bergman, H.; Ben-Hur, T.; Goelman, G. *J. Magn. Reson. Imaging* **2007**, *26*, 863.
- [33] Silva, A. C.; Lee, J. H.; Aoki, I.; Koretsky, A. P. *NMR Biomed.* **2004**, *17*, 532.
- [34] Yu, X.; Wadghiri, Y. Z.; Sanes, D. H.; Turnbull, D. H. *Nat. Neurosci.* **2005**, *8*, 961.
- [35] Aoki, I.; Takahashi Y.; Chuang, K.-H.; Silva, A. C.; Igarashi, T.; Tanaka, C.; Childs, R. W.; Koretsky, A. P. *NMR Biomed.* **2006**, *19*, 50.
- [36] Troughton, J. S.; Greenfield, M. T.; Greenwood, J. M.; Dumas, S.; Wiethoff, A. J.; Wang, J.; Spiller, M.; McMurry, T. J.; Caravan, P. *Inorg. Chem.* **2004**, *43*, 6313.
- [37] Na, H. B.; Lee, J. H.; An, K.; Park, Y.; Park, M.; Lee, I. S.; Nam, D.-H.; Kim, S. T.; Kim, S.-H.; Kim, S.-W.; Lim, K.-H.; Kim, K.-S.; Kim, S.-O.; Hyeon, T. *Angew. Chem. Int. Ed.* **2007**, *46*, 5397.
- [38] Gilad, A. A.; Walczak, P.; McMahon, M. T.; Na, H. B.; Lee, J. H.; An, K.; Hyeon, T.; van Zijl, P. C. M.; Bulte, J. W. M. *Magn. Reson. Med.* **2008**, *60*, 1.

- [39] Yang, H.; Zhuang, Y.; Hu, H.; Du, X.; Zhang, C.; Shi, X.; Wu, H.; Yang, S. *Adv. Funct. Mater.* **2010**, *20*, 1733.
- [40] Yi, D. K.; Selvan, S. T.; Lee, S. S.; Papaefthymiou, G. C.; Kundaliya, D.; Ying, J. Y. *J. Am. Chem. Soc.* **2005**, *127*, 4990.
- [41] Selvan, S. T.; Patra, P. K.; Ang, C. Y.; Ying, J. Y. *Angew. Chem. Int. Ed.* **2007**, *46*, 2448.
- [42] Yoon, T. J.; Kim, J. S.; Kim, B. G.; Yu, K. N.; Cho, M.-H.; Lee, J.-K. *Angew. Chem. Int. Ed.* **2005**, *44*, 1068.
- [43] Burns, A. A.; Vider, J.; Ow, H.; Herz, E.; Penate-Medina, O.; Baumgart, M.; Larson, S. M.; Wiesner, U.; Bradbury, M. *Nano Lett.* **2009**, *9*, 442.
- [44] Piao, Y.; Burns, A.; Kim, J.; Wiesner, U.; Hyeon, T. *Adv. Funct. Mat.* **2008**, *18*, 3745.
- [45] Ying, J. Y.; Mehnert, C. P.; Wong, M. S. *Angew. Chem. Int. Ed.* **1999**, *38*, 56.
- [46] Wan, Y.; Zhao, D. *Chem. Rev.* **2007**, *107*, 2821.
- [47] Deng, Y.; Qi, D.; Deng, C.; Zhang, X.; Zhao, D. *J. Am. Chem. Soc.* **2008**, *130*, 28.
- [48] Kim, J.; Lee, J. E.; Lee, J.; Yu, J. H.; Kim, B. C.; An, K.; Hwang, Y.; Shin, C.-H.; Park, J.-G.; Kim, J.; Hyeon, T. *J. Am. Chem. Soc.* **2006**, *128*, 688.

- [49] Kim, J.; Kim, H. S.; Lee, N.; Kim, T.; Kim, H.; Yu, T.; Song, I. C.; Moon, W. K.; Hyeon, T. *Angew. Chem. Int. Ed.* **2008**, *47*, 8438.
- [50] Trewyn, B. G.; Slowing, I. I.; Giri, S.; Chen, H.-T.; Lin, V. S.-Y. *Acc. Chem. Res.* **2007**, *40*, 846.
- [51] Lin, Y.-S.; Wu, S.-H.; Hung, Y.; Chou, Y.-H.; Chang, C.; Lin, M.-L.; Tsai, C.-P.; Mou, C.-Y. *Chem. Mater.* **2006**, *18*, 5170.
- [52] Huang, D.-M.; Hung, Y.; Ko, B.-S.; Hsu, S.-C.; Chen, W.-H.; Chien, C.-L.; Tsai, C.-P.; Kuo, C.-T.; Kang, J.-C.; Yang, C.-S.; Mou, C.-Y.; Chen, Y.-C. *FASEB J.* **2005**, *19*, 2014.
- [53] Liu, H.-M.; Wu, S.-H.; Lu, C.-W.; Yao, M.; Hsiao, J.-K.; Hung, Y.; Lin, Y.-S.; Mou, C.-Y.; Yang, C.-S.; Huang, D.-M.; Chen, Y.-C. *Small* **2008**, *4*, 619.
- [54] Kim, J. S.; Rieter, W. J.; Taylor, K. M. L.; An, H.; Lin, W. *J. Am. Chem. Soc.* **2007**, *129*, 8962.
- [55] Taylor, K. M. L.; Kim, J. S.; Rieter, W. J.; An, H.; Lin, W. *J. Am. Chem. Soc.* **2008**, *130*, 2154.
- [56] Park, J.; An, K.; Hwang, Y.; Park, J.-G.; Noh, H.-J.; Kim, J.-Y.; Park, J.-H.; Hwang, N.-M.; Hyeon, T. *Nat. Mater.* **2004**, *3*, 891.
- [57] Shin, J.; Anisur, R. M.; Ko, M. K.; Im, G. H.; Lee, J. H.; Lee, I. S. *Angew. Chem. Int. Ed.* **2009**, *48*, 321.

- [58] Stallmach, F.; Kalrger J.; Krause, C.; Jeschke, M.; Oberhagemann U. *J. Am. Chem. Soc.* **2000**, *122*, 9237.
- [59] Amitay-Rosen, T.; Kababya, S.; Vega S. *J. Phys. Chem. B* **2009**, *113*, 6267.
- [60] Taylor, K. M. L.; Rieter, W. J.; Lin W. *J. Am. Chem. Soc.* **2008**, *130*, 14358.
- [61] Huang, H.; Xie, J.; Chen, K.; Bu, L.; Lee, S.; Cheng, Z.; Li X.; Chen X. *Chem. Commun.* **2010**, *46*, 6684.
- [62] Seo W. A.; Lee J. H.; Sun, X.; Suzuki, Y.; Mann, D.; Liu, Z.; Terashima, M.; Yang, P. C.; McConnell M. V.; Nishimura, D. G.; Dai, H. *Nat. Mater.* **2006**, *5*, 971.
- [63] Cowan, C. A.; Klimanskaya, I.; McMahan, J.; Atenza, J.; Witmyer, J.; Zucker, J.; Wang, S.; Morton, C. C.; McMahan, A. P.; Powers, D.; Melton, D. A. *N. Engl. J. Med.* **2004**, *350*, 1353.
- [64] Mckay, R. *Nature* **2000**, *406*, 361.
- [65] Pittenger, M. F.; Mackay, A. M.; Beck S. C.; Jaiswal R. K.; Douglas R.; Mosca, J. D.; Moorman, M. A.; Simonetti, D. W.; Craig, S.; Marshak, D. *R. Science* **1999**, *284*, 143.
- [66] Teissie, J.; Eynard, N.; Gabriel, B.; Rols, M. P. *Adv. Drug Deliv. Rev.* **1999**, *35*, 3.

- [67] Walczak, P.; Kedziorek, D. A.; Gilad, A. A.; Lin, S.; Bulte, J. W. M. *Magn. Reson. Med.* **2005**, *54*, 769.
- [68] Zhdanov, R. I.; Podobed, O. V.; Vlassov, V. V. *Bioelectrochemistry* **2002**, *58*, 53.
- [69] Gershon, H.; Ghirlando, R.; Guttman, S. B.; Minsky, A. *Biochemistry* **1993**, *32*, 7143.
- [70] Lee, J. E.; Lee, N.; Kim, H.; Kim, J.; Choi, S. H.; Kim, J. H.; Kim, T.; Song, I. C.; Park, S. P.; Moon, W. K.; Hyeon, T. *J. Am. Chem. Soc.* **2010**, *132*, 552.
- [71] Burns, A.; Ow, H.; Wiesner, U. *Chem. Soc. Rev.* **2006**, *35*, 1028.
- [72] Terreno, E.; Crich, S. G.; Belfiore, S.; Biancone, L.; Cabella, C.; Esposito, G.; Manazza, A. D.; Aime, S. *Magn. Reson. Med.* **2006**, *55*, 419.
- [73] Kostura, L.; Kraitchman, D. L.; Mackay, A. M.; Pittenger, M. F.; Bulte, J. W. M. *NMR Biomed.* **2004**, *17*, 513.
- [74] Arbab, A. S.; Rad, A. M.; Iskander, A.S.M.; Jafari-Khouzani, K.; Brown, S. L.; Churchman, J. L.; Ding, G.; Jiang, Q.; Frank, J. A.; Soltanian-Zadeh, H.; Peck, D. J. *Magn. Reson. Med.* **2007**, *58*, 519.
- [75] Thu, M. S.; Najbauer, J.; Kendall, S. E.; Harutyunyan, I.; Sangalang, N.; Gutova, M.; Metz, M. Z.; Garcia, E.; Frank, R. T.; Kim S. U.; Moats, R. A.; Aboody K. S. *PLoS One* **2009**, *4*, e7218.

Chapter 3. Micro-CT Imaging of Human Mesenchymal Stem Cells Labeled with Gold Nanoparticles

3.1 Introduction

Cell-based therapies have been recently promoted in the field of regenerative medicine.^[1,2] Transplantation of stem cells have shown positive effects on the regeneration of various tissues, such as bone,^[3] cartilage,^[4] and myocardium.^[5] In particular, adult human mesenchymal stem cells (hMSCs) are appropriate to be used in cell-based therapies because they can be relatively easily isolated, rapidly proliferated *in vitro*, and differentiated into various specific lineages.^[6,7]

A reliable means to image the distribution of engrafted stem cells is pertinent to monitor and support stem cell therapy. By tracking the location of the cells, the following can be investigated – the best routes of administration, distribution dynamics of transplanted cells, their

safety, and efficacy, and thus, successfully translated into clinical trials.^[8-10]

Various imaging modalities were used for stem cell imaging to clearly see transplanted cells and evaluate the underlying pathological processes. Each imaging modality has its own characteristics in specificity, sensitivity, resolution, and availability.^[11,12] Among them, X-ray computed tomography (CT) imaging is one of the most widely used imaging tools in the clinic due to its cost effectiveness, high-contrast resolution, and ease of imaging procedure.^[13-15] However, very few studies are performed in cell tracking using CT imaging due to its inherent low sensitivity and limit in soft-tissue image contrast as compared to other imaging modalities such as positron emission tomography (PET) or magnetic resonance imaging (MRI).^[16-18]

The advancements in nanotechnology have allowed development of novel contrast agents that can be successfully utilized in molecular and cell imaging. Recently, bismuth, ytterbium, tantalum based nanoparticles were synthesized and investigated as CT contrast agents.^[19-22] Gold nanoparticles (Au NPs) were also developed as promising CT contrast agents due to its high atomic number, and efficient X-ray attenuation properties.^[23-27] They have higher X-ray absorption

coefficient ($5.16 \text{ cm}^2/\text{g}$) than iodine, the commercial CT contrast agent ($1.94 \text{ cm}^2/\text{g}$) at 100 keV, thus, producing superior contrast.^[28,29] Particularly, gold nanoparticles are very easy to synthesize, and their size can be controlled.^[30] Above all, these nanoparticles are bioinert, and exhibit low cytotoxicity when labeled to cells.^[31-33]

In this study, we developed a method to label human mesenchymal stem cells (hMSCs) with Au NPs to enable their visualization by micro-CT imaging.

3.2 Experimental Section

3.2.1 Chemicals

Au nanoparticles with diameters of 5, 10, 20, and 40 nm were purchased from British Biocell International (Cardiff, UK). Poly-L-lysine hydrobromide and rhodamine B isothiocyanate (RITC) were purchased from Sigma-Aldrich (St. Louis, MO).

3.2.2 Preparation of Au NPs-PLL (RITC) complexes

32 mL of Au nanoparticle solutions (60 $\mu\text{g}/\text{ml}$) from the vendor of BBI were mixed with 1.4 mL of poly-L-lysine (1–5 kD) solution (1mg/ml) and stirred for 30 mins. Poly-L-lysine hydrobromide was dissolved in distilled water prior to use. The nanoparticle solutions were then centrifuged at 3600 rpm for 45 mins in order to remove the excess poly-L-lysine. Then distilled water was added into each conical tube resulting in a total of 1.5 mL of Au NPs-PLL complex solution.

Rhodamine B isothiocyanate (RITC) was added to the complexes to enable fluorescence microscopic imaging. For RITC conjugation to Au

NPs-PLL complexes, 2 mg of RITC were added to tubes and stirred for 12 h, protected from light. After thoroughly washing 3 times with distilled water to remove unreacted RITC, nanoparticle solution was finally dispersed in 1.5 mL of distilled water

3.2.3 Characterization of Au NPs-PLL(RITC) complexes

Transmission electron microscopy (TEM) analysis was conducted with a JEOL JEM-2010 transmission electron microscope operating at 200 kV. Samples were prepared by putting a drop of particle dispersions onto a carbon-coated copper grid. Dynamic light scattering (DLS) measurements and zeta potential measurements were obtained using a zeta-potential and particle size analyzer (ELS-Z2, Otsuka). An inductively coupled plasma atomic emission spectrometer (ICP-AES, Shimadzu ICPS-1000IV-JAPAN) and an inductively coupled plasma mass spectrometer (ICP-MS, ELAN 6100, Perkin-Elmer SCIEX) were used for quantitative analysis.

3.2.4 Hounsfield Unit (HU) measurements

To assess the contrast enhancement, the CT signal intensity was expressed in Hounsfield Units (HU) [Ambrose J, Hounsfield G (1973) Br. J. Radiol. 46:1016–1047]. To make this conversion, a two-point calibration method was used. In this method, the CT signal intensity in the water volume was set to 0 HU, and the CT signal intensity in the air volume was set to -1,000 HU. The HU values of other materials were then obtained by linear extrapolation. The HU values of target objects were then obtained by linear extrapolation.

$$HU = 1000 \times \frac{\mu_x - \mu_{water}}{\mu_{water} - \mu_{air}}$$

Where, μ_x , μ_{water} , μ_{air} are the linear attenuation coefficients of the target object, the water, and the air.

3.2.5 Cell culture

Human MSCs (Lonza, Walkersville, MD) were cultured in Dulbecco's Modified Eagle Medium (DMEM, Invitrogen, Carlsbad, CA) supplemented with 10% fetal bovine serum (FBS), 1% glutamax, and 1% penicillin-streptomycin. The cell culture medium was changed every 2–3 days. When hMSCs were confluent in 150 cm² cell culture

flask, cells were passaged using 0.25% trypsin/ethylenediamine tetraacetic acid (EDTA, Lonza), collected by centrifugation at 1000 rpm for five mins, and counted with Trypan Blue Exclusion Method. Cells were grown at 37 °C in 5% CO₂ incubator and passage 4–7 human hMSCs were used.

3.2.6 Cellular uptake assessment

Cellular uptake was studied using bright field microscopy, fluorescence microscopy, and transmission electron microscopy. Labeled hMSCs with Au NPs-PLL(RITC) complexes were cultured in a six-well plate (Falcon #303046, Non-pyrogenic). After 24 h, cells were washed with PBS, fixed with 4% paraformaldehyde, and stained with 4',6-diamidino-2-phenylindole (DAPI, 1 µg/mL in PBS, Roche). Fluorescence images were acquired using Olympus BX51 and IX71 epifluorescence microscopes equipped with an Olympus DP-70 digital acquisition system.

Transmission microscope images were acquired using JEOL JEM-2010 TEM operating at 200 kV. Labeled hMSCs with Au NPs-PLL complexes were cultured in a six-well plate. After 24 h, cells were

washed with PBS, fixed with 4% paraformaldehyde for 2 h. Subsequently, fixed specimens were treated with 2% osmium tetroxide buffered in 0.1 M cacodylate buffer for 2 h. Specimens were dehydrated with 50 to 100% graded ethanol and propylene oxide (EM Sciences). The samples were then embedded in pure Epoxy Resin at 60 °C for 3 days. Ultrathin sections were cut using glass knives and a diamond knife (Reichert-Jung, Vienna, Austria) on an ultramicrotome (RMC MTXL; Tucson, AZ, USA). Sections were then stained with lead citrate and uranyl acetate (both from EM Sciences), and observed under TEM.

3.2.7 Cell labeling and phantom preparation

Haman MSCs were cultured in 150 cm² cell culture plate to 80% confluence in CO₂ incubator. 1.5 mL of Au NPs-PLL(RITC) complexes solutions in PBS were added to cell culture plates and incubated. On the next day, cells were washed with phosphate buffered saline (PBS) 2-3 times, and suspended using trypsin/EDTA. After incubation for 5 mins in CO₂ incubator, cells were centrifuged down for 5 mins, counted, and collected. For *in vitro* phantom preparations, 1×10^6 cells labeled

with different concentration of Au NPs-PLL(RITC) complexes (0, 0.025, 0.05, 0.1, and 0.2 mgAu/ml) were suspended in 25 μ l of PBS in 0.1 mL PCR tubes and mixed with 25 μ l of 2% agarose in PBS. The final concentration was 2×10^4 cells/ μ l in 1% agarose. Different numbers of labeled cells (1×10^6 , 5×10^5 , 2.5×10^5 , 1.3×10^5 , 6.3×10^4 , and 3.1×10^4 cells) were suspended in 25 μ l of PBS in 0.1 mL PCR tubes and mixed with 25 μ l of 2% agarose in PBS. Gently mixing makes the homogeneous agarose gel solution. The final cell concentration was 2×10^4 , 1×10^4 , 5×10^3 , 2.5×10^3 , 1.3×10^3 , and 6.2×10^2 cells/ μ l in 1% agarose, respectively.

3.2.8 Cell viability assay

The viability and proliferation of labeled hMSCs with Au NPs-PLL(RITC) complexes were evaluated by MTS ([3-(4,5-dimethylthiazol-2-yl)-5-(3-carboxymethoxyphenyl)-2-(4-sulfophenyl)-2H-tetrazolium, inner salt) (Cell Titer 96[®] Aqueous, G3582; Promega) assay and calcein-acetyoxymethyl (AM) enzyme assay (4892-010-K; Trevigen Inc.). Assay was performed in triplicate. HMSCs were seeded in triplicate into 96 well plates at a density of 5.0×10^3 cells per well in

200 μ l of culture medium and grown overnight. The cells were then incubated with various concentrations of Au NPs-PLL(RITC) complexes (0, 0.25, 0.05, 0.1, and 0.2 mg Au/mL). On the next day, cells were washed with PBS and 20 μ l of Cell Titer 96[®] Aqueous One Solution Reagent was added to each well. Cells were incubated for 2 h at 37 °C in a humidified 5% CO₂ atmosphere. The absorbance was recorded at 490 nm using a 96-well micro plate reader (Victor3).

For calcein-acetyoxymethyl (AM) enzyme assay, labeled cells were washed once with 100 μ l of calcein-AM buffer, and then 100 μ l of calcein-AM solution was added. Cells were incubated for 30 min at 37 °C in a humidified 5% CO₂ atmosphere. The fluorescence was recorded using a 490-nm excitation filter and a 520-nm emission filter, with the fluorescence intensity being proportional to the number of viable cells.

3.2.9 *In vitro* cell differentiation studies

Labeled hMSCs with Au NPs-PLL(RITC) complexes were induced to differentiate into the adipogenic and osteogenic lineages. Labeled and unlabeled hMSCs were cultured in a six-well plate. After cells were

confluent, the MSC growth medium was replaced with adipogenic induction medium (DMEM, 10% fetal bovine serum, 1% penicillin-streptomycin, 1% glutamax, 1 μ M dexamethasone, 10 μ g/mL 3-isobutyl-1-methylxanthine, 10 μ g/mL insulin, and 100 μ M indomethacin, Lonza). After three days, the adipogenic induction medium was replaced with adipogenic maintenance medium for one day (DMEM, 10% fetal bovine serum, 1% penicillin-streptomycin, 1% glutamax, and 10 μ g/mL insulin, Lonza). Three cycles of induction and maintenance were performed, after which the cells were incubated in adipogenic maintenance medium for seven days. Control cells were supplemented only with adipogenic maintenance medium. Oil Red O (Sigma-Aldrich) staining was used to assess adipogenesis. The cells were fixed in 10% formalin and then incubated in 60% isopropanol for four mins. The cells were then incubated in Oil Red O staining solution for five mins, rinsed in distilled water, and counterstained in hematoxylin for one min. After washing with distilled water, the slides were mounted and viewed under brightfield microscope using Olympus BX51 and IX71 epifluorescence microscopes equipped with an Olympus DP-70 digital acquisition system.

Osteogenesis was initiated when hMSCs were confluent. The medium

were replaced with osteogenic induction medium (DMEM, 10% fetal bovine serum, 1% penicillin-streptomycin, 1% glutamax, 50 µg/mL ascorbic acid, 100 nM dexamethasone, and 10 mM beta-glycerophosphate disodium salt hydrate, Lonza). Osteogenesis was induced over a period of two weeks, and a von Kossa staining kit (Fisher Sci.) was used to assess osteogenesis. The cells were fixed in 10% formalin and then incubated in 5% silver nitrate for 40 mins with exposure to ultraviolet light. The cells were washed in distilled water and then placed in 5% sodium thiosulfate for two mins, after which they were rinsed in distilled water and placed in nuclear fast red stain for five mins. After washing with distilled water, the slides were mounted and viewed under brightfield microscope.

3.2.10 Micro-CT imaging of labeled cells *in vitro*

Micro-CT imaging of *in vitro* phantoms was performed by using a X-SPECT Gamma Medica imager (Gamma Medica-Ideas, Northridge, Calif) with tube settings of 75.16 kV and 240.3 mA, a 64-mm detector setting, and 512 projections obtained at 1° for a full 360° rotation. Scanning was performed in a clockwise direction with X-ray tube–

to-detector distance of 269 mm and an X-ray tube-to-center of rotation distance of 225 mm. Images were reconstructed by using standard backprojection techniques, and the images were reconstructed into axial sections with 512×512 pixels per section. Images were processed by using imaging software (ImageJ).

3.2.11 Measurement of intracellular gold contents

After *in vitro* agarose phantom imaging, samples were assayed for gold content using inductively coupled plasma mass spectroscopy (ICP-MS) analysis (ELAN 6100; Perkin-Elmer SCIEX). A standard curve was used to quantify the amount of gold in the cells. Briefly, standard solutions were made by diluting AAS gold standard (Sigma-Aldrich) in the same background solution as that of the cell solutions. Intracellular gold concentration was calculated by dividing the total gold content by the number of cells or the volume of agarose.

3.2.12 Micro-CT imaging of labeled cells *in vivo*

Animal experiments were performed in accordance with a protocol

approved by Animal Care and Use Committee of the Johns Hopkins University School of Medicine. Sprague Dawley rat (weight of 350 g) were anesthetized with isoflurane (ISO), and positioned in a stereotaxic device (Stoelting, Wood Dale, IL, USA). A small skin incision was made in the midline to expose the skull. Using a motorized nanoinjector (Stoelting, Inc.) and 10 μ l Hamilton syringe (Hamilton, Reno, NV) with an attached 33 G needle with a total of 5.0×10^5 cells (different number of labeled hMSCs – 5×10^5 , 2×10^5 , 6×10^4 , and 2×10^4 cells, and unlabeled hMSCs) in 10 μ l of culture media, were injected into the putamen of mice, according to the following coordinates from bregma: anteroposterior [AP] = 0.0 mm; mediolateral [ML] = -3.5/ 3.5 mm; and dorsoventral [DV] = -5.0 mm. Cells were injected slowly over 10 min, and the needle was left in place for 1 min before being withdrawn. The incision was closed, and postoperative analgesia was provided with Ketofen.

Micro-CT imagings were performed using X-SPECT Gamma Medica imager (Gamma Medica-Ideas, Northridge, Calif) with tube settings of 75.16 kV and 240.3 mA, a 64-mm detector setting, and 512 projections obtained at 1° for a full 360° rotation.

3.2.13 Tissue section and immunostaining

Simultaneous multi-color immunofluorescence staining was performed. After perfusions, tissue sections were harvested from rat brain with cell transplants by the Microm HM 505 E Cryostat. After fixation with 4% paraformaldehyde, glass slides with tissues were dried for 1 h at 50 °C. After washing 3 times with PBS, tissues were blocked for 1 h with 0.1% Tryptone X and 10% normal goat serum (NGS), and then incubated with primary STEM121 (1:1000 dilution) antibody in PBS (pH 7.4) containing 0.02% sodium azide (Catal#: AB-121-U-050 StemCells, Inc.) for 24 h. Thereafter slides were washed 2 times with PBS for 5 min, and secondary antibodies were applied (1:300). After washing 2 times with PBS, slides were mounted with fluorogel with tris buffer (EMS catal# 17985-10) and viewed under fluorescence microscope. Negative controls were performed by omission of the primary antibody.

3.3 Results and Discussion

3.3.1 Preparation and characterizations of Au NPs-PLL(RITC) complexes

Colloidal Au NPs were prepared using well known citric acid reduction method similar to that reported previously.^[34,35] The Au NPs were observed to be of dark-red-colored aqueous suspension with a mean particle size of 40 nm in diameter which was examined by JEOL JEM-2010 transmission electron microscope operating at 200 kV.

However, citrate stabilized gold nanoparticles have negative surface charge, resulting in repulsion of the nanoparticles by the cell membrane,^[36] and thus, uptake would be prevented. Therefore, in order to enhance their uptake and higher accumulation in stem cells, cationic transfection agent was used. Transfection agents are macromolecules used for nonviral transfection of DNA into nucleus, and has been applied to efficiently label mammalian cells by electrostatic interactions.^[37,38] Moreover, rhodamine B-isothiocyanate (RITC) was conjugated to amino group in PLL complexes for fluorescence microscopic imaging availability as well (Figure 3.1a).^[39]

With particle size and a zeta potential analyzer, the electrophoretic (zeta) potential (ζ) and average size of the nanoparticles (citrate-stabilized gold nanoparticles and poly-L-lysine coated gold nanoparticles) were determined. Surface charge of gold nanoparticles in water changed from negatively charged (approximately $-30 \sim -40$ mV) to positively charged (approximately $+45$ mV for 40 nm; $+20$ mV for 20 nm and 10 nm, and $+15$ mV for 5 nm nanoparticles) by complexing with poly-L-lysine (see Table 3.1). From Table 3.2, it should be noted that smaller nanoparticles (5, 10 nm nanoparticles) were most likely to undergo aggregation in the presence of poly-L-lysine due to insufficient coating with poly-L-lysine, however, 40 nm gold nanoparticles were not aggregated, and homogenous Au NPs-PLL(RITC) complexes were produced (Figure 3.1b).

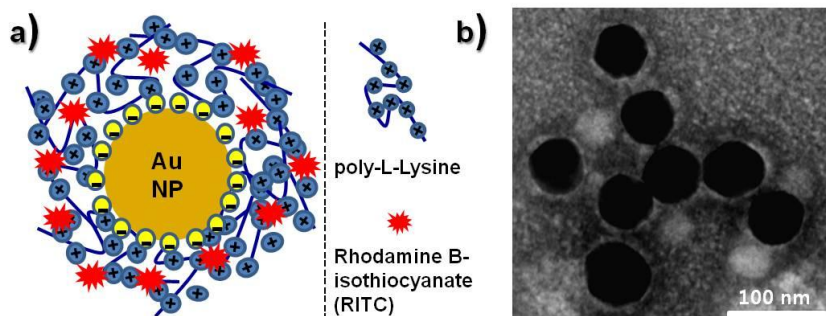


Figure 3.1. a) Schematic illustration of Au NPs-PLL(RITC) complexes.

b) TEM images of 40 nm Au NPs-PLL(RITC) complexes.

	Au NPs	Au NPs-PLL Complexes
5 nm	6.99 ± 0.35 nm	680.97 ± 50.64 nm
10 nm	9.05 ± 0.07 nm	198.23 ± 62.66 nm
20 nm	18.93 ± 0.91 nm	70.89 ± 19.97 nm
40 nm	38.24 ± 0.99 nm	43.78 ± 7.81 nm

Table 3.1. Hydrodynamic diameters of Au nanoparticles and Au NPs-PLL complexes.

	Au NPs	Au NPs-PLL Complexes
5 nm	-41.85 ± 13.93 mV	$+15.40 \pm 0.41$ mV
10 nm	-37.95 ± 1.91 mV	$+20.45 \pm 1.06$ mV
20 nm	-40.60 ± 0.99 mV	$+21.95 \pm 0.92$ mV
40 nm	-39.80 ± 0.42 mV	$+48.35 \pm 0.35$ mV

Table 3.2. Surface charge of Au nanoparticles and Au NPs-PLL complexes. Electrophoretic (zeta) potential (ζ) was measured with a particle size and zeta potential analyzer.

3.3.2 Human mesenchymal stem cell labeling and cellular uptake

Cellular uptake of Au NPs-PLL(RITC) complexes were investigated using brightfield microscopy, fluorescence microscopy, and transmission electron microscopy imaging as shown in Figure 3.2.

HMSCs were successfully labeled by the complexes. Cell morphology was preserved after labeling (Figure 3.2a). The complexes were found to accumulate in the perinuclear region in a similar fashion as that seen for cells labeled by superparamagnetic iron oxide nanoparticles (SPIO).^[40,41] In fluorescence microscopy images (Figure 3.2b), AuNP-PLL complexes which is conjugated with RITC were detected red on images, and DAPI-stained nuclei looked blue. In transmission electron microscopy images (Figure 3.2c), dark black gold nanoparticles are observed at intracellular region as well.

These findings investigated that cell labeling by PLL complexation enabled gold nanoparticles efficiently located and clustered in confined region in endosome or lysosome by means of endocytosis.^[42,43]

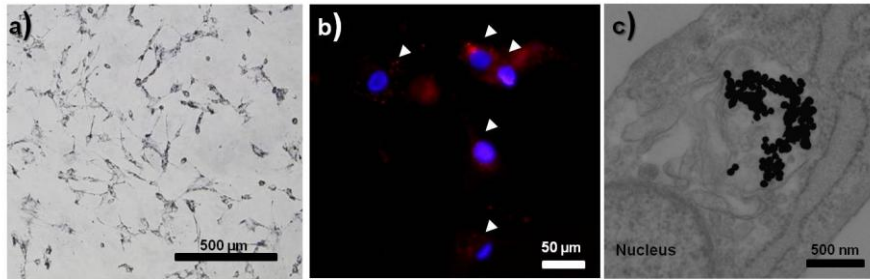


Figure 3.2. Cellular uptake of Au NPs-PLL(RITC) complexes to human mesenchymal stem cells. a) Brightfield microscopy images. b) Fluorescence microscopy images (blue: DAPI stained nucleus; red: Au NP-PLL(RITC) complexes). c) Transmission electron microscopy images.

3.3.3 Differentiation and viability of labeled hMSCs

To evaluate the possible cytotoxic effects of the Au NPs-PLL complexes on hMSCs, cell viability and proliferation was assessed with the MTS (3-(4,5-dimethylthiazol-2-yl)-5-(3-carboxymethoxyphenyl)-2-(4-sulfophenyl)-2H-tetrazolium) assay and Calcein-AM Assay. MTS assay is associated with the measurement of mitochondrial activity, and calcein-acetyoxymethyl (AM) enzyme assay is based on hydrolysis of Calcein-AM into fluorescent calcein by intracellular esterases.^[44] The results from both assays can be correlated with the number of viable cells. The viability of labeled hMSCs 24 hours post-incubation was 80-90% at a concentration of 0.1 mg Au/mL indicating that AuNP-PLL complexes labeling did not have a significant adverse effect on the cells (Figure 3.3).

Furthermore, the bipotent ability of MSCs to differentiate into specialized lineages after gold nanoparticle labeling was assessed in order to determine if hMSC function was maintained. Labeled hMSCs and unlabeled hMSCs were induced to differentiate into adipocyte and osteocyte (Figure 3.4). Figure 3.4b,d show the results of Oil Red O staining for assessing adipogenesis. Fatty lipid deposits were stained

red, which is indicative of adipogenesis. Labeled cells are successfully differentiated into adipogenic lineages, similarly to unlabeled hMSCs. Interestingly, labeled cells are examined even after differentiation in 3 weeks (indicated by white arrows). Figure 3.4c,e show the results of von Kossa staining for assessing osteogenesis. Calcium deposits were stained black, which is indicative of osteogenesis. The ability of labeled hMSCs to differentiate into osteocytes was also maintained similar to unlabeled hMSCs. These findings, taken together, indicate that Au NPs-PLL complexes do not impair cell viability, proliferation, and stem cell differentiation.

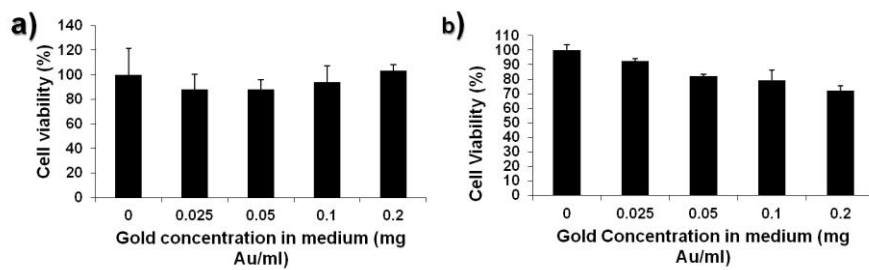


Figure 3.3. Assessment of cell viability and proliferation using a) MTS (3-(4,5-dimethylthiazol-2-yl)-5-(3-carboxymethoxyphenyl)-2-(4-sulfophenyl)-2H-tetrazolium) assay, and b) Calcein-AM assay. Different concentration of AuNPs-PLL(RITC) complexes were incubated with human mesenchymal stem cells for 1 day at 37 °C.

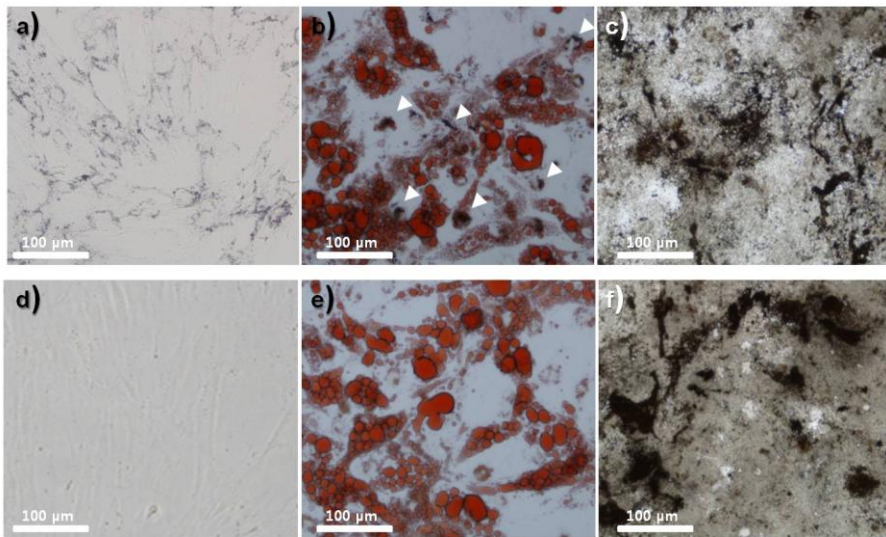


Figure 3.4. Differentiation of Labeled (a–c) and unlabeled hMSCs (d–f) and in 3 weeks (concentrations of Au NPs = 0.05 mgAu/ml) b, e) Adipogenic differentiation c, f) Osteogenic differentiation.

3.3.4 *In vitro* micro-CT imaging of labeled hMSCs

As mentioned previously, the goal of this study is to develop an imaging technique which can visualize and track hMSCs at sufficient depths and spatial/temporal resolutions by micro-CT imaging. Prior to *in vivo* imaging, capabilities of micro-CT imaging of hMSCs labeled with Au NPs-PLL complexes were evaluated.

Cell phantoms were prepared by suspending cells homogeneously in 1% agarose (1×10^6 cells/tube), and imaged by X-SPECT Gamma Media imager.

As shown in Figure 3.5a, labeled hMSCs exhibited a higher CT contrast compared to unlabeled cell phantom or agarose gel phantom. The average CT contrast values of unlabeled and labeled cell phantoms at different gold concentration in media (0, 0.025, 0.05, 0.1, and 0.2 mg Au/mL) were 45, 178, 425, 813, and 1449 HU, respectively. CT contrast value of agarose gel phantom was 35 HU.

Calculated HU values were increased by increasing the concentration of added gold nanoparticles which means that higher nanoparticle uptake was accomplished in cell phantoms of higher nanoparticle incubation (Figure 3.5b). When it was converted to intracellular gold

concentration versus HU, it demonstrated a linear pattern of CT contrast (Figure 3.5c) which means CT contrast is proportional to the amount of the contrast agent taken up by the cells.^[45] Therefore, the higher contrast enhancement in the labeled stem cells over the unlabeled cells suggested enhanced uptake of gold nanoparticles, thus leading to detectable CT contrast in the labeled stem cells.

In particular, when the plot of labeled cell phantom was compared with the corresponding free particle phantoms of same concentration, CT contrast of cell phantoms and free particle phantoms directly matched meaning no clustering effect in CT imaging and thus more precise quantitative cell labeling and tracking applications could be realized (Figure 3.6). In MR imaging with superparamagnetic iron oxide, the contrast from intracellular environment is higher than that of free particle phantoms because the aggregation of magnetic nanoparticles inside cells contribute to bigger magnetic inhomogeneity induction.^[46,47]

In vitro phantoms containing different number of labeled cells with Au NPs-PLL(RITC) complexes (0.1 mg Au/mL) in tube (0, 3.1×10^4 , 6.3×10^4 , 1.3×10^5 , 2.5×10^5 , 5×10^5 , and 1×10^6 cells in tube) were also imaged. As shown in Figure 3.7a, cell phantoms of 1×10^6 , 5×10^5 , 2.5

$\times 10^5$ cells (2×10^4 , 1×10^4 , 5×10^3 cells/ μ l in 1% agarose) in tube were detectable *in vitro* by micro-CT imaging. The average CT contrast values of unlabeled and labeled cell phantoms of different number of hMSCs were 41, 55, 69, 143, 271, 453, and 762 HU which showed a linear correlation in HU values versus the number of labeled cells (Figure 3.7b). From this plot, we can assess the number of transplanted cells for a particular HU value obtained by CT imaging.

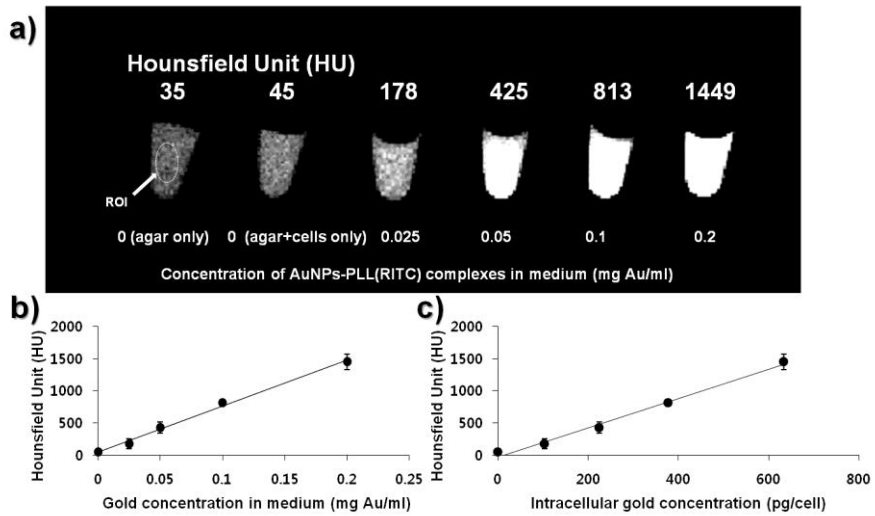


Figure 3.5. *In vitro* micro-CT imaging of hMSCs labeled with different concentrations of Au NPs-PLL(RITC) complexes. a) Micro-CT images and HU values of hMSCs suspended in 1% agarose (1×10^6 cells/tube). b) HU values vs. Au concentration used for labeling. c) HU values vs. intracellular Au concentration as measured by ICP-MS.

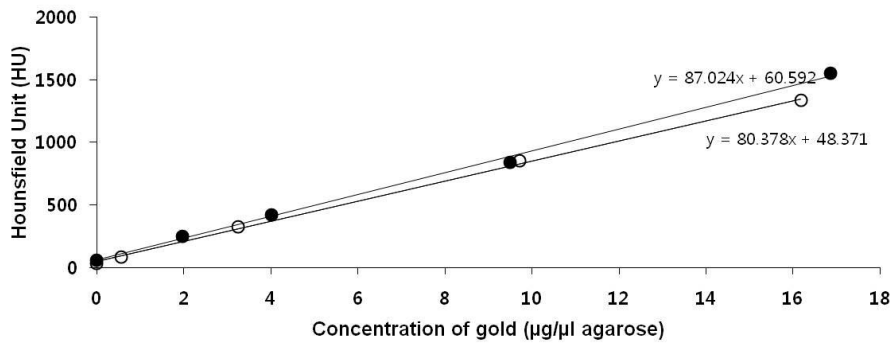


Figure 3.6. HU of labeled cell phantoms (○) versus HU of free gold nanoparticles phantoms (●).

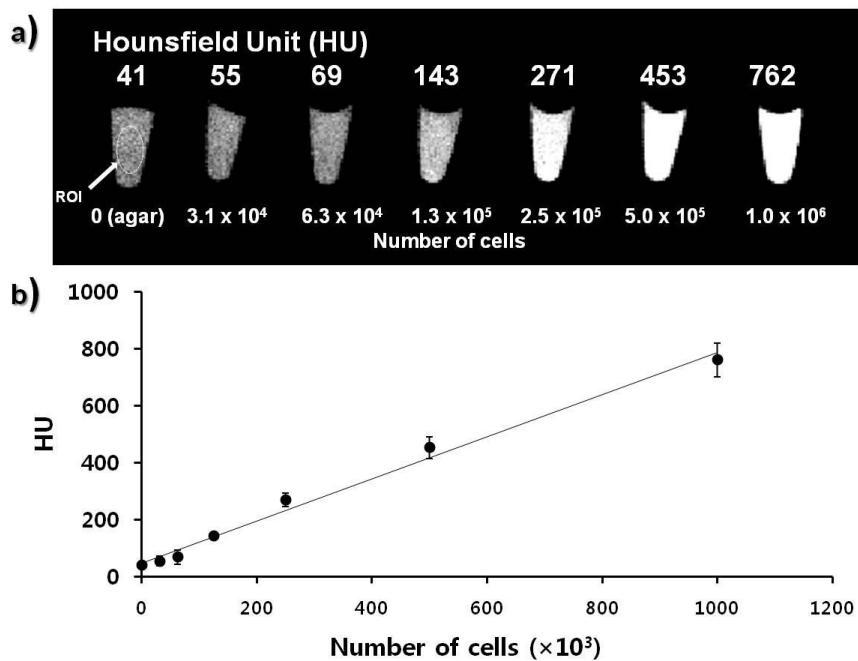


Figure 3.7. *In vitro* micro-CT imaging of different number of labeled hMSCs. a) Micro-CT images and HU of labeled hMSCs suspended in 1% agarose. b) A Plot of HU values vs. Number of cells labeled with Au NPs-PLL(RITC) complexes (0.1 mg Au/ml).

3.3.5 *In vivo* micro-CT imaging of labeled hMSCs

The feasibility of X-ray CT imaging in *in vivo* cell tracking was evaluated by monitoring the transplanted hMSCs labeled with Au NPs-PLL(RITC) complexes using micro-CT. Astolfo et al. recently demonstrated *in vivo* visualization of F98 tumor cells tracking loaded with gold nanoparticles by Monte Carlo calculations.^[48] Here, we investigated stem cells localization and tracking experimentally.

As shown in Figure 3.8a, different number of labeled cells with Au NPs-PLL(RITC) complexes (0.1mg Au/mL) was transplanted into parenchyma of rat brains and imaged 30 mins after transplantation *in vivo*. Cell transplanted groups (1, 2) exhibited much higher CT contrast with respect to typical soft tissue. As shown in Table 3.3, HU values were measured at the following locations and they were 1. cell transplant (5×10^5 cells) – 1445; 2. cell transplant (2×10^5 cells) – 505; 3. cell transplant (6×10^4 cells) – 145; 4. cell transplant (2×10^4 cells) – 76; 5. brain parenchyma – 60; 6. skull – 2340, respectively. 5×10^5 cells and 2×10^5 cells clusters are visible in micro-CT imaging. However, CT contrast was diminished for the number of cells lower than $\sim 1 \times 10^5$. From this study we can conclude that the detection limit

is $\sim 1 \times 10^4$ cells/ μ l in stem cell visualization by micro-CT imaging.

After sacrificing rat and obtaining tissue sections 1 day after transplantation, immunostaining was performed to confirm the engraftment of transplanted hMSCs. STEM121 is human-specific mouse monoclonal antibody which recognizes a cytoplasmic protein of human cells, and improves the visualization of transplanted human cells. As shown in Figure 3.8b, the cytoplasm of human cells was detected green and red signals from rhodamin dye conjugated Au NPs-PLL complexes were also detected.

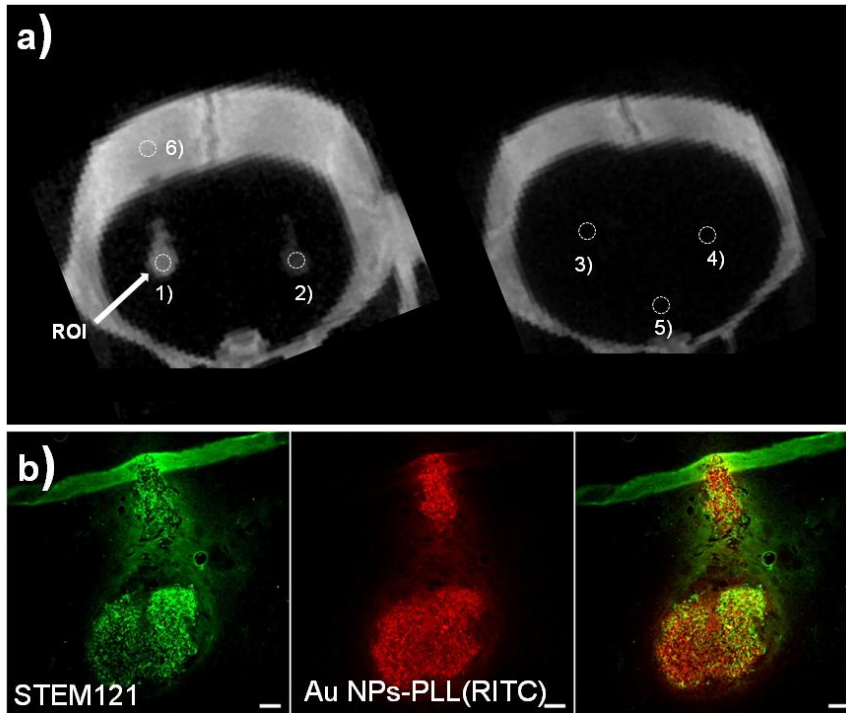


Figure 3.8. *In vivo* micro-CT images of transplanted hMSCs by stereotaxic injection. a) Different number of cells labeled with Au NPs-PLL(RITC) complexes (0.1 mg Au/ml) were transplanted into parenchyma of rat brain. 1) 5×10^5 cells; 2) 2×10^5 cells; 3) 6×10^4 cells; 4) 2×10^4 cells. b) Immunofluorescence images of the corresponding brain tissue section in a). Left) Transplanted hMSCs are stained with anti-human cytoplasmic (STEM121) antibody (green). Middle) Au NPs-PLL(RITC) complexes (red). Right) Overlapped image of the left and the middle image. Scale bar = 200 μ m.

ROI	Description	HU value
1	5×10^5 cells	1445
2	2×10^5 cells	505
3	6×10^4 cells	145
4	2×10^4 cells	76
5	Brain parenchyma	60
6	Skull	2340

Table 3.3. HU measurements performed at the following locations in Figure 3.8. 1) Cell transplant: 5×10^5 cells; 2) Cell transplant: 2×10^5 cells; 3) Cell transplant: 6×10^4 cells; 4) Cell transplant: 2×10^4 cells; 5) Brain parenchyma; 6) Skull.

3.4 Conclusion

In summary, 40 nm Au NPs were readily complexed with PLL, and hMSCs were successfully labeled by these Au NPs-PLL complexes. Cell morphology was preserved after labeling, and the complexes were found to accumulate in the perinuclear region. Importantly, labeling does not impair cellular viability, proliferation, and stem cell differentiation. Labeled hMSCs can be visualized *in vitro* and tracked *in vivo* using micro-CT imaging. Detection limit of labeled hMSCs by gold nanoparticles was revealed to be $\sim 1 \times 10^4$ cells/ μl *in vivo*. This study represents one of the first attempts to develop CT cell tracking, and furthermore, Au NPs-PLL complexes cellular labeling may find applications in CT image-guided interventions and fluoroscopic procedures commonly used for injection of molecular and cellular therapeutics.

3.5 References

- [1] Carpenter, M. K.; Frey-Vasconcells, J.; Rao, M. S. *Nat. Biotechnol.*, **2009**, 27, 606.
- [2] Zimmermann, W. H.; Melnychenko, I.; Wasmeier, G. Didie, M.; Naito, H.; Nixdorff, U.; Hess, A.; Budinsky, L.; Brune, K.; Michaelis, B.; Dhein, S.; Schwoerer, A.; Ehmke, H.; Eschenhagen, T. *Nat. Med.* **2006**, 12, 452.
- [3] Petite, H.; Viateau, V.; Bensaïd, W.; Meunier, A.; de Pollak, C.; Bourguignon, M.; Oudina, K.; Sedel, L.; Guillemin, G. *Nat Biotechnol.* **2000**, 18, 959.
- [4] Djouad, F.; Mrugala, D.; Noël, D.; Jorgensen, C. *Regern. Med.* **2006**, 1, 529.
- [5] Badorff, C.; Brandes, R. P.; Popp, R.; Rupp, S.; Urbich, C.; Aicher, A.; Fleming, I.; Busse, R.; Zeiher, A. M.; Dimmeler, S. *Circulation* **2003**, 107, 1024.
- [6] Liechty, K. W.; MacKenzie, T. C. Shaaban, A. F.; Radu, A.; Moseley, A. B.; Deans, R.; Marshark, D. R.; Flake, A. W. *Nat. Med.* **2000**, 6, 1282.
- [7] Pittenger, M. F.; Mackay, A. M.; Beck, S. C.; Jaiswal, R. K.; Douglas, R.; Mosca, D.; Moorman, M. A.; Simonetti, D. W.; Craig, S.; Marshak D. R. *Science* **1999**, 284, 143.

- [8] Bulte, J. W.; Kraitchman, D. L. *NMR Biomed.* **2004**, *17*, 484.
- [9] Janowski, M.; Bulte, J. W.; Walczak P. *Adv. Drug Deliv. Rev.* **2011**, *64*, 1488.
- [10] Bhirde, A.; Xie, J.; Swierczewska, M.; Chen, X. *Nanoscale* **2011**, *3*, 142.
- [11] Weissleder, R.; Pittet, M. J. *Nature* **2008**, *452*, 580.
- [12] Willmann, J. K.; van Bruggen, N.; Dinkelborg L. M.; Gambhir, S. S. *Nat. Rev. Drug Discover.* **2008**, *7*, 591.
- [13] Schwenzer, N. F.; Springer, F.; Schraml, C.; Stefan, N.; Machann, J.; Schick, F. *J. Hepatol.* **2009**, *51*, 433.
- [14] Yu S.-B.; Watson A. D. *Chem. Rev.* **1999**, *99*, 2353.
- [15] Liu, L.; Ai, K. Lu, L. *Acc. Chem. Res.* **2012**, *45*, 1817.
- [16] Shilo, M.; Reuveni, T.; Motiei, M.; Popovtzer, R. *Nanomedicine* **2012**, *7*, 257.
- [17] Cai, W.; Chen, X. *Small* **2007**, *3*, 1840.
- [18] Pan, D.; Lanza, G. M.; Wickline, S. A.; Caruthers, S. D. *Eur. J. Radiol.* **2009**, *70*, 274.
- [19] Rabin, O.; Perez, J. M.; Grimm, J.; Wojtkiewicz, G.; Weissleder, R. *Nat. Mater.* **2006**, *5*, 118.
- [20] Liu, Y.; Ai, K.; Liu, J.; Yuan, Q.; He, Y.; Lu, L. *Angew. Chem. Int. Ed.* **2012**, *51*, 1437.

- [21] Oh, M. H.; Lee, N.; Kim, H.; Park, S. P.; Piao, Y.; Lee, J.; Jun, S. W.; Moon, W. K.; Choi, S. H.; Hyeon, T. *J. Am. Chem. Soc.* **2007**, *133*, 5508.
- [22] Bonitatibus Jr., P. J.; Torres, A. S.; Goddard, G. D.; FitzGerald, P. F.; Kulkarni, A. M. *Chem. Commun.* **2010**, *46*, 8956.
- [23] Popovtzer, R.; Agrawal, A.; Kotov, N. A.; Popovtzer, A.; Balter, J.; Carey, T. E.; Kopelman R. *Nano Lett.* **2008**, *8*, 4593.
- [24] Kim, D.; Park, S.; Lee, J. H.; Jeong, Y. Y.; Jon, S. *J. Am. Chem. Soc.* **2007**, *129*, 7661.
- [25] Hainfeld, J. F.; Slatkin, D. N.; Focella, T. M.; Smilowitz, H. M. *Br. J. Radiol.* **2006**, *79*, 248.
- [26] Sun, I.-C.; Eun, D.-K.; Na, J. H.; Lee, S.; Kim, I.-J.; Youn, I.-C.; Ko, C.-Y.; Kim, H.-S.; Lim, D.; Choi, K.; Messersmith, P. B.; Park, T. G.; Kim, S. Y.; Kwon, I. C.; Kim, K.; Ahn C.-H. *Chem. Eur. J.* **2009**, *15*, 13341.
- [27] Xi, D.; Dong, S.; Lu, Q.; Meng, L.; Ye J. *RSC Adv.* **2012**, *2*, 12515.
- [28] Jackson, P.A.; Rahman, W.N.; Wong, C.J.; Ackerly, T.; Geso, M. *Eur. J. Radiol.* **2010**, *75*, 104
- [29] Hubbell, J. H.; Seltzer, S. M. X-Ray Mass Attenuation Coefficients. Online, <http://physics.nist.gov/PhysRefData/XrayMassCoef>. **2009**.
- [30] Xu, C; Tung, G. A.; Sun, S. *Chem. Mater.* **2008**, *20*, 4167.
- [31] Alkilany, A. M.; Murphy C. J. *J. Nanopart. Res.* **2010**, *12*, 2313.

- [32] Connor, E. E.; Mwamuka, J.; Gole, A.; Murphy, C. J.; Wyatt, M. D. *Small* **2005**, *1*, 325.
- [33] Ricles, L. M.; Nam, S. Y.; Sokolov, K.; Emelianov, S. Y.; Suggs, L. J. *Int. J. Nanomed.* **2011**, *6*, 407.
- [34] Enustun B. V.; Turkevich J. *J. Am. Chem. Soc.* **1963**, *85*, 3317.
- [35] Ji, X.; Song, X.; Bai, Y.; Yang, W.; Peng, X. *J. Am. Chem. Soc.* **2007**, *129*, 13939.
- [36] Zhdanov, R. I.; Podobed, O. V.; Vlassov, V. V. *Bioelectrochemistry* **2002**, *58*, 53.
- [37] Gershon, H.; Ghirlando, R.; Guttman, S. B.; Minsky, A. *Biochemistry* **1993**, *32*, 7143.
- [38] Kalish, H.; Arbab, A. S.; Miller, B. R.; Lewis, B. K.; Zywicke, H. A.; Bulte, J. W.; Bryant Jr., L. H.; Frank, J. A. *Magn. Reson. Med.* **2003**, *50*, 275.
- [39] Zhou, D.; Li, C.; Hu, Y.; Zhou, H.; Zhang, Z.; Guo, T. *J. Mater. Chem.* **2012**, *22*, 10743.
- [40] Frank, J. A.; Miller, B. R.; Arbab, A. S.; Zywicke, H. A.; Jordan, E. K.; Lewis, B. K.; Bryant, Jr, L. H.; Bulte, J. W. *Radiology* **2003**, *228*, 480.
- [41] Kim, H. S.; Oh, S. Y.; Joo, H. J.; Son, K.-R.; Song, I.-C.; Moon W. K. *NMR Biomed.* **2010**, *23*, 514.

- [42] Mailander, V.; Landfester K. *Biomacromol.* **2009**, *10*, 2379.
- [43] Shukla, R.; Bansal, V.; Chaudhary, M.; Basu, A.; Bhonde, R. R.; Sastry, M. *Langmuir* **2005**, *21*, 10644.
- [44] Gilad, A. A.; Walczak, P.; McMahon, M. T.; Na, H. B.; Lee, J. H.; An, K.; Hyeon, T.; van Zijl, P. C. M.; Bulte, J. W. *Magn. Reson. Med.* **2008**, *60*, 1.
- [45] Galper, M. W.; Saung, M. T.; Fuster, V.; Roessl, E.; Thran, A.; Proksa, R.; Fayad, Z. A.; Cormode, D. P. *Invest. Radiol.* **2012**, *47*, 475.
- [46] Roch, A.; Gossuin, Y.; Muller, R. N.; Gillis, P. J. *Magn. Mater.* **2005**, *293*, 532.
- [47] Perez, J. M.; Josephson, L.; O'Loughlin, T.; Hogemann, D.; Weissleder, R. *Nat. Biotechnol.* **2002**, *20*, 816.
- [48] Astolfo, A.; Schültke, E.; Menk, R. H.; Kirch, R. D.; Juurlink, B. H.; Hall, C.; Harsan, L.A.; Stebel, M.; Barbetta, D.; Tromba, G.; Arfelli, F. *Nanomedicine* **2012** ASAP. DOI: 10.1016/j.nano.2012.06.004

Chapter 4. Ceria Nanoparticles that can Protect against Ischemic Stroke

4.1 Introduction

Ischemic stroke is the leading cause of adult disability in the United States and the second leading cause of death worldwide.^[1] Reactive oxygen species (ROS) such as the superoxide anion ($O_2^{\bullet-}$), hydrogen peroxide (H_2O_2), and hydroxyl radical (HO^{\bullet}), are generated and accumulate during ischemic periods. These species induce oxidative damage, which is one of the most critical mechanisms responsible for causing ischemic injury,^[2] and oxidative damage elicits stroke-related cell death mechanisms, such as apoptosis.^[3] As a result, neuronal networks and neurovascular units are completely destroyed, and the brain function is stopped. However, no effective neuroprotective therapy for ischemic stroke has been developed for clinical practice. Despite the availability of antioxidant drugs, no treatments have been proven to protect against oxidative damage after acute ischemic stroke in humans.

Ceria nanoparticles are known to exhibit free radical scavenging activity by reversibly binding oxygen and shifting between the Ce^{3+} (reduced) and Ce^{4+} (oxidized) forms at the particle surface.^[4] From the crystal structure of ceria nanoparticles, cerium ions mostly exist in the valence state of Ce^{4+} , however, reduction in particle size results in oxygen vacancies from the particle surface, which allows the coexistence of Ce^{3+} .^[5] Moreover, the catalytic properties of ceria nanoparticles can be further enhanced by using ultrasmall nanoparticles of < 4 nm.^[6] The ability of ceria nanoparticles to switch between oxidation states and scavenge free radicals is comparable to biological antioxidants. In fact, it was recently reported that ceria nanoparticles exhibit superoxide dismutase-mimetic activity^[7,8] and catalase-mimetic activity^[9,10] to protect cells against two dominant ROS, the superoxide anion and hydrogen peroxide. Here, we report that ceria nanoparticles can protect against ischemic stroke in an *in vivo* animal model.

4.2 Experimental Section

4.2.1 Chemicals

Cerium acetate (98%), xylene (98.5%+), hydrogen peroxide (H₂O₂, 30%), and rhodamine B isothiocyanate (RITC) were purchased from Sigma-Aldrich Inc (St. Louis, MO, USA). Oleylamine (approximate C₁₈-content of 80–90%) was purchased from Acros Organics (Geel, Belgium). n-Hexane (99%), ethanol (99%), chloroform (99%), and acetone (99%) were purchased from Samchun Chemicals. 1,2-Distearoyl-*sn*-glycero-3-phosphoethanolamine-*N*-[methoxy(polyethylene glycol)-2000] (mPEG-2000 PE) and 1,2-distearoyl-*sn*-glycero-3-phosphoethanolamine-*N*-[amino(polyethylene glycol)-2000] (DSPE-PEG(2000) amine) were purchased from Avanti Polar Lipids Inc (AL, USA). SOD assay kit was purchased from Dojindo Laboratories (Japan) and Amplex® Red Hydrogen Peroxide/Peroxidase assay kit was purchased from Molecular Probes Inc (Eugene, OR, USA).

4.2.2 Synthesis of ceria nanoparticles

One millimole (0.43 g) of cerium(III) acetate (98%, Sigma-Aldrich) and 12 mmol (3.25g) of oleylamine (approximate C₁₈-content of 80–90%, Acros Organics) were added to 15 mL xylene (98.5%, Sigma-Aldrich). The resulting solution was stirred for 2 h at room temperature and then heated to 90 °C under vacuum. One milliliter of deionized water was injected into the solution under vigorous stirring at 90 °C, and the solution color changed to an off-white color, demonstrating that the reaction had occurred. The resulting mixture was aged at 90 °C for 3 h to give a light yellow colloidal solution, which was then cooled to room temperature. Ethanol (100 mL) was added to the precipitated ceria nanoparticles. The precipitate was washed with ethanol and acetone using centrifugation, and the resulting ceria nanoparticles were easily dispersible in organic solvents, such as n-hexane and chloroform. For large-scale synthesis, we used a 10-fold increase in the volume of these reagents.

4.2.3 Synthesis of phospholipid-PEG-capped ceria nanoparticles

To make biocompatible ceria nanoparticles, ceria nanoparticles

dispersed in chloroform were encapsulated by a PEG-phospholipid shell. First, 5 mL ceria nanoparticles in CHCl_3 (10 mg/mL) was mixed with 5 mL CHCl_3 solution containing 50 mg of mPEG-2000 PE. Then, solvents were evaporated by rotary evaporator and incubated at 80 °C in vacuum for 1 h. The addition of 5 mL water resulted in a clear and light-yellowish suspension. After filtration, excess mPEG-2000 PE was removed using ultracentrifugation. Purified phospholipid-PEG-capped ceria nanoparticles were dispersed in distilled water.

4.2.4 RITC-conjugated ceria nanoparticles

First, ceria nanoparticles dispersed in chloroform were encapsulated by amine-functionalized PEG lipid and PEG-phospholipid shells. Five milliliters of ceria nanoparticles in CHCl_3 (10 mg/mL) was mixed with 5 mL CHCl_3 solution containing 45 mg mPEG-2000 PE and 5 mg DSPE-PEG(2000) amine. After evaporation of the solvent and subsequent filtration, ceria nanoparticles were dispersed in water. Amine groups were available for the attachment of RITC molecules. Five milligrams RITC was added, and the solution was stirred for 6 h. After ultracentrifugation, RITC-conjugated ceria nanoparticles were

dispersed in distilled water.

4.2.5 Characterization of phospholipid-PEG-capped ceria nanoparticles

Transmission electron microscope (TEM) analysis was conducted using a JEOL JEM-2010 TEM operating at 200 kV. Samples were prepared by casting a drop of the ceria nanoparticle dispersion onto a carbon-coated copper grid. XRD patterns were obtained using a Rigaku D/Max-3C diffractometer equipped with a rotation anode and a Cu K α radiation source ($\lambda = 0.15418$ nm). Phase identification was performed using JCPDS-ICDD 2000 software (The International Centre for Diffraction Data; ICDD). XPS experiments were performed using a multipurpose surface analysis system (Sigma Probe, Thermo, UK). The photoelectron spectra were excited by an Al K α (1486.6 eV) anode operating at 100 W. The base pressure during XPS analysis was maintained at less than 10^{-9} mbar, and the binding energy scale was calibrated from the C 1s peak at 285 eV. The 3d peak positions of ceria were then fitted using PeakFit (version 4.0) software (Systat Software, Chicago, IL, USA). UV/Vis absorbance measurements were taken

using a JASCO V-550 instrument. DLS measurements were obtained using a particle size analyzer (ELS-Z, Otsuka Electronics, Japan). Elemental analysis was performed using inductively coupled plasma atomic emission spectrometer (ICP-AES, Shimadzu ICPS-1000IV-JAPAN) and an inductively coupled plasma mass spectrometer (ICP-MS, ELAN 6100, Perkin-Elmer SCIEX). The 3-[4,5-dimethylthiazol-2-yl]-2,5-diphenyltetrazolium bromide (MTT) assay was conducted using a Multiple Plate Reader (Victor3, manufactured by Perkin Elmer, USA).

4.2.6 SOD mimetic activity assay

The superoxide anion scavenging activity was assessed with SOD assay kit (Dojindo Laboratories, Japan). First, ceria nanoparticle solutions of different concentrations (0, 0.2, 0.4, 0.8, and 1.6 mM) were mixed with 200 μ L of WST-1 working solution. The reaction was initiated with the addition of 20 μ L of xanthine oxidase solution. After incubating plate at 37 $^{\circ}$ C for 20 min, the absorbance at 450 nm was measured using a micro plate reader (Victor3). Since the absorbance is proportional to the amount of superoxide anion, the SOD mimetic

activity could be measured by quantifying the decrease of the color development at 450 nm.

4.2.7 Catalase mimetic activity assay

Quenching activities of hydrogen peroxide were quantified using Amplex[®] Red Hydrogen Peroxide/Peroxidase assay kit (Molecular Probes Inc.). Amplex Red reagent (10-acetyl-3,7-dihydroxyphenoxazine) reacts with H₂O₂, in the presence of horseradish peroxidase (HRP), to produce the red fluorescent resorufin. The fluorescence of resorufin (excitation at 571 nm and emission at 585 nm) indicates the H₂O₂ levels in the samples. First, a H₂O₂ standard curve was prepared and used to determine H₂O₂ concentration in each sample. After pipetting 50 µL of ceria nanoparticle solutions of different concentrations (0, 0.125, 0.25, 0.75, and 1.5 mM) into each micro well, 2 µM of H₂O₂ solutions in the final concentration were added to nanoparticle samples and pre-incubated for 5 mins. 50 µL of the Amplex[®] Red reagent/HRP working solution was added and reactions were initiated. The fluorescence was measured after incubating for 30 min with protection from light.

4.2.8 Autocatalytic activity of ceria nanoparticles

The autocatalytic activity of ceria nanoparticles was examined by color change and UV/Vis spectroscopy. A drop of H₂O₂ solutions with various concentrations (0, 0.1, 0.5, and 1 M), as a source of hydroxyl radicals to mimic *in vivo* oxidative stress, were added to PBS solutions containing 5 mM ceria nanoparticles. As a control, nanoparticle dispersion without H₂O₂ was used. When more H₂O₂ was added to the ceria nanoparticle dispersion, the solution color changed from light yellow to orange, demonstrating that more Ce³⁺ species were generated by the addition of H₂O₂. In UV/Vis spectroscopy, upon the addition of H₂O₂, the shoulder between 300 and 400 nm was significantly red-shifted. This color change and absorption shift was derived from the oxidation of Ce⁴⁺ species on the particle surface to Ce³⁺ by H₂O₂. During the following 3 weeks, the H₂O₂ in the solution decomposed, and the observed orange color disappeared because the Ce⁴⁺ regeneration occurred. The subsequent addition of H₂O₂ converted the light yellow color to orange again. This reversible autocatalytic activity of ceria nanoparticles is the key to their potential biomedical application as antioxidants *in vivo*.

4.2.9 Cell culture

Mammalian CHO-K1 cells were grown in monolayers in 89% RPMI 1640 with L-glutamine (300 mg/L), 25 mM HEPES, and 25 mM NaHCO₃ supplemented with 10% heat-inactivated fetal bovine serum (FBS; Gibco) and penicillin/streptomycin (100 U/mL and 100 µg/mL, respectively; Gibco) in a humidified 5% CO₂ atmosphere at 37 °C. Cells were cultured in 80-cm² flasks overnight to 80–90% confluence.

4.2.10 Fluorescence microscopy of cellular uptake

To observe the cellular uptake of ceria nanoparticles, CHO-K1 cells were cultured in a 6-well plate (nonpyrogenic; BD Falcon, BD Bioscience, San Diego, CA, USA). Next, 200 µL ceria nanoparticles (0.1 mg Ce/ml = 0.7 mM) was added to each well, and the cells were incubated. After 1 h, the cells were washed with PBS 2 times, fixed with 2.5% paraformaldehyde, and stained with DAPI (2 µg/ml in PBS, Sigma-Aldrich). Red fluorescence was detected under the fluorescence microscope with an excitation of 350 nm and an emission of 470 nm for DAPI and with excitation of 540 nm and an emission of 625 nm for

RITC.

4.2.11 Intracellular ROS and cell viability assay

CHO-K1 cells were initially seeded in triplicate in 96-well plates at a density of 25,000 cells per well and were grown in culture medium for 24 h at 37 °C. Cells were washed with PBS 2 times, and the 1 mM tBHP solution was added, and incubated for 1 h. After washing with PBS, medium alone or medium containing ceria nanoparticles (0.125 or 0.25 mM) was added into each well. Six hours after treatment, an MTT assay (Sigma-Aldrich) was performed for viability. Twenty microliters of a 5 mg/mL solution of MTT was added to each well, and cells were incubated for additional 2 h at 37 °C in a humidified 5% CO₂ atmosphere. The supernatant was aspirated, and the cells were dissolved in 200 µL DMSO. After shaking for 30 mins, the absorbance was measured at 540 nm using a 96-well plate reader (Victor3).

4.2.12 Fluorescence-activated cell sorting (FACS) analysis

Cells were stained with FITC-conjugated ceria nanoparticles. Using BD FACSCalibur (BD Bioscience), we obtained relative optical densities of cells which absorbed fluorescent dye-conjugated ceria nanoparticles in various concentrations and time.

4.2.13 Animals

Male Sprague-Dawley rats (Koatech, Seoul, Republic of Korea), each weighing between 200 and 220g, were used in these experiments. All animal studies were carried out according to the National Institutes of Health Guide of the Institutional Animal Care and Use Committee of the Biomedical Research Institute at Seoul National University Hospital. Every effort was made to minimize animal suffering and to limit the number of animals used.

4.2.14 Focal ischemia-reperfusion model and the injection of ceria nanoparticles

Focal cerebral ischemia-perfusion was induced with a minor modification of the endovascular internal carotid artery (ICA) suture

method developed by E. Z. Longa, P. R. Weinstein, S. Carlson, R. Cummins, *Stroke* **1989**, 20, 84. After inhalation anesthesia using 3% isoflurane in 30% oxygen and 70% air, the left common carotid artery (CCA) was exposed at its bifurcation using a midline cervical incision. The external carotid artery (ECA), ICA, and CCA were ligated using a 5-0 silk suture. The CCA was then transected, and a 5-0 nylon monofilament suture (with its tip rounded by heating) was inserted into the CCA. To occlude the origins of the MCA and proximal anterior cerebral artery, the suture was advanced into the ICA for a distance of 20 mm. The suture was secured in place using a ligature, and the wound was closed. The monofilament was removed 60 min after the occlusion. The animals were allowed food and water ad libitum. Seizure events were not observed during the experiments at any time after the MCA occlusion. Rectal temperature was maintained at 37 ± 0.5 °C using a thermistor-controlled heating blanket. We administered various doses of ceria nanoparticles (0.1, 0.3, 0.5, 0.7, 1.0, and 1.5 mg/kg) or PBS intravenously immediately after reperfusion to detect optimal doses.

4.2.15 Measurement of infarct volumes

After cardiac perfusion-fixation with 4% paraformaldehyde in 0.1 mol/L PBS, brains were removed quickly and cut into 30- μ m-thick coronal sections on a freezing microtome. Ten brain sections were mounted onto glass slides, and processed for Nissl staining. Infarct volumes were measured using an image analysis program, ImageJ (National Institutes of Health, Bethesda, MD).

4.2.16 In situ labeling of DNA fragmentation

Terminal deoxynucleotidyl transferase-mediated dUTP-biotin nick end labeling (TUNEL) was performed with the use of a commercially available kit. Sections were incubated in a TdT-labeling reaction mixture for 90 min, colored with DAB solution, and counterstained with methyl green. A single axial section through the center of the hemorrhagic lesion was analyzed. Eight sampling regions were placed along the periphery. TUNEL-positive cells were identified and counted. Total counts in these sampling regions were converted into cell densities for quantification and comparison between the treatment groups. According to morphological criteria, apoptosis-specific

TUNEL-positive nuclei with chromatin condensation and fragmented nuclei (>2 apoptotic bodies) were considered probable apoptotic cells, while nonapoptotic TUNEL-positive cells exhibited diffuse light labeling of nuclei.

4.2.17 Biodistribution of ceria nanoparticles

At 24 h after injection of ceria nanoparticles, rats with focal cerebral ischemia were decapitated to rapidly harvest the brain and other organs. Post-mortem samples were obtained to determine ceria concentrations in the brain, heart, kidneys, liver, and blood, using inductively coupled plasma-mass spectrometry (ICP-MS). After the injection of ceria nanoparticles without inducing focal ischemia, brain samples were obtained to evaluate the effects of focal ischemia on the concentration of ceria in the brain.

4.2.18 ICP-MS analysis

Determination of cerium content in organs was performed by ICP-MS analysis (ELAN 6100, Perkin-Elmer SCIEX). Organs were dissolved in

aqua regia. The resulting solutions were diluted in HNO₃ (2%, 2 ppb, 1:300 v/v for the brain, heart, spleen, lung, liver, and kidneys).

4.2.19 Tracking of ceria nanoparticles

After 60 min of occlusion-reperfusion, RITC-conjugated ceria nanoparticles were injected intravenously. At 6 h after ceria injection, rats were sacrificed and the brains were examined under a confocal laser scanning biological microscope (LSM 410 META; Carl Zeiss, Jena, Germany). To evaluate the distribution of ceria nanoparticles in the ischemic brain, we conducted computerized visual augmentation using 3-dimensional reconstruction of the fluorescence signals. After adding 1,250 high-power field images, a raw image of the whole brain was created. These raw images were imported from the LSM Image Examiner Version 4.0 (Carl Zeiss MicroImaging GmbH, Germany). Visible sediments on scanned images were manually excluded using Photoshop (Adobe Systems Inc., USA), and images were then converted by the ImageJ 1.44 (NIH, Bethesda, Maryland, USA) plugin Auto Threshold, which converts 8-bit images to binary images, to facilitate automatic particle filtering. To suppress the remaining

background noise, we used the “Analyze Particles” mode in ImageJ. Extracted (x,y) data values from the processed images were computed to save kernel density estimates in SAS 9.2 software (SAS Institute Inc., Cary, NC, USA). Calculated (x,y,density) data values were then reincorporated to generate 3-dimensional contour plots in ImageJ. We then overlapped original rat brain images with scatter plots of ceria nanoparticles drawn by R version 2.14.

4.2.20 Detection of ROS *in vivo*

Production of ROS during cerebral ischemia was investigated using a previously reported hydroethidine (HEt) method. An HEt solution (100 μ L, 20 mg/mL in DMSO; Sigma-Aldrich) was administered 15 min before the induction of ischemia. Animals were killed 4 h after the induction of ischemia using transcardial perfusion. Fluorescence was assessed microscopically at an excitation wavelength of 355 nm and an emission wavelength of greater than 415 nm for HEt detection or at an excitation wavelength of greater than 510–550 nm and an emission wavelength of greater than 580 nm for oxidized HEt detection.

4.2.21 Lipid peroxides assay

Malondialdehyde was estimated as an indicator of lipid peroxidation. The malondialdehyde level in the brain tissue at 24 hrs after stroke was measured using the thiobarbituric acid reduction method with a commercially available kit (Cell Biolabs, San Diego, CA, USA).

4.2.22 Western blot analysis

Twenty-four hours after the induction of focal ischemia, rats were sacrificed by decapitation, and the brains were extracted. After centrifugation of hemisphere homogenates, 50 µg of protein was separated on a 10% sodium dodecyl sulfate-polyacrylamide gel and transferred onto a nitrocellulose membrane. Membranes were incubated in blocking buffer (5% skim milk in 50 mM Tris, pH 7.5, 0.15 mM NaCl, 0.05% Tween-20), and the blots were probed with antibodies for p53, phospho-p53, caspase-3, cleaved caspase-3, and gelsolin (Cell Signaling Technology, Danvers, MA). Immunoreactivity was visualized using enhanced chemiluminescence, and relative densities were determined by comparing measured values with me

an values of the control group.

4.2.23 Statistical analysis

Values are presented as the mean \pm standard deviation. Data were analyzed using the Student's *t*-test for normally distributed unpaired samples. The nonparametric Mann-Whitney U test or Wilcoxon signed-rank test was used for unpaired or paired samples, respectively. A 2-tailed *p*-value of less than 0.05 was considered significant. All statistical analyses were performed using SPSS version 19.0 (SPSS Inc., Chicago, IL, USA).

4.3 Results and Discussion

4.3.1 Synthesis and characterizations of ceria nanoparticles

Ceria nanoparticles were prepared using a modified reverse micelle method,^[11] which enabled the synthesis of uniformly sized ceria nanoparticles under facile and mild reaction conditions. Transmission electron microscope (TEM) images revealed discrete and uniform 3 nm-sized ceria nanoparticles (Figure 4.1a). High-resolution TEM images revealed a cross-lattice pattern, demonstrating the highly crystalline nature of these particles, despite the low reaction temperature (Figure 4.1b). The selected area electron diffraction (SAED) pattern (Figure 4.1c) and X-ray diffraction (XRD) pattern (Figure 4.2) revealed a cubic fluorite structure (JCPDS card no. 34-0394). The particle size, estimated using the Scherrer formula, was 3.3 nm, which matched very well with that measured using TEM. In contrast to the white color of pure CeO₂, the prepared nanoparticles exhibited a yellowish color because they were composed of not only cerium(IV) oxide but also cerium(III) oxide.^[12] X-ray photoelectron spectroscopy (XPS) analysis was used to identify the valence state of

Ce³⁺ (peaks at 885.0 and 903.5 eV) and Ce⁴⁺ (peaks at 882.1, 888.1, 898.0, 900.9, 906.4, and 916.40 eV), confirming the mixed valence state (Figure 4.3).^[7]

Good colloidal stability and narrow size distribution are essential for the successful biomedical application of ceria nanoparticles. Because of the strong hydrophobic nature of the synthesized ceria nanoparticles, we used PEGylation method for stabilization, enabling the nanoparticles to circulate longer in the blood stream by reducing nonspecific binding and uptake by organs.^[13,14] Briefly, nanoparticles were transferred to aqueous media by encapsulation with phospholipid–polyethylene glycol (PEG) (Figure 4.4b).^[15] The nanoparticles showed excellent colloidal stability without agglomerations in phosphate-buffered saline (PBS) as well as in blood plasma, and their hydrodynamic diameters were maintained at 18–30 nm for over 10 days (Figure 4.4a). The ROS-scavenging activity of the ceria nanoparticles, assessed by the superoxide dismutase-mimetic assay and catalase-mimetic assay, was found to be dose-dependent (Figure 4.5). Furthermore, we examined the autocatalytic properties of ceria nanoparticles using visual inspection of color change and UV/Vis spectroscopic analysis.^[16,17] When H₂O₂ solutions of various

concentrations were added to PBS solutions containing 5 mM ceria nanoparticles, reversible autocatalytic activity persisted even after 3 weeks (Figure 4.6).

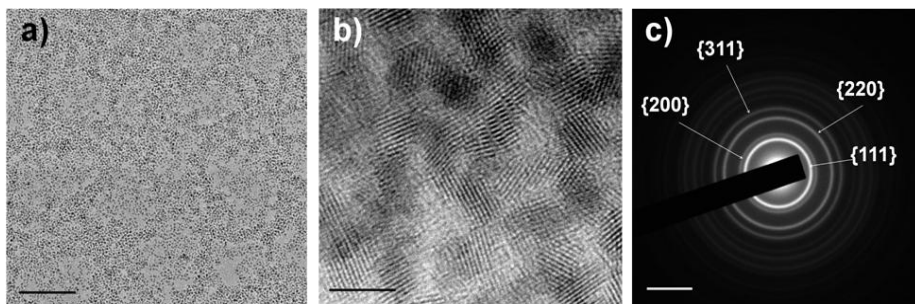


Figure 4.1. a) Transmission electron microscope (TEM) images revealed discrete and uniform 3-nm-sized ceria nanoparticles. Scale bar = 100 nm. b) High-resolution TEM images revealed a cross-lattice pattern, demonstrating the highly crystalline nature of the ceria nanoparticles. Scale bar = 5 nm. c) The selected area electron diffraction pattern.

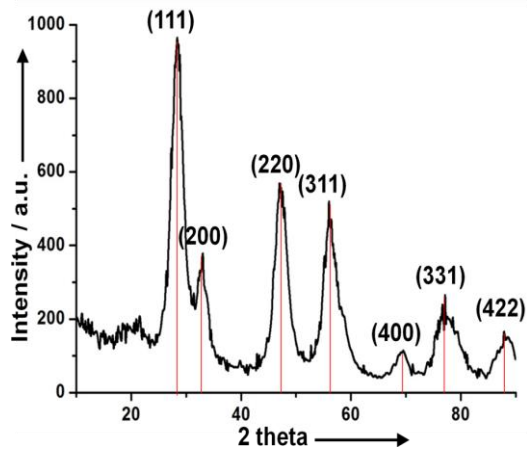


Figure 4.2. X-ray diffraction pattern revealed a cubic fluorite structure.

Scale bar = 5 nm^{-1} .

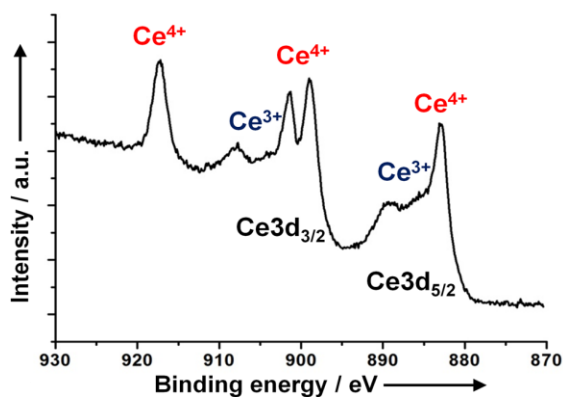


Figure 4.3. X-ray photoelectron spectroscopy analysis was used to identify the valence state of cerium ions and confirmed corresponding binding energy peaks for Ce³⁺ (peaks at 885.0 and 903.5 eV) and Ce⁴⁺ (peaks at 882.1, 888.1, 898.0, 900.9, 906.4, and 916.40 eV).

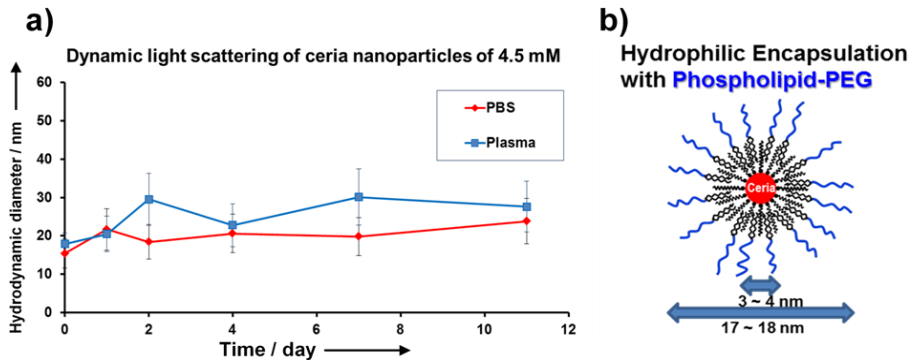


Figure 4.4. a) Hydrodynamic diameters of phospholipid-PEG-capped ceria nanoparticles in PBS and blood plasma demonstrated that they do not agglomerate and are very well dispersed for over ten days in the physiological medium. b) A sketch of the ceria nanoparticles geometry (core diameter $d_c = 3 - 4$ nm and hydrodynamic diameter $d_h = 17 - 18$ nm).

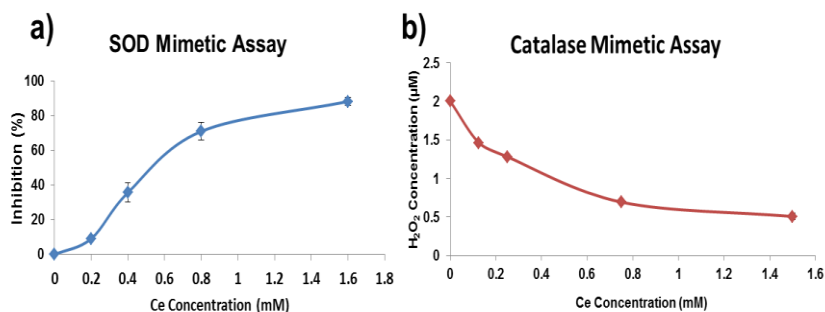


Figure 4.5. ROS-scavenging activities of ceria nanoparticles by superoxide dismutase-mimetic assay and catalase-mimetic assay. a) Dose-dependent O₂^{•-} scavenging by ceria nanoparticles. b) Quenching activities of hydrogen peroxide by ceria nanoparticles. Ceria nanoparticles exhibit catalase mimetic activity at physiologically relevant hydrogen peroxide concentrations.

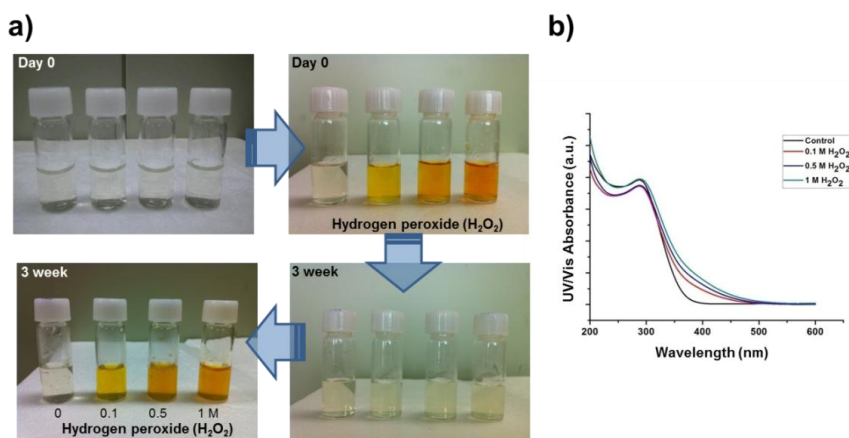


Figure 4.6. Autocatalytic activity of ceria nanoparticles as examined by color change and UV/Vis spectroscopy. a) Reversible color change, demonstrating that Ce^{3+} species were generated by the addition of a hydrogen peroxide (H_2O_2) solution to the ceria nanoparticles. b) UV/Vis absorption spectra show the red-shift of the band between 300 and 400 nm after the addition of H_2O_2 solution to 5 mM ceria nanoparticle suspensions.

4.3.2 Effects of ceria nanoparticles on ROS-induced cell death *in vitro*

To investigate the effects of ceria nanoparticles on ROS-induced cell death *in vitro*, CHO-K1 cells were incubated with *tert*-butyl hydroperoxide (tBHP), which increases intracellular ROS.^[18] Using 3-(4,5-dimethylthiazol-2-yl)-2,5-diphenyltetrazolium bromide (MTT) assay, we found that 1 mM tBHP significantly increased cell death compared with the control (83%, $p < 0.05$; Figure 4.7), while the addition of 0.125 mM ceria nanoparticles significantly increased cell viability (113%, $p < 0.05$). We also found that ceria nanoparticles were mostly detected in intracellular spaces, as shown by fluorescence imaging with rhodamine dye (Figure 4.8). To investigate the concentration- and time-dependent cellular uptake, we performed fluorescence-activated cell sorting study using fluorescent dye-conjugated 3 nm-sized ceria nanoparticles (Figure 4.9). The cellular uptake was increased with dose-dependent manner until 0.125 mM, and was saturated above 0.125 mM. The cellular uptake was increased with time-dependent manner until 180 min. Taken together, our results demonstrate that ceria nanoparticles introduced into cells show

protective effects against ROS-induced cell death *in vitro*, which correlated with the results of a previous report.^[19]

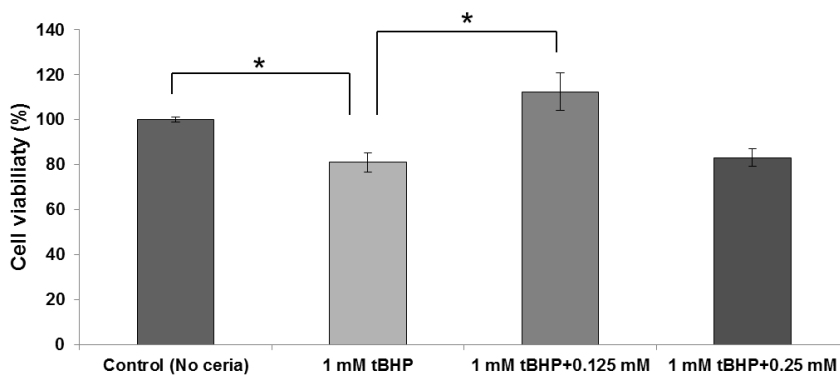


Figure 4.7. Protective effects of ceria nanoparticles against ROS-induced cell death *in vitro*. To investigate the effects of ceria nanoparticles on ROS-induced cell death *in vitro*, CHO-K1 cells were incubated with *tert*-butyl hydroperoxide (tBHP), which increases intracellular ROS (n = 3 each). In an MTT assay, the addition of 1 mM tBHP significantly increased cell death compared to the control (83%, $p < 0.05$), while the addition of 0.125 mM ceria nanoparticles increased cell viability (113%, $p < 0.05$).

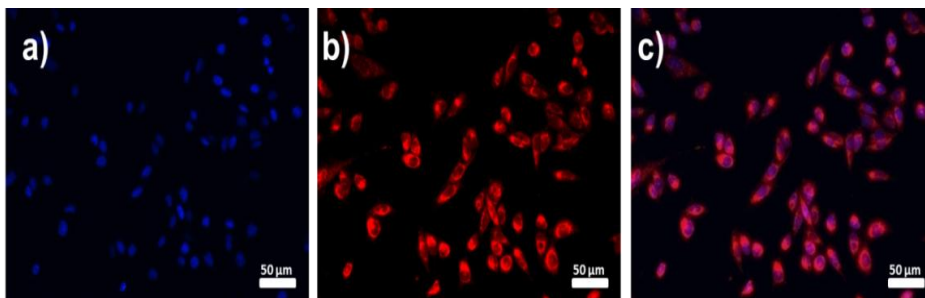


Figure 4.8. Fluorescence microscopy images of CHO-K1 cells incubated with ceria nanoparticles conjugated with a fluorescent rhodamine dye. a) The nuclei were stained blue with 4'-6-diamidino-2-phenylindole (DAPI). b) Red fluorescence from the nanoparticles was detected throughout the cytoplasm. c) Overlapped images from a) and b) represent the cellular uptake and intracellular localization of ceria nanoparticles.

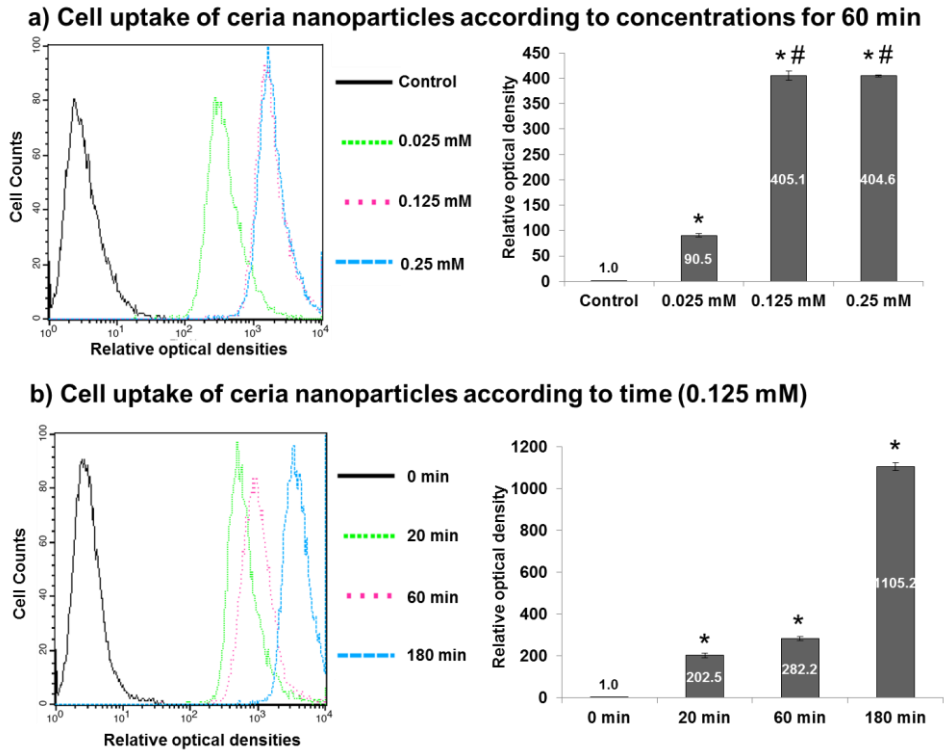


Figure 4.9. Cellular uptake of ceria nanoparticles according to concentration and time. a) The cells were cultured in a 6-well plate and various concentrations of FITC-conjugated ceria nanoparticles were added to each well and incubated. After 60 min, the cells were washed with PBS 2 times, and intensity of the green fluorescence on the cell was detected using fluorescence-activated cell sorting (FACS). For 3 nm (core size) ceria nanoparticles, the uptake in cells was increased with dose dependent manner until 0.125 mM, and above 0.125 mM, the uptake of ceria nanoparticles was saturated (* compared with control, #

compared with 0.025 mM, $p < 0.05$). b) The uptake of 3 nm (core size) ceria nanoparticles was increased with time-dependent manner until 180 min (*, $p < 0.05$ compared with control).

4.3.3 Neuroprotective effects of ceria nanoparticles *in vivo*

To investigate the neuroprotective effects of ceria nanoparticles *in vivo*, we induced ischemic stroke in rats and subsequently introduced ceria nanoparticles by intravenous injection. We then compared brain infarct volumes in rats treated with various doses of ceria nanoparticles to determine an optimal dose (Figure 4.10a,b,c). Low-dose ceria nanoparticles (0.1 and 0.3 mg/kg) did not decrease infarct volumes, whereas ceria nanoparticles at concentrations of 0.5 and 0.7 mg/kg considerably reduced infarct volumes up to 50% of those of the control group ($p < 0.05$). However, higher doses of ceria nanoparticles (1.0 and 1.5 mg/kg) failed to show a protective effect against stroke. To support these findings, we performed microscopic analysis of cell death in frozen brain sections using terminal deoxynucleotidyl transferase-mediated dUTP-biotin nick end labeling (TUNEL) assays (Figure 4.11a). Quantitative analysis showed that the number of TUNEL-positive cells was markedly decreased in the ceria-injected group (0.5 mg/kg; $p < 0.05$; Figure 4.11b). Collectively, we concluded that the optimal dose of ceria nanoparticles (0.5 to 0.7 mg/kg) had powerful neuroprotective effects in this rodent stroke model, and all subsequent

experiments were performed using 0.5 mg/kg ceria nanoparticles. On the basis of the observed therapeutic window for ceria nanoparticles *in vivo*, we found that the indiscriminate use of nanoparticles without considering the optimal dose may not be protective and may even be harmful.^[20, 21] Recent studies using a hippocampal brain slice model^[22] and spinal cord injury model^[23] have shown that ceria nanoparticles may be protective against ischemic or traumatic neuronal damage *in vitro*. Thus, in the current study, we demonstrated this protective effect, using the optimal dose, in a living animal model of ischemic stroke to mimic human clinical settings.

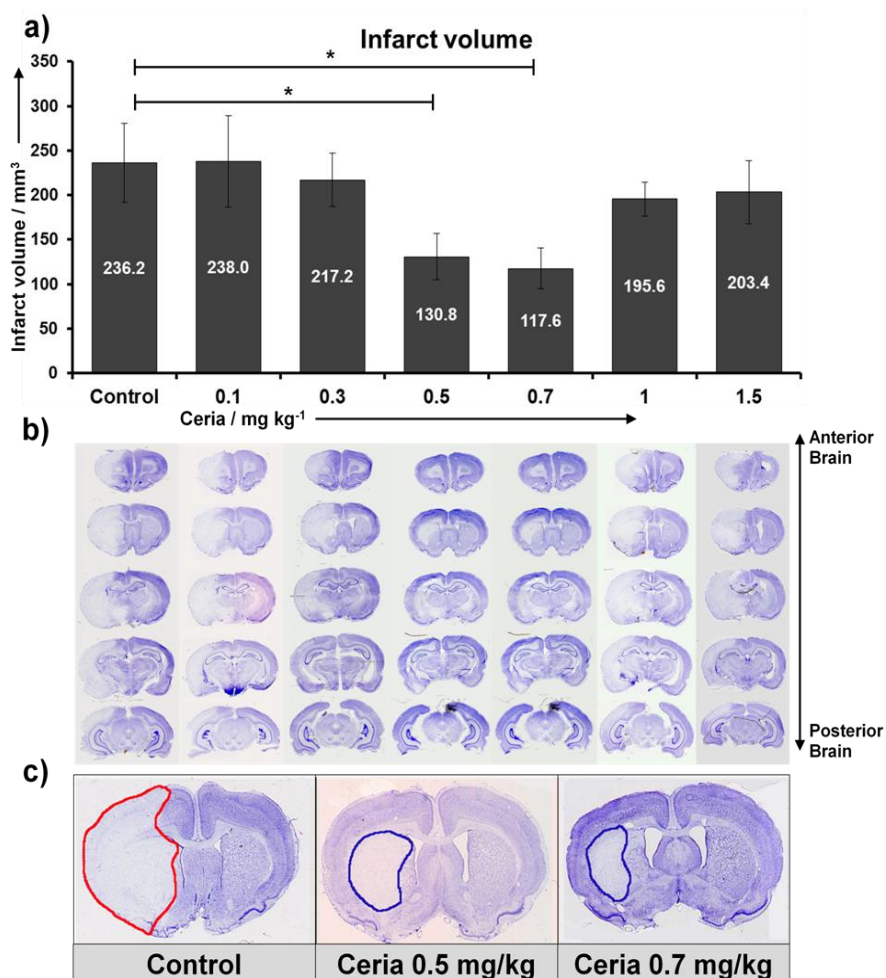


Figure 4.10. Infarct volume and ischemic cell death *in vivo*. a) Low-dose ceria nanoparticles (0.1 and 0.3 mg/kg) did not decrease infarct volumes, whereas 0.5 and 0.7 mg/kg ceria nanoparticles considerably reduced infarct volumes, to as little as 50% of those of the control group (*, $p < 0.05$). Higher doses of ceria nanoparticles (1.0 and 1.5 mg/kg) failed to exhibit protective effects from stroke (n = 12 for each

group, except 0.1 and 1.5 mg/kg, where n = 6). b) Brain slices are presented from anterior (top) to posterior (bottom), with intervals of 2 mm. On Nissl-stained brains, infarcts are shown as pale blue-colored lesions, while undamaged region are stained as deep blue. Infarct areas were maximally decreased at 0.5 and 0.7 mg/kg ceria nanoparticles. c) Representative slices clearly showed that 0.5 and 0.7 mg/kg ceria nanoparticles can significantly reduced infarct volume.

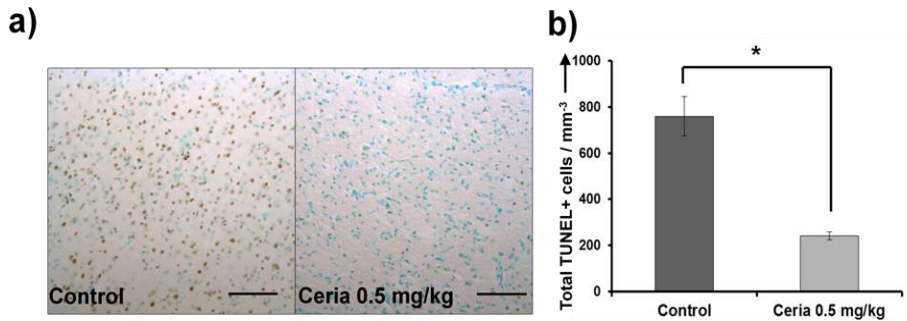


Figure 4.11. Ischemic cell death *in vivo*. a) Microscopic analysis of cell death in brain slices using terminal deoxynucleotidyl transferase-mediated dUTP-biotin nick end labeling (TUNEL). TUNEL-positive cells are shown in brown, and TUNEL-negative cells, which were counter-stained with methyl green, are shown in blue. The number of TUNEL-positive cells was reduced in the ceria-injected group (0.5 mg/kg). Scale bar = 100 μ m. b) In our quantitative analysis, the number of TUNEL-positive cells was markedly decreased in the ceria-injected group (*, $p < 0.05$; $n = 4$ each).

4.3.4 Delivery of ceria nanoparticles through an *in vivo* study

Since the brain is secured by the blood-brain barrier and ceria nanoparticles were injected intravenously in this study, we also analyzed the delivery of ceria nanoparticles through an *in vivo* study to determine whether intravenous injection could effectively localize ceria nanoparticles to the ischemic brain. For this experiment, concentrations of ceria nanoparticles were measured in various internal organs of rats using inductively coupled plasma-mass spectrometry analysis. Interestingly, while the concentration of ceria nanoparticles in the nonischemic brain was very low, the level of ceria nanoparticles increased strikingly 24 h after ischemia ($p < 0.05$; Figure 4.12), exceeding the concentrations of nanoparticles observed in the kidneys and heart. The concentration of ceria nanoparticles in brain after stroke was increased with dose dependent manner with 0.5, 1.0, and 1.5 mg/kg. Next, we sought to track ceria nanoparticles microscopically using rhodamine B isothiocyanate-conjugated ceria nanoparticles and fluorescence microscopy analysis. As shown in Figure 4.13, a significant number of positively stained cells were identified in the ischemic hemisphere, but very few cells were located in the

nonischemic hemisphere. We conducted computerized visual augmentation using 3-dimensional reconstruction of the fluorescence signals and found that the signals for ceria nanoparticles were significantly increased in the peri-infarct area in the ischemic hemisphere (Figure 4.14). Thus, we demonstrated that intravenously injected ceria nanoparticles did not sufficiently permeate the normal brain tissue^[24] but were able to permeate ischemic brain tissue; This was likely possible because brain ischemia leads to extensive breakage of the blood-brain barrier, which may facilitate passage of ceria nanoparticles into the brain.^[25] Furthermore, the accumulation of ceria nanoparticles was increased due to their uniformity, small size, and prolonged blood circulation due to PEGylation.

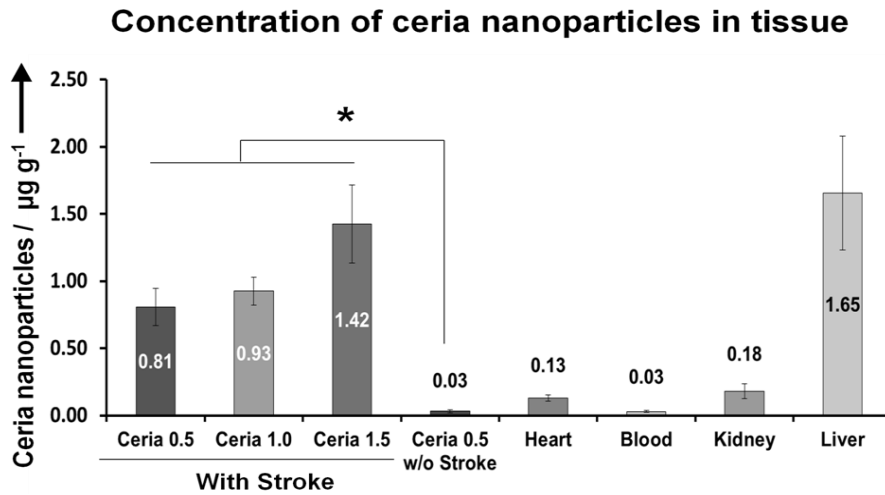


Figure 4.12. The concentration of ceria nanoparticles in the nonischemic brain was very low, but significantly increased at 24 h after ischemia (*, $p < 0.05$); values were even higher than those observed in the kidneys and heart ($n = 8$ for brain with stroke, otherwise $n = 4$ each).

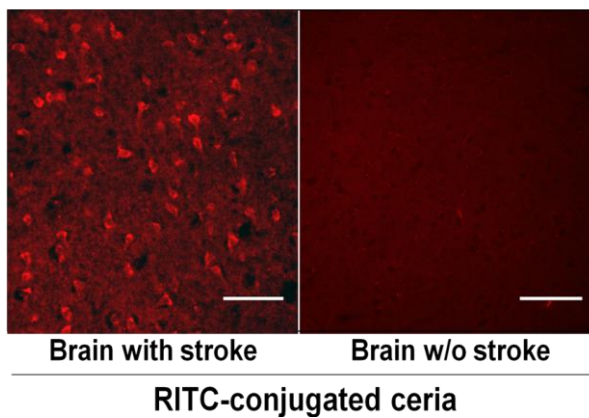


Figure 4.13. Cells that were positively stained with rhodamine B isothiocyanate-conjugated ceria nanoparticles were identified to a great extent in the ischemic hemisphere, but only minimally in the nonischemic hemisphere. Scale bar = 100 μm .

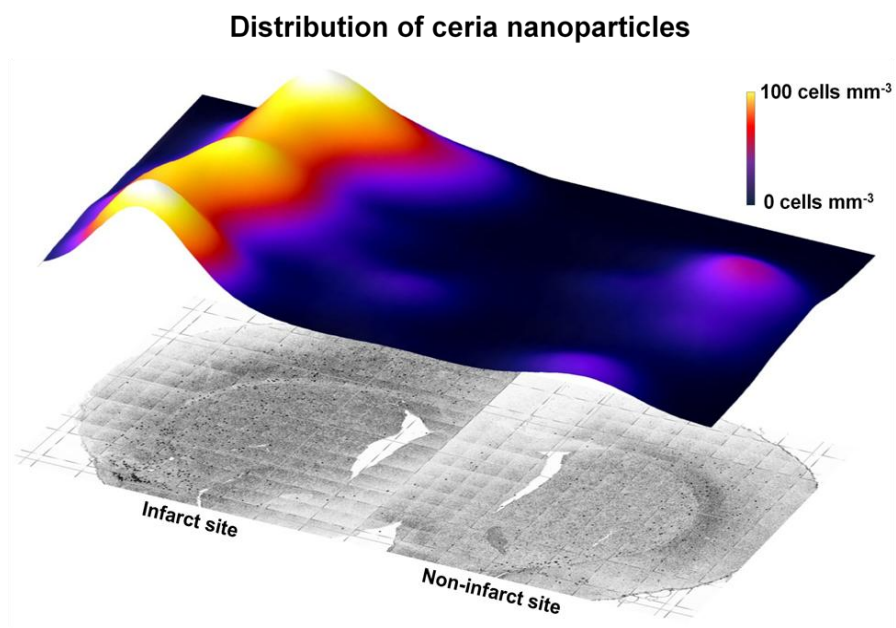


Figure 4.14. By using computerized visual augmentation with 3-dimensional reconstruction of fluorescence signals, we found that signals for ceria nanoparticles were greatly increased in the peri-infarct area in the ischemic hemisphere.

4.3.5 ROS scavenging and apoptosis decreasing effects of ceria nanoparticles *in vivo*

We investigated whether ceria nanoparticles reduce ROS and apoptosis *in vivo* because oxidative damage is a major cause of ischemic brain injury and elicits apoptotic cell death.^[2,3] After a stroke, oxidized hydroethidine signals (as a measure of ROS) were lower in the ceria-injected group than in the control group ($p < 0.05$; Figure 4.15), indicating that ceria nanoparticles acted as antioxidants after ischemia. To analyze ROS quantitatively, we performed the assay for lipid peroxides. The average concentration of lipid peroxides in stroke area was measured to be $24.6 \pm 7.9 \mu\text{M}$. After treating with 0.5 mg/kg of ceria nanoparticles, the concentration was significantly decreased to $15.5 \pm 4.9 \mu\text{M}$ ($p < 0.05$; Figure 4.16). To investigate the effects of ceria nanoparticles on apoptosis after stroke, we analyzed apoptotic TUNEL-positive cells. The number of apoptotic cells in the ceria nanoparticle-injected group was lower than that in the control group ($p < 0.05$; Figure 4.17), and pro-apoptotic proteins, such as phospho-p53, cleaved caspase-3, and gelsolin, decreased in the ceria nanoparticle-injected group ($p < 0.05$; Figure 4.18a,b). ROS production and

apoptosis are closely related because they both occur in the mitochondria. Furthermore, ROS directly stimulates apoptosis-regulated proteins, such as p53.^[26,27] Recently, amine-modified single-walled carbon nanotubes were investigated as potential therapeutic agents for ischemic stroke through reducing apoptosis.^[28] In a previous *in vitro* study, ceria nanoparticles decreased apoptosis as well as ROS.^[29] Thus, the results of our current *in vivo* model support these previous studies, demonstrating that ceria nanoparticles can reduce apoptotic cell death by decreasing ROS, which may lead to a decreased infarct volume.

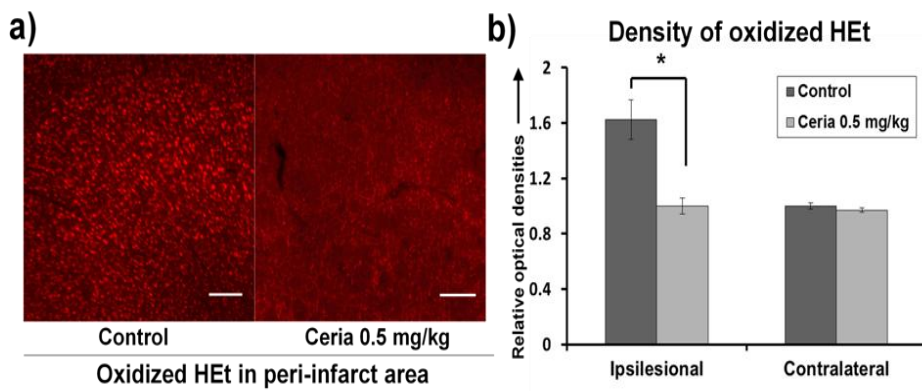


Figure 4.15. Reactive oxygen species (ROS)-scavenging effects. a, b) Oxidized hydroethidine signals (as a detector of ROS) were decreased in the ceria nanoparticle-injected group compared with the control group (*, $p < 0.05$; $n = 4$ each). Scale bar = 200 μm .

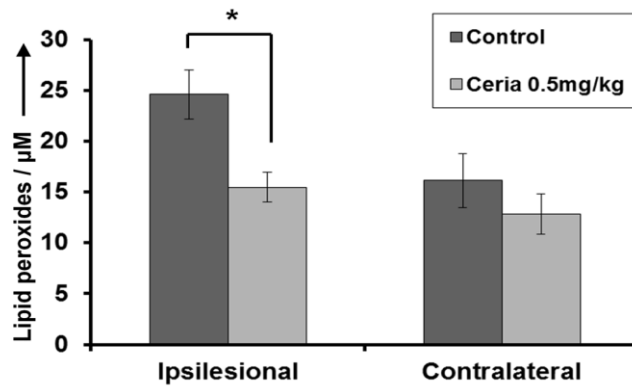


Figure 4.16. Lipid peroxides in stroke area was decreased in ceria-injected group compared with control (*, $p < 0.05$; $n = 8$ each).

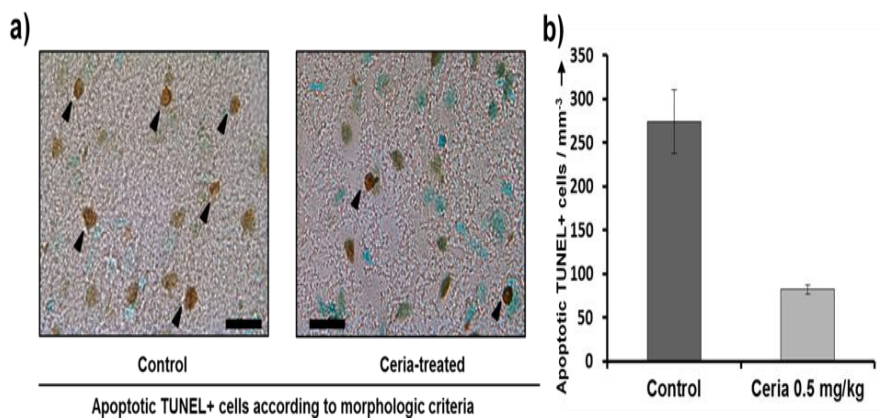


Figure 4.17. Apoptosis-reducing effects a) Morphological criteria of apoptotic TUNEL-positive cells. According to morphological criteria, apoptosis-specific TUNEL-positive nuclei with chromatin condensation and fragmented nuclei (≥ 2 apoptotic bodies) were considered apoptotic cells (arrow), and non-apoptotic TUNEL-positive cells exhibited diffuse light labeling of nuclei. TUNEL-negative cells were counterstained with methyl green (blue). In the cortical area, the number of apoptotic TUNEL-positive cells in the ceria-injected group was lower than in the control. Scale bar = 50 μm . b) The number of apoptotic cells in the ceria-nanoparticle-injected group was lower than that in the control group (*, $p < 0.05$; $n = 4$ each).

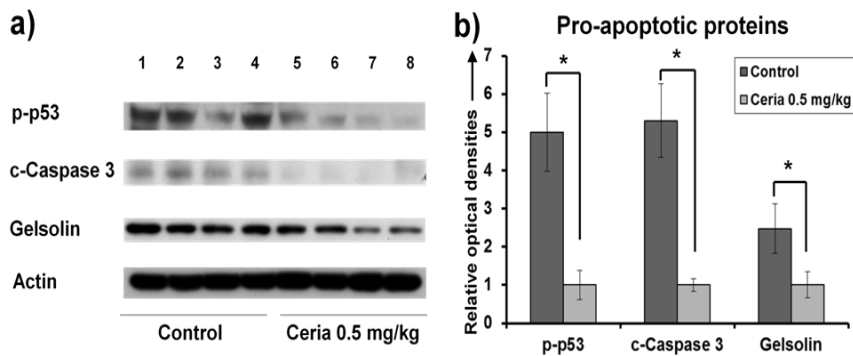


Figure 4.18. a, b) In western blotting analyses, pro-apoptotic proteins, such as phospho-p53, cleaved caspase-3, and gelsolin, decreased in the ceria nanoparticle-injected group compared with the control group (*, $p < 0.05$; $n = 4$ each). These proteins were obtained from cell extracts in infarcted hemisphere.

4.4 Conclusion

In conclusion, optimal doses of ceria nanoparticles (0.5 and 0.7 mg/kg) reduced ischemic brain damage. Our ceria nanoparticles targeted the damaged area by disruption of the blood-brain barrier after ischemia. Innovative nanotechnology such as the ceria nanoparticles studies here makes it possible to produce more chemically potent and biologically compatible materials. Previous studies evaluated the *in vivo* protective effects of ceria nanoparticles in only a few diseases, including retinal degeneration and cardiomyopathy.^[30,31] This report is the first demonstration of the protective effects of ceria nanoparticles against ischemic stroke in living animals, offering hope and an alternative treatment modality for patients with ischemic stroke.

4.5 References

- [1] Roger, V. L. *et al. Circulation* **2012**, *125*, e20.
- [2] Allen, C. L.; Bayraktutan, U. *Int. J. Stroke* **2009**, *4*, 461.
- [3] P. H. Chan, *J. Cereb. Blood Flow Metab.* **2001**, *21*, 2.
- [4] I. Celardo, J. Z. Pedersen, E. Traversa, L. Ghibelli, *Nanoscale* **2011**, *3*, 1411.
- [5] D. Sameer, P. Swanand, V. N. T. K. Satyanarayana, S. Seal, *Apply. Phys. Lett.* **2005**, *87*, 133113.
- [6] W. J. Stark, *Angew. Chem.* **2011**, *123*, 1276; *Angew. Chem. Int. Ed.* **2011**, *50*, 1242.
- [7] E. G. Heckert, A. S. Karakoti, S. Seal, W. T. Self, *Biomaterials* **2008**, *29*, 2705.
- [8] C. Korsvik, S. Patil, S. Seal, W. T. Self, *Chem. Commun.* **2007**, 1056.
- [9] T. Pirmohamed, J. M. Dowding, S. Singh, B. Wasserman, E. Heckert, A. S. Karakoti, J. E. S. King, S. Seal, W. T. Self, *Chem. Commun.* **2010**, *46*, 2736.
- [10] S. Singh, T. Dosani, A. S. Karakoti, A. Kumar, S. Seal, W. T. Self, *Biomaterials* **2011**, *32*, 6745.
- [11] T. Yu, J. Moon, J. Park, Y. I. Park, H. B. Na, B. H. Kim, I. C. Song, W. K.

- Moon, T. Hyeon, *Chem. Mater.* **2009**, *21*, 2272.
- [12] H. Gu, M. D. Soucek, *Chem. Mater.* **2007**, *19*, 1103.
- [13] A. S. Karakoti, S. Das, S. Thevuthasan, S. Seal, *Angew. Chem.* **2011**, *123*, 2024; *Angew. Chem. Int. Ed.* **2011**, *50*, 1980.
- [14] P. Rivera-gil, D. J. D. Aberasturi, V. Wulf, B. Pelaz, P. D. Pino, Y. Zhao, J. M. D. L. Fuente, I. R. D. Larramendi, T. Rojo, X.-J. Liang, W. J. Parak, *Acc. Chem. Res.* **2012**, *45*, 1637.
- [15] B. Dubertret, P. Skourides, D. J. Norris, V. Noireaux, A. H. Brivanlou, A. Libchaber, *Science* **2002**, *298*, 1759.
- [16] J. M. Perez, A. Asati, S. Nath, C. Kaittanis, *Small* **2008**, *4*, 552.
- [17] A. S. Karakoti, S. Singh, A. Kumar, M. Malinska, S. V. N. T. Kuchibhatla, K. Wozniak, W. T. Self, S. Seal, *J. Am. Chem. Soc.* **2009**, *131*, 14144.
- [18] K. Zhao, G.-M. Zhao, D. Wu, Y. Soong, A. V. Birk, P. W. Schiller, H. H. Szeto, *J. Biol. Chem.* **2004**, *279*, 34682.
- [19] A. S. Karakoti, S. Singh, J. M. Dowding, S. Seal, W. T. Self, *Chem. Soc. Rev.* **2010**, *39*, 4422.
- [20] N. Singh, C. A. Cohen, B. A. Rzigalinski, *Ann. N. Y. Acad. Sci.* **2007**, *1122*, 219.
- [21] M. Horie, K. Nishio, H. Kato, K. Fujuta, S. Endoh, A. Nakamura, A.

- Miyauchi, S. Kinugasa, K. Yamamoto, E. Niki, Y. Yoshida, Y. Hagihara, H. Iwahashi, *J. Biochem.* **2011**, *150*, 461.
- [22] A. Y. Estevez, S. Pritchard, K. Harper, J. W. Aston, A. Lynch, J. J. Lucky, J. S. Ludington, P. Chatani, W. P. Mosenthal, J. C. Leiter, S. Andreescu, J. S. Erlichman, *Free. Radic. Biol. Med.* **2011**, *51*, 1155.
- [23] M. Das, S. Patil, N. Bhargava, J.-F. Kang, L. M. Riedel, S. Seal, J. J. Hickman, *Biomaterials* **2007**, *28*, 1918.
- [24] S. S. Hardas, D. A. Butterfield, R. Sultana, M. T. Tseng, M. Dan, R. L. Florence, J. M. Unrine, U. M. Graham, P. Wu, E. A. Grulke, R. A. Yokel, *Toxicol. Sci.* **2010**, *116*, 562.
- [25] Y. Yang, G. A. Rosenberg, *Stroke* **2011**, *42*, 3323.
- [26] K. Niizuma, H. Endo, P. H. Chan, *J. Neurochem.* **2009**, *109* (Suppl. 1), 133.
- [27] K. Niizuma, H. Yoshioka, H. Chen, G. S. Kim, J. E. Jung, M. Katsu, N. Okami, P. H. Chan, *Biochim. Biophys. Acta* **2010**, *1802*, 92.
- [28] H. J. Lee, J. Park, O. J. Yoon, H. W. Kim, D. Y. Lee, D. H. Kim, W. B. Lee, N.-E. Lee, J. V. Bonventre, S. S. Kim, *Nature Nanotech.* **2011**, *6*, 121.
- [29] A. Clark, A. Zhu, K. Sun, H. R. Petty, *J. Nanopart. Res.* **2011**, *13*, 5547.
- [30] J. Chen, S. Patil, S. Seal, J. F. McGinnis, *Nature Nanotech.* **2006**, *1*, 142.

[31] J. Niu, A. Azfer, L. M. Rogers, X. Wang, P. E. Kolattukudy, *Cardiovasc. Res.* **2007**, *73*, 549.

Bibliography

1. International Publications

- 1) **Taeho Kim**, Eric Momin, Jonghoon Choi, Kristy Yuan, Hasan Zaidi, Jaeyun Kim, Mihyun Park, Nohyun Lee, Michael T. McMahon, Alfredo Quinones-Hinojosa, Jeff W. M. Bulte, Taeghwan Hyeon,* and Assaf A. Gilad,*

“Mesoporous Silica-Coated Hollow Manganese Oxide Nanoparticles as Positive T₁ Contrast Agents for Labeling and MRI Tracking of Adipose-Derived Mesenchymal Stem Cells”,
Journal of the American Chemical Society **2011**, *133*, 2955–2961.

- 2) Chi Kyung Kim,[†] **Taeho Kim** (co-first author),[†] In-Young Choi, Min Soh, Dohoung Kim, Young-Ju Kim, Hyunduk Jang, Hye-Sung Yang, Jun Yup Kim, Hong-Kyun Park, Seung Pyo Park, Sangseung Park, Taekyung Yu, Byung-Woo Yoon, Seung-Hoon Lee,* and Taeghwan Hyeon,*

“ Ceria Nanoparticles that can Protect against Ischemic Stroke”,

Angewandte Chemie International Edition **2012**, *51*, 11039–11043.

- 3) **Taeho Kim**, Nohyun Lee, Dian Arifin, Mirosław Janowski, Piotr Walczak, Taeghwan Hyeon,* and Jeff W. M. Bulte,*

“Micro-CT Imaging of Human Mesenchymal Stem Cells Labeled with Gold Nanoparticles”,

Manuscript in Preparations.

- 4) Mohammadreza Shokouhimehr,[†] **Taeho Kim** (co-first author),[†] Youngjin Jang, Samuel Woojoo Jun, Byung Hyo Kim, Kwangsoo Shin, Jaeyun Kim, and Taeghwan Hyeon,*

“Magnetically recyclable carbon nanocomposite catalyst for heterogeneous Suzuki cross-coupling reaction”,

Green Chemistry, submitted.

- 5) Ji Eun Lee, Nohyun Lee, **Taeho Kim**, Jaeyun Kim, and Taeghwan Hyeon,*

“Multifunctional Mesoporous Silica Nanocomposite Nanoparticles for Theranostic Applications”,

Accounts of Chemical Research **2011**, *44*, 893–902.

- 6) Jonghoon Choi, Kyobum Kim, **Taeho Kim**, Guanshu Liu, Amnon Bar-Shir, Taeghwan Hyeon, Michael T. McMahon, Jeff W.M. Bulte, John P. Fisher, and Assaf A. Gilad,*
“Multimodal imaging of sustained drug release from 3-D poly(propylene fumarate) (PPF) scaffolds”,
Journal of Controlled Release **2011**, *156*, 239–245.
- 7) Jaeyun Kim, Dian R. Arifin, Naser Muja, **Taeho Kim**, Assaf A. Gilad, Heechul Kim, Aravind Arepally, Taeghwan Hyeon,* and Jeff W. M. Bulte,*
“Multifunctional Capsule-in-Capsules for Immunoprotection and Trimodal Imaging”,
Angewandte Chemie International Edition **2011**, *50*, 2317–2321.
- 8) Bong-Hyun Jun, Gunsung Kim, Jongho Baek, Homan Kang, **Taeho Kim**, Taeghwan Hyeon, Dae Hong Jeong, and Yoon-Sik Lee,*
“Magnetic field induced aggregation of nanoparticles for sensitive molecular detection”,
Physical Chemistry Chemical Physics **2011**, *13*, 7298–7303.

9) Ji Eun Lee, Nohyun Lee, Hyongsu Kim, Jaeyun Kim, Seung Hong Choi, Jeong Hyun Kim, **Taeho Kim**, In Chan Song, Seung Pyo Park, Woo Kyung Moon, and Taeghwan Hyeon,*

“Uniform Mesoporous Dye-Doped Silica Nanoparticles Decorated with Multiple Magnetite Nanocrystals for Simultaneous Enhanced Magnetic Resonance Imaging, Fluorescence Imaging, and Drug Delivery”,

Journal of the American Chemical Society **2010**, *132*, 552–557.

10) Jaeyun Kim, Hoe Suk Kim, Nohyun Lee, **Taeho Kim**, Hyongsu Kim, Taekyung Yu, In Chan Song, Woo Kyung Moon, and Taeghwan Hyeon,*

“Multifunctional Uniform Nanoparticles Composed of a Magnetite Nanocrystal Core and a Mesoporous Silica Shell for Magnetic Resonance and Fluorescence Imaging and for Drug Delivery”,

Angewandte Chemie International Edition **2008**, *47*, 8438–8441.

2. Patents

1) 현택환, 이승훈, **김태호**, 김치경,

“세리아 나노복합체와 이를 포함하는 약학 조성물 및 이들의 제조 방법”,

대한민국 특허 출원 제 10-2012-0036880, 2011년 4월 9일.

3. International Conferences

- 1) **Taeho Kim**, Taeghwan Hyeon,* and Jeff W. M. Bulte,*

“Micro-CT Imaging of Human Mesenchymal Stem Cells Labeled with Gold Nanoparticles”,

2012 World Molecular Imaging Congress (WMIC) Meeting, Dublin, Ireland, September, **2012**.

- 2) **Taeho Kim**, Chi Kyung Kim, Seung-Hoon Lee,* and Taeghwan Hyeon,*

“Ceria Nanoparticles Protect against Ischemic Stroke”,

2012 American Chemical Society (ACS) Fall Meeting, Philadelphia, PA, U.S.A., August, **2012**.

- 3) **Taeho Kim**, Taeghwan Hyeon,*

“Mesoporous Silica-Coated Hollow Manganese Oxide

Nanoparticles as Positive T1 Contrast Agents for Labeling and MRI Tracking of Adipose-Derived Mesenchymal Stem Cells”,
The 3rd Asian Biomaterials Congress 2011, BEXCO, Busan, Korea,
September, **2011**.

4) **Taeho Kim**, Taeghwan Hyeon,*

“Mesoporous Silica-Coated Hollow Manganese Oxide Nanoparticles as Positive T1 Contrast Agents for Labeling and MRI Tracking of Adipose-Derived Mesenchymal Stem Cells”,
11th IEEE International Conference on Nanotechnology Joint symposium with NANO KOREA 2011, KINTEX, Goyang, Korea,
August, **2011**.

5) **Taeho Kim**, Taeghwan Hyeon,* and Assaf, A. Gilad,*

“Hollow structured mesoporous silica coated MnO nanoparticles as highly efficient T1 contrast agents and their applications in MR tracking of transplanted mesenchymal stem cells”,
18th Annual Meeting of the International Society of Magnetic Resonance in Medicine (ISMRM), Stockholm, Sweden, May, **2010**.

- 6) Jaeyun Kim, **Taeho Kim**, Taeghwan Hyeon,* and Jeff W. M. Bulte,*
“Microfabrication of multifunctional alginate capsule-in-capsule (CIC) for immunoprotected cell transplantation with MR, CT, and US visibility”,
Imaging the Pancreatic Beta Cell, 4th Workshop, NIDDK/NIBIB,
Washington D.C., U.S.A., April, **2009**.

4. Domestic Conferences

- 1) **Taeho Kim**, Taeghwan Hyeon,*
“Mesoporous Silica-Coated Hollow Manganese Oxide Nanoparticles as Positive T1 Contrast Agents for Labeling and MRI Tracking of Adipose-Derived Mesenchymal Stem Cells”,
2011 The Korean Society of Industrial and Engineering Chemistry Spring Meeting, ICC Jeju, Jeju, Koera, May, **2011**.

5. Award

Best Poster Awards at the KSIEC Meeting 2011

2011 The Korean Society of Industrial and Engineering Chemistry

Spring Meeting, ICC Jeju, Jeju, Koera, May, **2011.**

초 록

최근 다양한 기능성 나노구조 물질들은 그것들의 독특한 광학적, 기계적, 자기적, 화학적 특성과 함께 진단과 치료를 포함한 여러 생물 의학 분야에 광범위하게 적용되어왔다. 특히 활발한 학제간 공동연구를 통해 나노입자를 이용하여 여러 생물학적인 이슈들을 해석하고 이를 임상에까지 적용하려는 시도들이 행해지고 있다. 줄기세포나 면역세포와 같은 치료용 세포를 이식하여 세포치료를 행함에 있어 이미징이 가능한 나노입자의 사용은 고해상도로 세포추적을 가능하게 하여 치료 효과를 증대시켜 준다. 또한 최근에는 나노입자 자체를 화학치료제로 사용하기도 한다. 장기간의 세포추적은 조영효과가 뛰어난 나노입자의 사용, 그리고 세포와 나노입자간의 상호작용을 잘 조절함으로써 효과적으로 달성할 수 있다. 나노입자의 조성, 크기, 표면 특성과 같은 물리화학적 특성의 개선을 통해 나노입자의 치료제로서의 역할 역시 증대시킬 수 있다. 이 학위논문에서는 기능성 무기 나노입자를 이용한 효과적인 줄기세포의 추적과 뇌경색 치료에 관한 연구 결과에 대해 보고하였다.

첫번째로 다공성 실리카로 코팅된 속이 빈 구조의 산화망간 나노입자를 제조하고, 이를 이용한 T₁ 자기공명영상 세포추적 기술을 개발하였다. 본 나노입자는 속이 빈 구조의 산화망간 코어 부분이 넓은 비표면적을 가지고 있고, 코팅된 실리카 셀의 무수히 많은 기공을 통해 외부의 물 분자가 코어 부분의 망간 이온에 쉽게 접근이 가능한 특징을 가진다. 따라서 기존 산화망간 조영제에 비해 T₁ 자기공명영상 조영 효과가 크게 증대된 특성을 보인다. 이러한 나노입자를 전기천공법 (electroporation)을 이용하여 지방조직에서 추출한 성체줄기세포에 효과적으로 표지하였고, 결과적으로 T₁ 자기공명영상을 통해 이식된 줄기세포의 장기간 세포추적이 가능함을 보여주었다.

두번째로 금 나노입자를 이용한 줄기세포의 컴퓨터단층촬영 (CT) 영상화와 추적 기술을 개발하였다. 컴퓨터단층촬영은 민감도가 떨어지는 단점이 있기 때문에 이를 통한 세포추적은 매우 어렵다고 알려져 왔다. 그러나 40 nm 의 시트레이트 (citrate)로 안정화된 금 나노입자에 양이온성 고분자인 폴리-L-라이신 (poly-L-lysine)을 도입하여 복합체를 형성함으로써 금 나노입자를 효율적으로 성체줄기세포에 표지하였다. 이렇게 표지된 세포를 쥐의 뇌에 이식하여 이식된 줄기세포의

컴퓨터단층촬영 영상화와 추적의 가능성을 보여주었고, 또한 생체내에서 영상화의 한계가 $\sim 1 \times 10^4$ 개의 세포/ μl 가 됨을 밝혔다. 이와 같은 방법은 표지된 세포의 증식이나 분화 등에 악영향을 미치지 않았으며, 매우 쉽고 효과적인 방법인 동시에 X-선 형광 투시기 유도 (fluoroscopic guidance)를 통한 세포 이식 등에 널리 활용 되리라 기대된다.

마지막으로 세리아 나노입자를 이용한 뇌경색 치료제를 개발하였다. 활성산소 (ROS)는 뇌경색에 의한 뇌손상의 주요한 원인이 되고 있다. 또한 희토류의 일종인 세리아를 작은 크기의 나노입자로 만들게 되면 활성산소를 제거해 주는 항산화 효과를 보일 수 있다는 특성이 보고 되고 있다. 따라서 3 nm 의 균일한 세리아 나노입자를 제작하였고, 뇌경색을 유도한 동물모델에 주입하여 세리아 나노입자의 뇌경색 보호 효과를 살펴보았다. 본 세리아 나노입자는 생체 분산도가 매우 뛰어나 정맥 투여시에 뇌경색 부위로 잘 전달이 되었고, 적정농도 (0.5, 0.7 mg/kg)를 사용했을 시에 항산화, 항세포자멸사 효과를 통해 생체 내 뇌경색 손상을 상당히 감소시켰다.

주요어: 나노바이오기술, 줄기세포추적, 화학치료제,
자기공명영상, 산화망간 나노입자, 컴퓨터단층촬영, 금
나노입자, 뇌경색, 세리아 나노입자

학번: 2010-30804

